SEARCH FOR QUARK-LEPTON COMPOSITENESS IN THE DIMUON FINAL STATE AT DØ

A Dissertation

Submitted to the Graduate School
of the University of Notre Dame
in Partial Fulfillment of the Requirements
for the Degree of

Doctor of Philosophy

by

Nguyen Phuoc Xuan, B.S., M.S.

Neal Cason, Director

Graduate Program in Physics
Notre Dame, Indiana
April 2005

SEARCH FOR QUARK-LEPTON COMPOSITENESS IN THE DIMUON FINAL STATE AT DØ

Abstract

by

Nguyen Phuoc Xuan

We used the upgraded DØ detector at the Tevatron at $\sqrt{s} = 1.96$ TeV to collect data in a search for a compositeness signature of quarks and leptons. This analysis uses an integrated luminosity of 400 pb^{-1}. The high-mass dimuon mass spectrum is compared with that predicted by Drell-Yan (DY) scattering, modified by a contact interaction. This interaction is parameterized by a compositeness energy scale factor Λ. Preliminary limits on Λ are set at the 95% confidence level for constructive and destructive interference between the DY amplitude and the contact interaction for various quark and lepton chiralities.

To my beloved wife Bong and my friends for their tireless support and encouragement.

Whatever nature has in store for mankind, unpleasant as it may be, men must accept, for ignorance is never better than knowledge.

Enrico Fermi

CONTENTS

FIGURES vi

TABLES xi

ACKNOWLEDGMENTS xiii

CHAPTER 1: INTRODUCTION 1
1.1 The Standard Model of Particle Physics 2
1.2 Motivation for this Research 7
1.3 Organization of the Thesis 7

CHAPTER 2: THEORIES AND PHENOMENOLOGY 9
2.1 Drell-Yan Process in Standard Model 9
2.2 Leading Order Calculation of Drell-Yan Cross Section 10
2.3 Higher Order Corrections 12
2.4 Quark and Lepton Compositeness 13
2.5 Experimental Status 17

CHAPTER 3: THE EXPERIMENTAL APPARATUS 21
3.1 Fermilab Accelerator Complex 21
3.1.1 Preaccelerator 22
3.1.2 The Linac 24
3.1.3 The Booster Synchrotron 26
3.1.4 Main Injector 27
3.1.5 The Anti-proton Source 28
3.1.6 The Tevatron 30
3.2 The DØ Detector 31
3.2.1 DØ Coordinate Systems and Kinematic Variables 34
3.2.2 Solenoid 37
3.2.3 The Central Tracking System 37
3.2.4 The Preshower Detectors 47
3.2.5 The Calorimeter 49
3.2.6 Intercryostat and Massless Gap Detectors 54

3.2.7 The Muon System 55
3.2.8 Trigger and Data Acquisition Systems 60

CHAPTER 4: COMPOSITENESS ANALYSIS 68
4.1 Monte Carlo Studies 68
4.2 Muon Identification 71
4.3 Data Set and Event Selection 73
4.3.1 Event Selection Cuts 77
4.4 Background 84
4.5 Data and MC Comparison 85
4.6 Cross Section Measurement 107
4.7 Limit Calculation of Λ 109

CHAPTER 5: CONCLUSIONS 127

APPENDIX A: CANDIDATE EVENTS 129

BIBLIOGRAPHY 133

FIGURES

2.1 Lepton pair production through the Drell-Yan process. 10

2.2 Feynman diagrams for dimuon production through the Drell-Yan process. 11

2.3 Feynman diagrams for next-to-leading-order Drell-Yan process. 13

2.4 Feynman diagrams for dimuon production in the presence of compositeness. 15

2.5 Theoretical cross section versus dimuon invariant mass for the DY process and for three different values of Λ in the LL channel for constructive (left) and destructive (right) interference. 17

3.1 An aerial view of the Fermilab accelerator complex. Figure courtesy of Fermilab. 22

3.2 A schematic view of the Fermilab accelerator complex. Figure courtesy of Fermilab. 23

3.3 Production of H^- ions. Figure courtesy of Fermilab. 24

3.4 An aerial and schematic view of the preaccelerator. Figure courtesy of Fermilab. 25

3.5 Illustration of the Linac. Figure courtesy of Fermilab. 26

3.6 The Linac. Figure courtesy of Fermilab. 27

3.7 The Booster. Figure courtesy of Fermilab. 28

3.8 Main Injector. Figure courtesy of Fermilab. 29

3.9 Anti-proton production. Figure courtesy of Fermilab. 30

3.10 An aerial and schematic view of the anti-proton source. Figure courtesy of Fermilab. 31

3.11 Side view of the Run II DØ detector. Adapted from [28]. 33

3.12 The DØ coordinate system. Adapted from [21]. 35

3.13 Distribution of the interaction point in z-axis. 36

3.14 The DØ tracking system. Adapted from [30]. 37

3.15 The SMT structure. Adapted from [28]. 39

3.16 A $x - y$ view of the bulkhead. Adapted from [27]. 40

3.17 A bulkhead with two ladders. Adapted from [27]. 41

3.18 Secondary vertex finding. Adapted from [28]. 42

3.19 A quarter $r - z$ view of the CFT detector with a magnified $r - \phi$ end view of the two ribbon doublet layer configuration for two different barrels. Adapted from [28]. 43

3.20 a) Distribution for the position resolution measured in the CFT cosmic ray system test. b) An interlocking doublet ribbon configuration. Adapted from [28]. 44

3.21 Schematic of fiber-tracking element. Adapted from [35]. 44

3.22 Spectrum from a VLPC. Adapted from [35]. 46

3.23 a) A $r-z$ semi-quarter view of the CPS detector. b) A cross-sectional $r - \phi$ end view of the CFT and CPS detectors. Adapted from [28]. . 48

3.24 A quarter $r - z$ view of the FPS detector. Adapted from [28]. 49

3.25 The DØ calorimeter. Adapted from [28]. 51

3.26 A $r - z$ view of one quarter of the DØ calorimeter. Adapted from [28]. 53

3.27 Calorimeter unit cell. Adapted from [28]. 54

3.28 Full calorimeter data flow. Adapted from [27]. 55

3.29 DØ Muon System. Adapted from [28]. 57

3.30 A $r - \phi$ view of one plane of the muon mini-drift tube. Adapted from [28]. 61

3.31 A $r - \phi$ view of the segmentation of the FAMUS scintillator pixel counters Adapted from [28]. 62

3.32 The DØ trigger layout and typical trigger rates. Adapted from [28]. . 64

3.33 Level 1 and Level 2 trigger data flow paths. Adapted from [28]. . . . 65

3.34 The L3 and DAQ system layout. Adapted from [27]. 66

4.1 a) Definition of the angle θ^* at the parton level. b) Definition of the angle θ^* at NLO. Here GJ stands for the Gottfried-Jackson frame. ISR refers to initial state radiation. Adapted from [45]. 72

4.2 Run number for the entire data set. 75

4.3 η versus ϕ of muons before acceptance cuts. 76

4.4 Track quality selection. The top two plots are CFT and SMT hits distributions of the muon tracks. The bottom plot shows distribution of M$\mu\mu$ for the events rejected by this track quality selection. 78

4.5 Standard cosmic cuts. The top two plots are distributions of A and BC scintillator times of the muons in the sample. The bottom plot shows distribution of M$\mu\mu$ for the events rejected by this selection. Note that with missing hits, d0root_analysis defaults times to 99 ns. . 80

4.6 Standard isolation cuts. The top plot shows distributions of $\sum_{cone0.5}(p_T)$ of the muons in the sample. The bottom plot shows distribution of M$\mu\mu$ for the events rejected by this selection 82

4.7 Standard isolation cuts. The top plot shows distributions of $\sum_{halo}(E_T)$ of the muons in the sample. The bottom plot shows distribution of M$\mu\mu$ for the events rejected by this selection 83

4.8 Comparison of dimuon invariant mass for the data (dots) and Drell-Yan MC (filled histogram). 85

4.9 Comparison between data (points) and backgrounds (histogram) for $|\cos\theta^*|$ and $M_{\mu\mu}$ distribution. 86

4.10 The distribution in M$\mu\mu$ vs. $|\cos\theta^*|$ space for data and MC for constructive LL channel. MC is scaled by the effective luminosity. . . 87

4.11 The distribution in M$\mu\mu$ vs. $|\cos\theta^*|$ space for data and MC for destructive LL channel. MC is scaled by the effective luminosity. . . . 88

4.12 The distribution in M$\mu\mu$ vs. $|\cos\theta^*|$ space for data and MC for constructive RR channel. MC is scaled by the effective luminosity. . . 89

4.13 The distribution in M$\mu\mu$ vs. $|\cos\theta^*|$ space for data and MC for destructive RR channel. MC is scaled by the effective luminosity. . . 90

4.14 The distribution in M$\mu\mu$ vs. $|\cos\theta^*|$ space for data and MC for constructive LR channel. MC is scaled by the effective luminosity. . . 91

4.15 The distribution in M$\mu\mu$ vs. $|\cos\theta^*|$ space for data and MC for destructive LR channel. MC is scaled by the effective luminosity. . . . 92

4.16 The distribution in M$\mu\mu$ vs. $|\cos\theta^*|$ space for data and MC for constructive RL channel. MC is scaled by the effective luminosity. . . 93

4.17 The distribution in M$\mu\mu$ vs. $|\cos\theta^*|$ space for data and MC for destructive RL channel. MC is scaled by the effective luminosity. . . . 94

4.18 The distribution in M$\mu\mu$ vs. $|\cos\theta^*|$ space for data and MC for constructive LLRR channel. MC is scaled by the effective luminosity. 95

4.19 The distribution in M$\mu\mu$ vs. $|\cos\theta^*|$ space for data and MC for destructive LLRR channel. MC is scaled by the effective luminosity. . 96

4.20 The distribution in M$\mu\mu$ vs. $|\cos\theta^*|$ space for data and MC for constructive LRRL channel. MC is scaled by the effective luminosity. 97

4.21 The distribution in M$\mu\mu$ vs. $|\cos\theta^*|$ space for data and MC for destructive LRRL channel. MC is scaled by the effective luminosity. . 98

4.22 The distribution in M$\mu\mu$ vs. $|\cos\theta^*|$ space for data and MC for constructive LLLR channel. MC is scaled by the effective luminosity. 99

4.23 The distribution in M$\mu\mu$ vs. $|\cos\theta^*|$ space for data and MC for destructive LLLR channel. MC is scaled by the effective luminosity. . 100

4.24 The distribution in M$\mu\mu$ vs. $|\cos\theta^*|$ space for data and MC for constructive RLRR channel. MC is scaled by the effective luminosity. 101

4.25 The distribution in M$\mu\mu$ vs. $|\cos\theta^*|$ space for data and MC for destructive RLRR channel. MC is scaled by the effective luminosity. . 102

4.26 The distribution in M$\mu\mu$ vs. $|\cos\theta^*|$ space for data and MC for constructive VV channel. MC is scaled by the effective luminosity. . . 103

4.27 The distribution in M$\mu\mu$ vs. $|\cos\theta^*|$ space for data and MC for destructive VV channel. MC is scaled by the effective luminosity. . . 104

4.28 The distribution in M$\mu\mu$ vs. $|\cos\theta^*|$ space for data and MC for constructive AA channel. MC is scaled by the effective luminosity. . . 105

4.29 The distribution in M$\mu\mu$ vs. $|\cos\theta^*|$ space for data and MC for destructive AA channel. MC is scaled by the effective luminosity. . . 106

4.30 Comparison of kinematic variables p_T, η and ϕ for the data (points) and backgrounds (histogram). 107

4.31 Cross section measurement. 111

4.32 Limit calculation of Λ (for LL destructive model). 112

4.33 Limit calculation of Λ (for RR destructive model). 113

4.34 Limit calculation of Λ (for RL destructive model). 114

4.35 The distribution of best fit values on β_C for 200 MC trials for LL (constructive and destructive) 122

4.36 The distribution of best fit values on β_C for 200 MC trials for RR (constructive and destructive) 122

4.37 The distribution of best fit values on β_C for 200 MC trials for LR (constructive and destructive) 123

4.38 The distribution of best fit values on β_C for 200 MC trials for RL (constructive and destructive) . . . 123

4.39 The distribution of best fit values on β_C for 200 MC trials for LLRR (constructive and destructive) . . . 124

4.40 The distribution of best fit values on β_C for 200 MC trials for LRRL (constructive and destructive) . . . 124

4.41 The distribution of best fit values on β_C for 200 MC trials for LLLR (constructive and destructive) . . . 125

4.42 The distribution of best fit values on β_C for 200 MC trials for RLRR (constructive and destructive) . . . 125

4.43 The distribution of best fit values on β_C for 200 MC trials for VV (constructive and destructive) . . . 126

4.44 The distribution of best fit values on β_C for 200 MC trials for AA (constructive and destructive) . . . 126

A.1 The top figure shows XY view for the highest mass event. The bottom figure shows the $r - z$ view for the event. Reconstructed tracks are shown as well as muon system hits displayed as polygons or rectangles. Adapted from [51] . . . 131

A.2 The top figure shows the XY view for the next to the highest mass event. The bottom figure shows the $r - z$ view for the event. Reconstructed tracks are shown as well as muon system hits displayed as polygons or rectangles. Adapted from [51] . . . 132

TABLES

1.1 PROPERTIES OF QUARKS IN THE STANDARD MODEL. 5

1.2 PROPERTIES OF LEPTONS IN THE STANDARD MODEL. 5

1.3 PROPERTIES OF GAUGE BOSONS IN THE STANDARD MODEL. 6

2.1 η_{ij} FOR CONTACT INTERACTION MODE INVOLVING DIFFERENT CHIRALITY TERMS. 16

2.2 QUARK AND LEPTON COMPOSITENESS SEARCH RESULTS. ADAPTED FROM [3]. 18

2.3 DØ RUN I 95% CL LOWER LIMIT ON COMPOSITENESS SCALE Λ FOR DIFFERENT CONSTRUCTIVE AND DESTRUCTIVE CONTACT INTERACTION MODELS IN DIELECTRON CHANNEL. ADAPTED FROM [3]. 19

2.4 DØ RUN II 95% CL LOWER LIMIT ON COMPOSITENESS SCALE Λ FOR DIFFERENT CONSTRUCTIVE AND DESTRUCTIVE CONTACT INTERACTION MODELS IN DIELECTRON CHANNEL. ADAPTED FROM [20]. 20

3.1 FERMILAB TEVATRON OPERATING PARAMETERS. 32

3.2 FERMILAB ACCELERATOR COMPLEX. 32

3.3 DEPTHS OF THE CALORIMETER LAYERS. ADAPTED FROM [27]. 52

4.1 THE DIFFERENT MUON TYPE. 73

4.2 MUON QUALITY DEFINITIONS. 74

4.3 DATA SELECTION. 84

4.4 DATA AND EXPECTED BACKGROUND COMPARISON FOR EVENTS ABOVE CERTAIN DIMUON MASS CUTOFF. 108

4.5 BEST FIT VALUES FOR β_C FOR DIFFERENT CONSTRUCTIVE (β_C^+) AND DESTRUCTIVE (β_C^-) CONTACT INTERACTION MODELS IN THE DIMUON CHANNEL. 116

4.6 DØ RUN II 95% CL LOWER LIMIT (THIS ANALYSIS) ON COMPOSITENESS SCALE Λ FOR DIFFERENT CONSTRUCTIVE AND DESTRUCTIVE CONTACT INTERACTION MODELS IN DIMUON CHANNEL. 118

4.7 DØ RUN I 95% CL LOWER LIMIT ON COMPOSITENESS SCALE Λ FOR DIFFERENT CONSTRUCTIVE AND DESTRUCTIVE CONTACT INTERACTION MODELS IN DIELECTRON CHANNEL. ADAPTED FROM [3]. 119

4.8 DØ RUN II 95% CL LOWER LIMIT ON COMPOSITENESS SCALE Λ FOR DIFFERENT CONSTRUCTIVE AND DESTRUCTIVE CONTACT INTERACTION MODELS IN DIELECTRON CHANNEL. ADAPTED FROM [20]. 120

5.1 DØ RUN II 95% CL LOWER LIMIT ON COMPOSITENESS SCALE Λ FOR DIFFERENT CONSTRUCTIVE AND DESTRUCTIVE CONTACT INTERACTION MODELS IN DIMUON CHANNEL. 128

A.1 PARAMETERS OF THE HIGHEST MASS CANDIDATE EVENT. . 130

A.2 PARAMETERS OF THE NEXT TO THE HIGHEST MASS CANDIDATE EVENT. 130

ACKNOWLEDGMENTS

My time spent at University of Notre Dame has been and will be one of the happiest stages of my life. I was fortunate to work with the High Energy Physics group and to have Prof. Neal Cason as my thesis advisor.

First of all I want to thank Prof. Neal Cason for his limitless advice, encouragement and support to help me to accomplish this study.

I would also like to thank Prof. Ikaros Bigi for helping me in many ways to achieve my dream.

I thank all the members of HEP group who made the environment welcomed and lovely. Specifically, I want to thank Prof. Mitch Wayne for his help and understanding, Prof. Randy Ruchti for his enthusiasm and encouragement, Prof. Mike Hildreth and Prof. Anna Goussiou for giving me a hand when needed.

I would like to thank all professors and colleagues from physics department of University of Notre Dame. Special thanks are due to Prof. Gordon Berry.

Thank you Don Lincoln for your help, direction, support and comments during my time at Fermilab.

I would like to thank all the people from Fermilab and DØ collaboration for their enormous effort in designing and developing the tools needed to accomplish this analysis. Special thanks are dedicated to our colleagues from the New Phenomena group at DØ for their help and comments.

I would like to thank several individuals for helping me in many ways while I was at DØ. Ryan Hooper, Greg Landsberg, Jerry Blazey, Marian Zdrazil, Fred

Borchering, Jadwiga Warchol, Avto Kharchilava, Drew Alton, Paul Tedford, Eugene Galyaev, and Yuri Pogorelov, I can't thank you all enough for all your help and encouraging comments.

My gratitude is dedicated to Patrick Aurenche, Jean Tran Thanh Van and friends and colleagues from Rencontres du Vietnam for their tireless encouragement and support.

CHAPTER 1

INTRODUCTION

The standard model of quarks and leptons does not predict their mass spectrum or the number of their families. This suggests that there might exist a more fundamental basis. In one such scenario, fundamental constituents called preons interact via a new strong gauge interaction of metacolor. Below a certain characteristic energy scale Λ, the interaction becomes strong and binds the preons together to form leptons, quarks and heavy bosons. The signature for this compositeness would be a significant deviation from the Standard Model prediction of high energy cross sections. There is as yet no experimental evidence of such a deviation. The null results of such experimental searches are used to set lower limits on the characteristic scale Λ.

This is a thesis on a search for quark-lepton compositeness using data collected at the DØ detector at the Fermilab Tevatron at the colliding energy of $\sqrt{s} = 1.96$ TeV. In this chapter an overview of the amazingly successful Standard Model of Elementary Particle Physics is given. In the next chapter, emphasis is given to the specific topic of the Drell-Yan process in this framework. Physics beyond the Standard Model is discussed; specifically, theoretical and experimental aspects of the compositeness of quarks and leptons are presented in detail. A brief summary of the current experimental status of the search for quark-lepton compositeness is given at the end.

1.1 The Standard Model of Particle Physics

Modern understanding of the nature of particles and their interaction is a natural development from quantum physics, which also has a long history of theoretical prediction and experimental verification.

The Standard Model of Particle Physics is a local gauge invariant relativistic quantum field theory, evolved from efforts to categorize the experimentally observed particles and forces in terms of the fewest number of more basic constituents as fundamental building blocks and interactions. Its final form is the result of the tireless effort of many experimentalist and theorists, over a period of seventy years or so. That is in turn also inherited from outstanding scientific activities in the first third of the twentieth century. The establishment of quantum mechanics and special and general relativity led to an intense stream of breakthroughs in theoretical and experimental physics. These developments are presented decade by decade to place them in historical context [1].

- 1930's The first family of elementary particles and their interaction were investigated. A successful theory of Quantum Electrodynamics (QED), describing the interaction of photons with matter, was provided by P. A. M. Dirac. The positron, counterpart of the electron in the first family, was discovered by C. D. Anderson in 1932. The existence of a very weakly interacting neutral particle called the neutrino was postulated by W. Pauli and the neutron was discovered by J. Chadwick, which later, in 1933, were incorporated in the work of E. Fermi in β decay, which later evolved into the theory of weak interaction. A new massive elementary particle was suggested by Yukawa as mediator for the short range strong interaction, which was discovered a decade earlier. In 1937 a massive elementary, but weakly interacting particle was discovered in cosmic rays, the muon, counterpart of the electron in second family of elementary particles. The second half of the decade was spent on the theoretical difficulties associated with QED, and ended with O. Klein bringing gauge theories to β decay puzzles [1].

- 1940's The work of R. Feynman, J. Schwinger and I. Tomonaga in renormalization in QED computation showed its fruitful signature in calculations and measurements of the anomalous magnetic moment of the electron and the Lamb shift. It was later adapted in the early theory of the strong and weak interactions. The strong interaction mediator, the π meson, was discovered

in 1947. Soon after, the first class of new strange elementary particles, the K-mesons, were discovered.

- 1950's The decade began with spectacular evidence of a new quantum number, strangeness, in the discovery of strongly-interacting particles, produced in pairs and decaying with slow rates, particularly, the Λ particles. Electron neutrino was discovered by C. Cowan and F. Reines in 1956. The theory of weak interaction was established and soon 'strangeness' was discovered. The experiments to test parity violation were proposed by T. D. Lee and C. N. Yang and this soon was confirmed by C.S. Wu and V. Teledgi experimentally. The source of parity violation as the interaction of the V-A vector and axial vector was verified by R. Marshak, C. G. Sudarshan, R. Feynman and M. Gell-Mann. The realization that the weak interaction could be mediated by a massive vector particle, the W-boson, followed the work of C. N. Yang, R. L. Mills, J. Schwinger and others.

- 1960's A birth decade of the Standard Model. The vast number of strongly interacting particles was organized in terms of group structure SU(3) in the beginning of this decade. This classification was used independently by M. Gell-Mann and G. Zweig to propose quarks as building blocks of hadronic matter. In 1964, the SU(3) Yang-Mills theory was used by Y. Nambu to describe the quark-quark interaction. The works of S. Glashow in 1961, of A. Salam and J. C. Ward in 1964 and of S. Weinberg in 1967 created a model of the electroweak interactions, which after spontaneous breaking of electroweak symmetry, reduced to QED. Experimental evidence for the theory was adding up. The muon neutrino was discovered by L. Lederman, M. Schwartz, J. Steinberger in 1962 and CP-violation was discovered by J. Cronin and V. Fitch in 1964. In the end of the decade, the scaling behavior (predicted by J. Bjorken in 1966) in deep inelastic experiments gave strong evidence of the existence of smaller constituents inside the proton.

- 1970's This decade observed the fastest growth and maturation of the Standard Model both experimentally and theoretically. The absence of a flavor changing neutral current interaction, as pointed out by S. Glashow, J. Iliopoulos and L. Miani in 1970, theoretically gives evidence of the existence of a charm quark in the second family. The Glashow-Salam-Weinberg theory is renormalizable as proved by G. 't Hooft. The quantum consistency required the existence of both quarks and leptons as indicated by C. Bouchiat, J. Iliopoulos and P. Meyer. M. It was incorporated in the work of Gell-Mann and H. Fritzsch as evidence for a new quantum number for quarks, color. Based on this new quantum signature, Quantum Chromodynamics (QCD) was established as quark dynamics in 1973 by M. Gell-Mann, H. Fritszch, and H. Leutwyler. .The asymptotically free characteristic of QCD and the scaling behavior in deep inelastic scattering experiment were explained in the work of G. 't Hooft, H. Politzer and F. Wilczek. The discovery of the J/Ψ charmed quark-antiquark bound states at Brookhaven and SLAC in 1974 completely build up the first two families of elementary particles. The experimental evidence of CP-violation suggested the existence of the third family. In 1975 the first third family members of lepton and quark were discovered, first the τ lepton by M. Perl and soon after the bottom quark at Fermilab.

- 1980's The discovery of the gauge bosons, the charged W and the neutral Z bosons at CERN in 1983 proved one important part of the theory, giving the impression that the discovery of the remaining third family members is on the horizon. With the precision measurements of the width of the Z boson at CERN and SLAC, which limits the number of families to three, the hunt for the remaining particles, the top quark, the τ neutrino and the Higgs boson was intensified, but with no success.
- 1990's The continuing effort of verification and testing of the Standard Model showed stunning agreement between experiment and theory. With the discovery of top quark at Fermilab in 1995 and the strong kinematic evidence for the τ neutrino, the hunt is now concentrated on the Higgs boson [1, 2].

The Standard Model of elementary particle physics describes the interaction of fields of various spins and considers particles as field excitations above the vacuum ground state. It includes particles with spin 0, 1/2 and 1 and categorizes them into two groups: fermions of spin 1/2 and bosons of spin 0 (Higgs particle) and spin 1 (gauge bosons). The fermion group is further categorized into three families of quarks (q) and leptons (l). They interact through the three fundamental forces, electromagnetic (EM), weak and strong mediated by photon, W and Z bosons and gluons from the gauge boson group. Their basic properties are shown in Table 1.1, Table 1.2 and Table 1.3. Each particle from the fermion group has its antiparticle counterpart, identified with a bar over the particle symbol. For example, the anti-neutrino $\bar{\nu}$ is the anti-particle of the electron neutrino and $\bar{u}$ is the anti-particle of u quark. The quarks and gluons also have additional degrees of freedom called color charge. There are three color charges, red, green and blue; each quark (and antiquark) can have one of the three different color charges. With the color charge included, the total number of fermions in the Standard Model goes up to forty eight. Also because of color charge, quark and antiquark can only be in a combination that neutralize the color charge. Quark and antiquark are paired in bound states called mesons, and combinations of three quarks are in bound states called baryons. Together quarks and leptons make up the matter in the universe.

Table 1.1

PROPERTIES OF QUARKS IN THE STANDARD MODEL.

Generation	Quark	Mass (Gev/c^2)	Electric Charge	Interaction
I	Up (u)	1.5×10^{-3}-4×10^{-3}	2/3	EM, weak, strong
I	Down (d)	4×10^{-3}-8×10^{-3}	-1/3	EM, weak, strong
II	Charm (c)	1.15-1.35	2/3	EM, weak, strong
II	Strange (s)	8×10^{-2}-13×10^{-2}	-1/3	EM, weak, strong
III	Top (t)	178.1	2/3	EM, weak, strong
III	Bottom (b)	4.6-4.9	-1/3	EM, weak, strong

Table 1.2

PROPERTIES OF LEPTONS IN THE STANDARD MODEL.

Generation	Lepton	Mass (Gev/c^2)	Electric Charge	Interaction
I	Electron (e)	5.11×10^{-4}	-1	EM, weak
I	Electron neutrino (ν_e)	$<$ 3 eV	0	EM, weak
II	Muon (μ)	0.106	-1	EM, weak
II	Muon neutrino (ν_μ)	$<$ 0.19 MeV	0	EM, weak
III	Tau (τ)	1.777	-1	EM, weak
III	Tau neutrino (ν_τ)	$<$ 18.2 MeV	0	EM, weak

The gauge symmetry group of the Standard Model is $SU(3)_C \times SU(2)_L \times U(1)_Y$, where C indicates color charge, L stands for left-handed interaction, and Y is weak hyper-charge defined as Y=2(Q-T_3). Here T_3 is the weak isospin projection and Q is charge.

The $SU(3)_C$ component of group structure of the Standard Model describes the gauge transformation of quark color charges of the strong interaction. It is

Table 1.3

PROPERTIES OF GAUGE BOSONS IN THE STANDARD MODEL.

Particle	Mass (Gev/c^2)	Electric Charge	Force
Photon (γ)	0	0	EM
Gluon (g)	0	0	Strong
W ($W^{\pm}$)	80.43	± 1	Weak
Z (Z)	91.19 MeV	0	Weak

described in the theoretical framework of Quantum Chromodynamics (QCD), a non-Abelian gauge theory. The local invariance of the Lagrangian requires the existence of eight massless spin 1 fields, the gluons, which carry color charges and can interact with each other. The behavior of the color interaction in the distances (infinitesimally small) between quarks give rise to asymptotic freedom and quark confinement effects.

The $SU(2)_L \times U(1)_Y$ component of the Standard Model describes gauge symmetry of a unified electromagnetic and weak interaction. The $SU(2)_L \times U(1)_Y$ symmetry is spontaneously broken in the presence of an additional scalar field giving masses to the two charged bosons $W^{\pm}$ and the neutral Z^0 boson (weak interaction mediators). The scalar field, the Higgs boson H^0, remains as a physical particle, which still eludes the experimental searches. The electromagnetic force mediator, the photon, remains massless.

The Standard Model is a very successful theory, not only strikingly accurate in incorporating observed phenomena, but also correctly predicting a broad range of precision experiments. Typical examples are the prediction of the W and Z bosons as well as their masses, and the prediction of the third family top quark. "The remarkable internal consistency of the theory is both a source of wonder and despair

to those who try to predict the future based on its flaws" [1]. Its most obvious flaw is that it contains no description of the force of gravity. It does not reveal the underlying structure of quarks and leptons. It does not address the existence of fermion masses and their hierarchy. It has no explanation of the extraordinary fine-tuning of parameters to compensate for the quadratic divergence in the Higgs mass. Today there seems no doubt that there is more to the world than just the Standard Model. It is more than likely that the Standard Model is just a part of a more complete, more integrated structure.

1.2 Motivation for this Research

In the Standard Model, quarks and leptons as fundamental building blocks are point-like particles. Looking beyond the Standard Model, one may wonder if this is really the fundamental building block or just a knot in the chain from atom, down to nucleus, further down to nucleons, to quark and lepton and to preon (?). The research in this thesis describes an attempt to look into the more fundamental structure of quarks and leptons at the highest energy scale of present accelerators.

1.3 Organization of the Thesis

This thesis is a part of an ongoing search for quark and lepton compositeness at the DØ detector at the Fermilab Tevatron. This thesis presents in detail the search in the dimuon channel. Chapter 2 gives an brief discussion of the Drell-Yan process in the Standard Model framework and examines a possible physics scenario beyond the Standard Model, where quarks and leptons can be composite. The effect of compositeness on the Drell-Yan process is presented and the current experimental status of studies on compositeness is described. Chapter 3 details the experimental setup used to perform the search for compositeness. Chapter 4 describes the search

for quark and lepton compositeness in the dimuon channel. Conclusions and a summary are given in Chapter 5. The Appendix shows event displays of some interesting candidate events.

CHAPTER 2

THEORIES AND PHENOMENOLOGY

2.1 Drell-Yan Process in Standard Model

The production of dilepton pairs in hadron-hadron collisions was first studied by S.D. Drell and T. M. Yan using parton model ideas and was measured in $pp, \pi^{\pm}p, K^{\pm}p$, and $p\bar{p}$ collisions. The actual process in proton and anti-proton collisions is through quark-antiquark annihilation mediated by a virtual photon γ^* or a Z boson:

$$p\bar{p} \to q\bar{q} \to \gamma^*/Z \to l^+l^-$$

where l is a lepton. The process is illustrated in Figure 2.1. Longitudinal momentum fractions x_1 and x_2 ($0 \leq x_{1,2} \leq 1$) carried by the quark and anti-quark are given by the parton distribution function (PDF). Transverse momenta of the quark and anti-quark are neglected. In the first approximation, the cross section for producing a dilepton (or quark) pair is obtained by multiplying the subprocess cross section $\hat{\sigma}$ for $q\bar{q} \to \gamma^*/Z \to l^+l^-$ by $dx_1 f_q(x_1)$ and $dx_2 f_{\bar{q}}(x_2)$, summing over quark and anti-quark types and integrating over x_1 and x_2; also an average must be made over the colors of quark and anti-quark. The resulting expression is:

$$\sigma(p\bar{p} \to l^+l^-) = \sum_{q,\bar{q}} C_{q\bar{q}} \int dx_1 dx_2 f_q(x_1) f_q(x_2) \hat{\sigma}(q\bar{q} \to l^+l^-) \tag{2.1}$$

where $C_{q\bar{q}} = 1/9$ is the initial color-averaging factor for quark and anti-quark [3, 4].

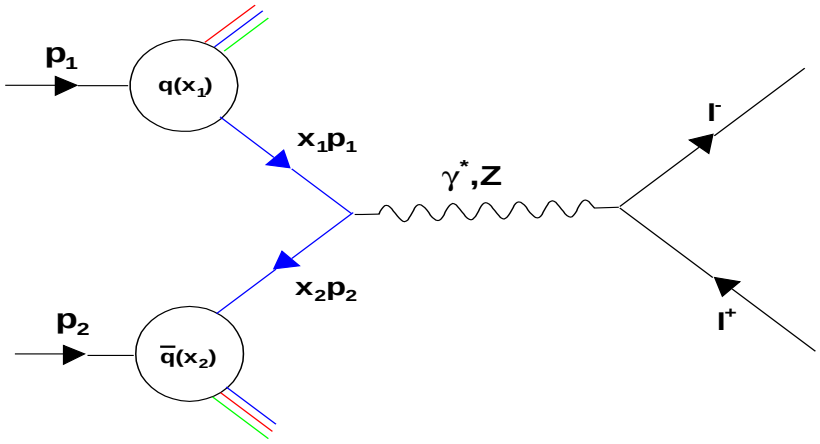

Figure 2.1. Lepton pair production through the Drell-Yan process.

Under the assumption that the transverse momenta of quark and anti-quark can be neglected, the transverse momentum of γ^*/Z should be identically zero. It is not supported by experimental data. However, the difference can be absorbed into higher order corrections to the Drell-Yan process.

In this analysis, the focus is on the Drell-Yan dimuon production process:

$$p\bar{p} \rightarrow q\bar{q} \rightarrow \gamma^*/Z \rightarrow \mu^+\mu^-$$

therefore, in the next section, only this particular channel will be considered.

2.2 Leading Order Calculation of Drell-Yan Cross Section

The production of a dimuon pair from the annihilation of a quark and anti-quark can proceed through an electromagnetic interaction (virtual photon γ^* exchange) or a weak interaction (Z boson exchange). The leading order Feynman diagram is shown in Figure 2.2.

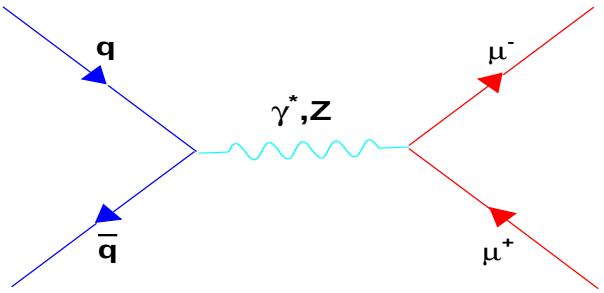

Figure 2.2. Feynman diagrams for dimuon production through the Drell-Yan process.

The scattering amplitude for the electromagnetic interaction is:

$$\mathcal{M}_\gamma = \frac{-ie^2 Q_i}{\hat{s}}[\bar{u}(p_3)\gamma^\mu v(p_4)][\bar{v}(p_2)\gamma_\mu u(p_1)] \tag{2.2}$$

where Q_i is the charge of the i^{th} quark, $e = \sqrt{4\pi\alpha}$, p_1 and p_2 are four momenta of the quark and anti-quark, p_3 and p_4 are four momenta of the μ^- and μ^+, u and v are four-component Dirac spinors for the particle and the antiparticle and $\hat{s}$ is the subprocess energy. The subprocess $q\bar{q} \rightarrow \mu^+\mu^-$ is an elastic collision and $(p_1 + p_2)^2 = \hat{s}$, is equal to the dimuon invariant mass m.

The amplitude for the weak interaction is:

$$\mathcal{M}_Z = \frac{-ie^2}{16 s_w c_w(\hat{s} - M_Z^2)}[\bar{u}(p_3)\gamma^\mu(C_V^\mu + C_A^\mu\gamma_5)v(p_4)][\bar{v}(p_2)\gamma_\mu(C_V^q + C_A^q\gamma_5)u(p_1)] \tag{2.3}$$

with M_Z the mass of Z boson, $s_w = \sin^2\theta_W$, the weak mixing parameter, $c_w = \cos^2\theta_W$, $C_V^{\mu,q} = L^{\mu,q} + R^{\mu,q}$, $C_A^{\mu,q} = -L^{\mu,q} + R^{\mu,q}$, $L_{\mu,q} = 2T_3$-$4Q_{\mu,q}s_w$ and $R_{\mu,q} =$ -$2Q_{\mu,q}s_w$. $Q_{\mu,q}$ are quark and muon charges and T_3 is the weak isospin projection.

The dimuon production cross section will have contributions from the γ^* amplitude $\mathcal{M}_\gamma$, the Z amplitude $\mathcal{M}_Z$ and their interference:

$$d\hat{\sigma}(q\bar{q} \to \mu^+\mu^-) = C|\mathcal{M}_\gamma + \mathcal{M}_Z|^2 \tag{2.4}$$

Assuming that the fermion masses are very small compared to their energy ($m_{\mu,q} \approx 0$), the differential cross section can be calculated from equations 2.2 and 2.3 [5]:

$$d\widehat{\sigma}^{\Lambda}(q\bar{q} \to \mu^+\mu^-) = \frac{\pi\alpha^2}{6\widehat{s}}\left[\frac{A_q + B_q}{4}(1+\cos^2\theta) + \frac{A_q - B_q}{2}\cos\theta\right] d\cos\theta \tag{2.5}$$

where

$$\begin{aligned} A_q &= |Q_q - \tfrac{L_q L_\mu}{4 s_w c_w}\tfrac{\widehat{s}}{\widehat{s}-M_Z^2+iM_Z\Gamma_Z}|^2 \\ &\quad + |Q_q - \tfrac{R_q R_\mu}{4 s_w c_w}\tfrac{\widehat{s}}{\widehat{s}-M_Z^2+iM_Z\Gamma_Z}|^2 \\ B_q &= |Q_q - \tfrac{R_q L_\mu}{4 s_w c_w}\tfrac{\widehat{s}}{\widehat{s}-M_Z^2+iM_Z\Gamma_Z}|^2 \\ &\quad + |Q_q - \tfrac{L_q R_\mu}{4 s_w c_w}\tfrac{\widehat{s}}{\widehat{s}-M_Z^2+iM_Z\Gamma_Z}|^2 \end{aligned} \tag{2.6}$$

2.3 Higher Order Corrections

The higher order corrections are due to virtual and real gluon radiation from quark and anti-quark. The $\mathcal{O}(\alpha_s)$ corrections to the LO Drell-Yan cross section are from the following contributions:

- Virtual gluon corrections.
- Real gluon correction from the process $q\bar{q} \to (\gamma^*/Z)g$
- The quark gluon scattering process $qg \to (\gamma^*/Z)q$ [3]

Figure 2.3 shows a few of the next-to-leading-order diagrams for the Drell-Yan process.

The $\mathcal{O}(\alpha_s)$ correction is calculated and given in terms of the so called K-factor (for NLO). Also the K-factor for NNLO is calculated in [6].

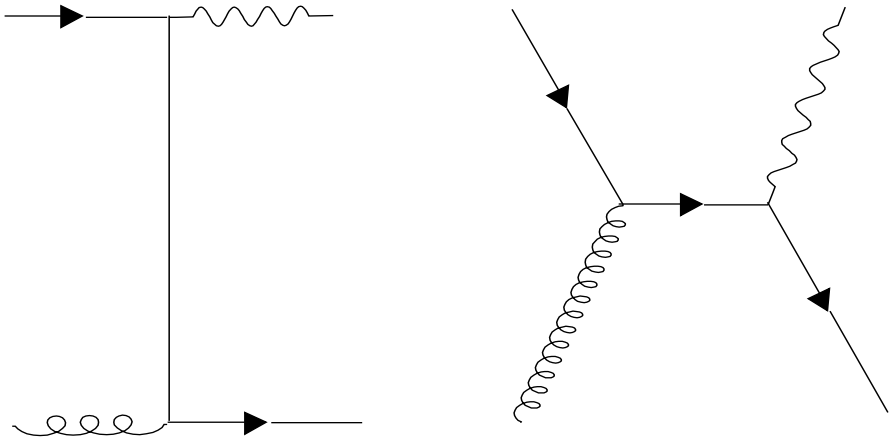

Figure 2.3. Feynman diagrams for next-to-leading-order Drell-Yan process.

2.4 Quark and Lepton Compositeness

In the introduction, there was a brief discussion of the most fundamental building blocks of matter in the universe. Over centuries, the search for the ultimate building blocks of matter has found the smallest point-like particles in historical order from molecules, atoms, down to nucleus, to nucleons and finally to quark and leptons in the current Standard Model framework. Whether it can go further is a natural question to ask. The collision energy at which colliding experiments can run to find a definite indication of this possible quark and lepton compositeness should be at least few times the world's current highest energy at proton anti-proton collider of 2 TeV (because of the lack of experimental evidence of compositeness up to scale of 10^{-16} cm and the high mass of the third family top quark). According to current theoretical ideas, quarks and leptons can be of composite structure i.e., bound states

of more fundamental constituents called preons [7]. The constituent preons interact via new non-Abelian strong gauge interaction called metacolor. The characteristic energy scale, below which the metacolor interaction becomes strong and binds the preons to form metacolor-singlet states like the quarks and leptons, is defined as the scale of compositeness Λ. The scale of compositeness Λ corresponds to the physical size of a quark or lepton, which is in the order of a few TeV.

When the collision energy significantly exceeds the compositeness scale Λ, multiple-parton production processes (e.g $u\bar{u} \rightarrow u\bar{u}u\bar{u}, u\bar{u}l\bar{l}, b\bar{b}t\bar{t}, e^+e^-\mu^+\mu-$) will dominate over the two-body parton scattering process. Unconventional events - multijets, jets with leptons, multi-leptons - will dominate standard model processes. The cross sections for these processes will be geometrical in magnitude, which is of the order of $4\pi/\Lambda^2$, different from $\pi\alpha^2/\hat{s}$ (α is the fine structure constant) of the cross sections of SM processes. On the other hand, if the accessible energy is below the Λ scale, then even though the physics nature may not be evident, the presence of quark and lepton compositeness can still be tested as deviations of the cross section, its energy, and its angular dependence from SM predictions. At this energy quark and lepton compositeness is modeled through a four fermion contact interaction.

The contribution of compositeness to dimuon production is illustrated in Figure 2.4 and modeled in the following effective Lagrangian:

$$\begin{aligned} L_{ql} = \tfrac{g_0^2}{\Lambda^2}\{&\eta_{LL}(\bar{q}_L\gamma^\mu q_L)(\bar{\mu}_L\gamma_\mu\mu_L) + \eta_{LR}(\bar{q}_L\gamma^\mu q_L)(\bar{\mu}_R\gamma_\mu\mu_R) \\ &+\eta_{RL}(\bar{u}_R\gamma_\mu u_R)(\bar{\mu}_L\gamma^\mu\mu_L) + \eta_{RL}(\bar{d}_R\gamma_\mu d_R)(\bar{\mu}_L\gamma^\mu\mu_L) \\ &+\eta_{RR}(\bar{u}_R\gamma^\mu u_R)(\bar{\mu}_R\gamma_\mu\mu_R) + \eta_{RR}(\bar{d}_R\gamma^\mu d_R)(\bar{\mu}_R\gamma_\mu\mu_R)\} \end{aligned} \tag{2.7}$$

where $q_L = (u,d)_L$ is a left-handed quark doublet; u_R and d_R are right-handed quark singlets; μ_L and μ_R are the left- and right-handed muons respectively; and η_{AB} defines the nature of interference between the contact interaction and the SM in the AB channel, with A and B representing the helicities of the quark and the

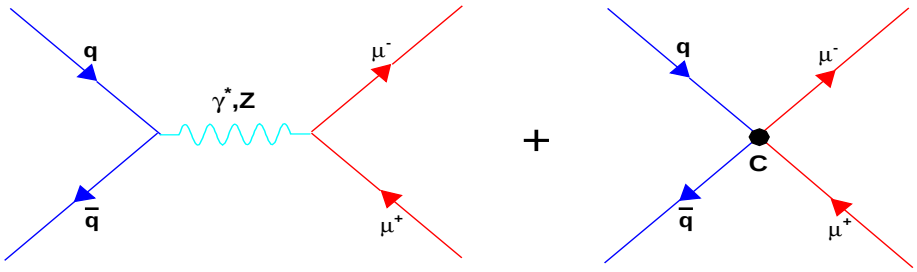

Figure 2.4. Feynman diagrams for dimuon production in the presence of compositeness.

muon currents. The differential cross section can be expressed as [3]:

$$d\widehat{\sigma}^{\Lambda}(q\bar{q} \to \mu^+\mu^-) = \frac{\pi\alpha^2}{6\widehat{s}}\left[\frac{A_q + B_q}{4}(1+\cos^2\theta) + \frac{A_q - B_q}{2}\cos\theta\right] d(\cos\theta) \tag{2.8}$$

where

$$\begin{aligned} A_q &= |Q_q - \tfrac{L_q L_\mu}{4 s_w c_w}\tfrac{\widehat{s}}{\widehat{s}-M_Z^2+iM_Z\Gamma_Z} - \tfrac{\eta_{LL}\widehat{s}}{\alpha\Lambda^2}|^2 \\ &+ |Q_q - \tfrac{R_q R_\mu}{4 s_w c_w}\tfrac{\widehat{s}}{\widehat{s}-M_Z^2+iM_Z\Gamma_Z} - \tfrac{\eta_{RR}\widehat{s}}{\alpha\Lambda^2}|^2 \\ B_q &= |Q_q - \tfrac{R_q L_\mu}{4 s_w c_w}\tfrac{\widehat{s}}{\widehat{s}-M_Z^2+iM_Z\Gamma_Z} - \tfrac{\eta_{RL}\widehat{s}}{\alpha\Lambda^2}|^2 \\ &+ |Q_q - \tfrac{L_q R_\mu}{4 s_w c_w}\tfrac{\widehat{s}}{\widehat{s}-M_Z^2+iM_Z\Gamma_Z} - \tfrac{\eta_{LR}\widehat{s}}{\alpha\Lambda^2}|^2 \end{aligned} \tag{2.9}$$

The dimuon cross section can be expressed as:

$$\frac{d^2\widehat{\sigma}^{\Lambda}}{dmdcos\theta} = \frac{d^2\widehat{\sigma}}{dmdcos\theta}(DY) + \beta I + \beta C^2 \tag{2.10}$$

where $\beta = 1/\Lambda^2$, m is the dimuon invariant mass; I is the interference of DY and the contact term and C is the pure contact term contribution to the cross section.

The total cross section is given by:

$$\widehat{\sigma}^{\Lambda}(p\bar{p} \to \mu^+\mu^-) = \int d\xi_1 d\xi_2 \sum\nolimits_q \left[f_q(\xi_1) f_q(\xi_2) \widehat{\sigma}^{\Lambda}(q\bar{q} \to \mu^+\mu^-) \right] \tag{2.11}$$

The quark-lepton compositeness in the contact interaction model was theoretically studied [3] for various chirality models corresponding to LL, RR, RL and LR terms of Equation 2.7. Combinations of these terms were also studied, which include LL+RR, LR+RL [8, 9], LL−LR [10], vector-vector VV (LL+RR+RL+LR) [11] and axial vector-axial vector AA (LL−LR−RL+RR) [11, 12]. Their coupling coefficients are shown in Table 2.1.

Table 2.1

η_{ij} FOR CONTACT INTERACTION MODE INVOLVING DIFFERENT CHIRALITY TERMS.

Model	η_{LL}	η_{RR}	η_{LR}	η_{RL}
$LL^{\pm}$	±1	0	0	0
$RR^{\pm}$	0	±1	0	0
$LR^{\pm}$	0	0	±1	0
$RL^{\pm}$	0	0	0	±1
$(LL+RR)^{\pm}$	±1	±1	0	0
$(LR+RL)^{\pm}$	0	0	±1	±1
$(LL-LR)^{\pm}$	±1	0	∓1	0
$(RL-RR)^{\pm}$	0	∓1	0	±1
$VV^{\pm}$	±1	±1	±1	±1
$AA^{\pm}$	±1	±1	∓1	∓1

Figure 2.5 shows the theoretical distributions of differential cross section versus dimuon invariant mass for the DY process and for three different values of Λ of 2 TeV, 4 TeV and 8 TeV in the LL channel for constructive and destructive interferences.

The effect of compositeness is pronounced only in the high-mass region above the Z peak.

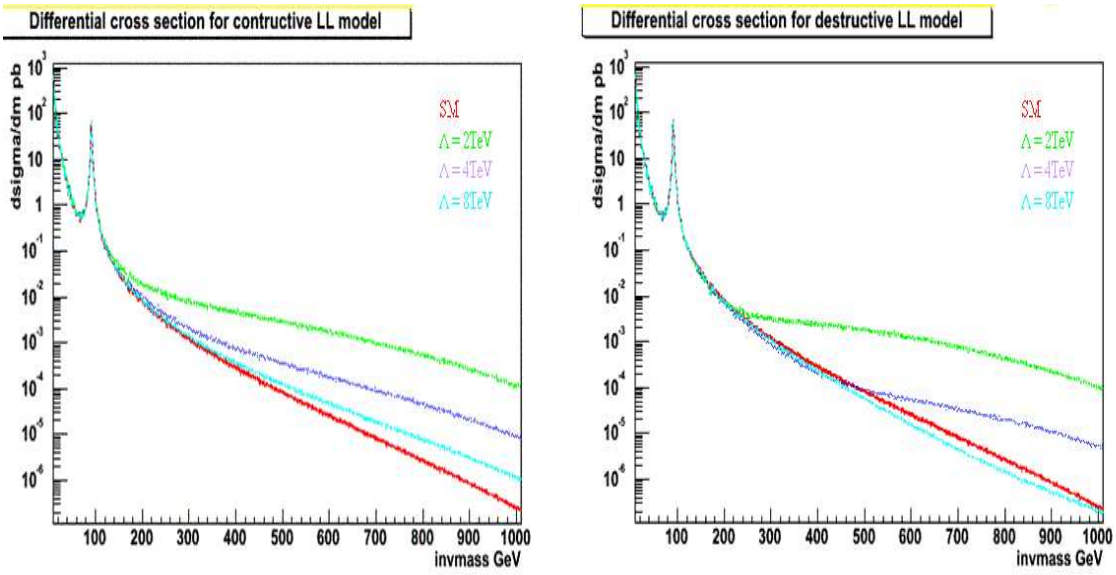

Figure 2.5. Theoretical cross section versus dimuon invariant mass for the DY process and for three different values of Λ in the LL channel for constructive (left) and destructive (right) interference.

Higher order corrections with the inclusion of a contact interaction to the Drell-Yan process has been calculated [19]. The NLO and NNLO K-factors for Drell-Yan plus contact interaction is the same as K-factors for Drell-Yan only.

2.5 Experimental Status

Searches for quark and lepton compositeness have been conducted in various high energy experiments.

- The CDF and DØ experiments at the Tevatron through $qqll$ contact interaction [13, 14].
- The LEP, HERA, Atomic Parity Violation and low energy electron-nucleon experiments through $eeqq$ contact interaction [15, 16, 17].
- The CCFR experiment [18] $qq\nu\nu$ contact interaction. Adapted from [3].

No evidence of significant deviation from SM predictions was found in these experiments. 95 % confidence lower limits on the scale of compositeness $\Lambda^{\pm}$ (Λ^{+} is for constructive and Λ^{-} is for destructive interference) for various chirality channel have been set. Table 2.2 shows a summary of results of 95 % cofidence lower limit from various collider experiments for the LL chirality model for dielectron channels. More recent results from DØ in dielectron channel for various chirality models are shown in Table 2.3 (Run I) and in Table 2.4 (Run II).

Table 2.2

QUARK AND LEPTON COMPOSITENESS SEARCH RESULTS. ADAPTED FROM [3].

Experiment	Λ^{+} (TeV)	Λ^{-} (TeV)
CDF	2.5	3.7
OPAL	3.4	2.2
L3	3.0	2.1
ALEPH	3.9	2.7
Gonzalez *et al.*	3.3	3.7

Table 2.3

DØ RUN I 95% CL LOWER LIMIT ON COMPOSITENESS SCALE Λ FOR DIFFERENT CONSTRUCTIVE AND DESTRUCTIVE CONTACT INTERACTION MODELS IN DIELECTRON CHANNEL. ADAPTED FROM [3].

Model	Λ^+(TeV)	Λ^-(TeV)
LL	3.3	4.2
RR	3.3	4.0
LR	3.4	3.6
RL	3.3	3.7
LL+RR	4.2	5.1
LR+RL	3.9	4.4
LL-LR	3.9	4.5
RL-RR	4.0	4.3
VV	4.9	6.1
AA	4.7	5.5

Table 2.4

DØ RUN II 95% CL LOWER LIMIT ON COMPOSITENESS SCALE Λ FOR DIFFERENT CONSTRUCTIVE AND DESTRUCTIVE CONTACT INTERACTION MODELS IN DIELECTRON CHANNEL. ADAPTED FROM [20].

Model	Λ^+(TeV)	Λ^-(TeV)
LL	3.6	6.2
RR	4.3	5.0
LR	4.5	4.8
RL	3.8	5.8
LL+RR	4.1	7.9
LR+RL	5.0	6.0
LL-LR	4.8	6.4
RL-RR	4.7	6.8
VV	4.9	9.1
AA	5.7	7.8

CHAPTER 3

THE EXPERIMENTAL APPARATUS

The data analyzed in this thesis were collected in 2002, 2003 and 2004 from proton and anti-proton collisions at a center-of-mass energy of 1.96 TeV at the Fermi National Accelerator Laboratory (FNAL) Tevatron and recorded by the upgraded DØ detector.

3.1 Fermilab Accelerator Complex

The Fermilab accelerator complex is currently the world's highest energy particle physics laboratory. In the heart of the lab is the Tevatron, a large particle accelerator in the shape of a ring four miles in circumference. The Tevatron is working in series with other accelerators to produce and deliver proton and anti-proton beams each with energies of 0.98 TeV. These accelerators are: the Cockroft-Walton preaccelerator, the linear accelerator (LINAC), the Booster synchrotron, the Main Injector, the Antiproton Souce, the Tevatron, and the Recycler. Each accelerates the particles passed to it from the preceding accelerator until the particles reach the nominal energy of 0.98 TeV. Running in collider mode, these proton and anti-proton beams collide with a center of mass energy of 1.96 TeV. Figure 3.1 and Figure 3.2 show an aerial view and a schematic view of the Fermilab accelerator complex. Even in their modest simplicity they show how these different accelerators tie together to

produce the collisions. More details of these accelerators are given in the following sections.

Figure 3.1. An aerial view of the Fermilab accelerator complex. Figure courtesy of Fermilab.

3.1.1 Preaccelerator

The Cockroft-Walton is the first accelerator in the Fermilab chain. The preacceleration process consists of two steps. The first step is creation of a proton beam.

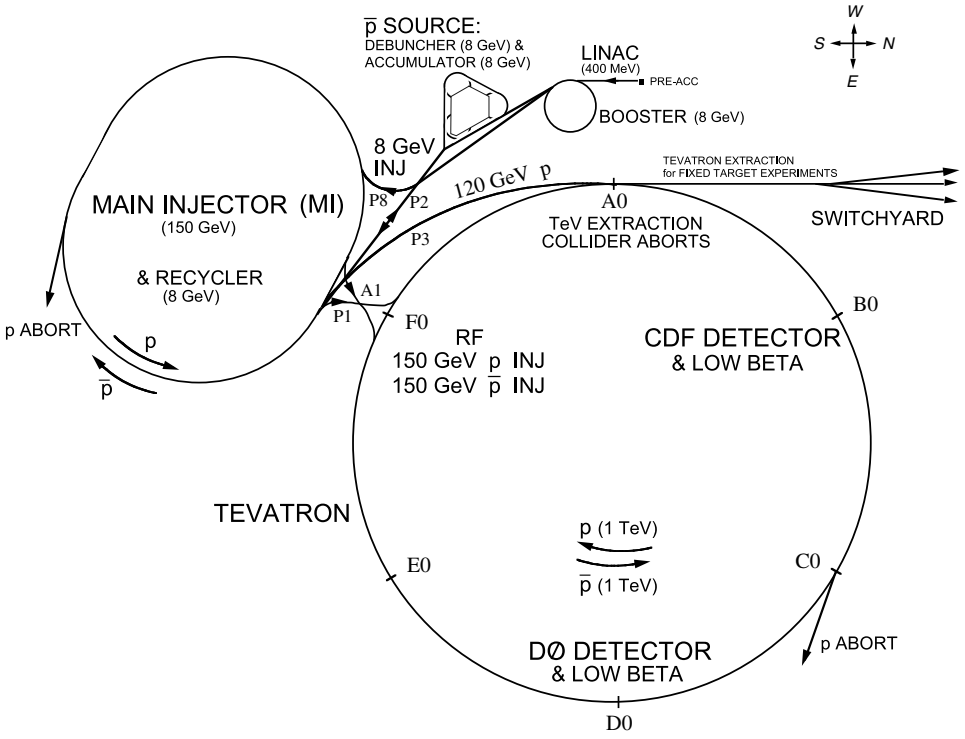

Figure 3.2. A schematic view of the Fermilab accelerator complex. Figure courtesy of Fermilab.

For technical reasons, instead of creating a positive H^+ ion (proton) beam, a negative H^- beam is created. Hydrogen gas is put through a magnetron surface-plasma source. An electric field in the magnetron strips off electrons from the hydrogen molecules, which then are attracted to the cathode's surface. The cathode is made of Cesium metal. The Cesium lowers the work function of the metal, making it easy to free an electron from the cathode. The incoming proton once in a while can smack a proton with two electrons (H^- ion) off the cathode, see Figure 3.3. The magnetic field causes the H^- ions to spiral out the opposite side of the magnetron source. An extractor plate both extracts and accelerates the ions to a kinetic energy of 18 keV [21]. The second step is the acceleration of the H^- ions using the electrostatic Cockroft-Walton accelerator, which raises the H^- ions to an energy of 750 keV.

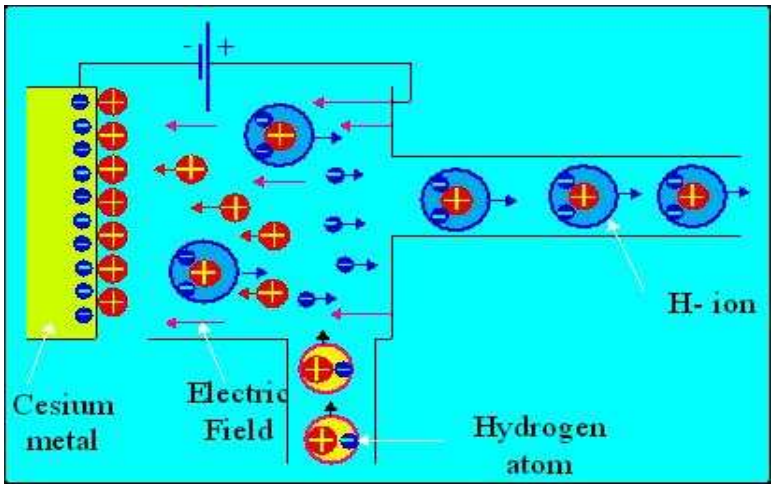

Figure 3.3. Production of H^- ions. Figure courtesy of Fermilab.

3.1.2 The Linac

After leaving the Cockroft-Walton accelerator, the H^- ions are injected into the 500-foot-long linear accelerator, the Linac. The Linac consists of a large series of

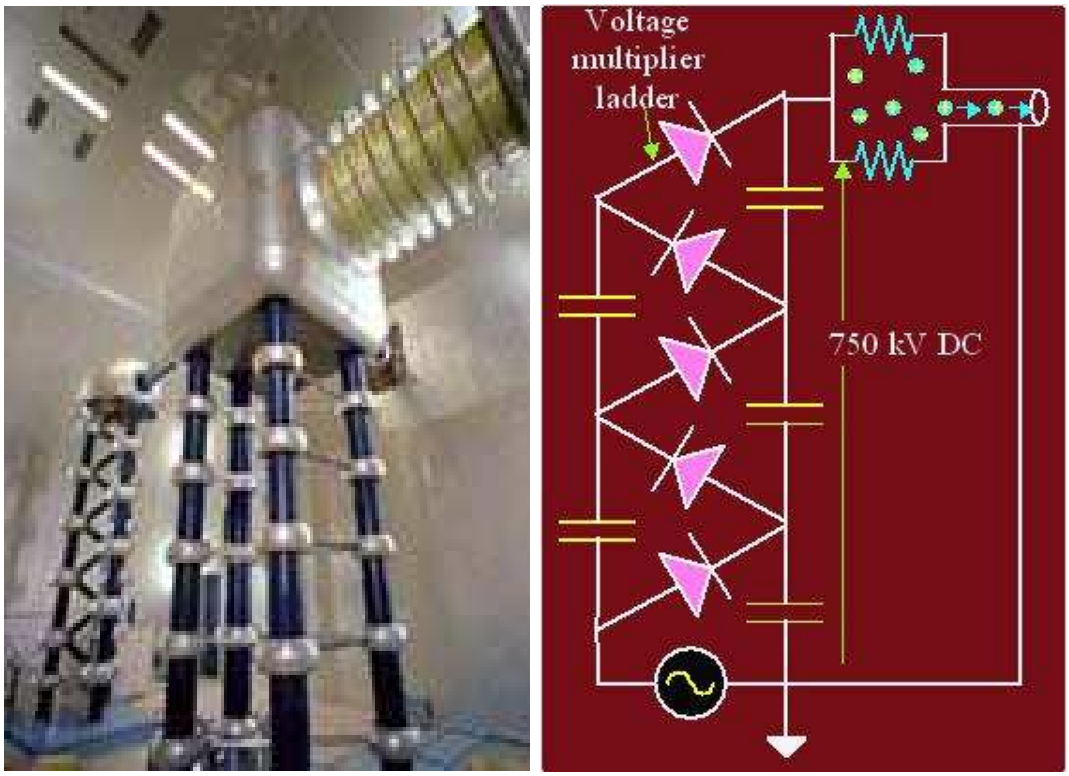

Figure 3.4. An aerial and schematic view of the preaccelerator. Figure courtesy of Fermilab.

repeating plates, as illustrated in Figure 3.5.

At the first stage, the H^- ions are pulled through by the electric field of the plate at the start of the Linac's beam tube. The ions then enter the region between the plates, while the polarity of the electric field is reversed, preventing more ions from entering, and creating a localized bunch of ions. The electric field is reversed again when the ions exit the shielded region and enter the next plate, getting more acceleration. This process is repeated over the 500-foot-long distance. The ions leave the Linac with a kinetic energy of 401 MeV (upgraded from 200 MeV in Run I), ready for the next stage of acceleration. See Figure 3.6 for the actual Linac and [22] for more technical details.

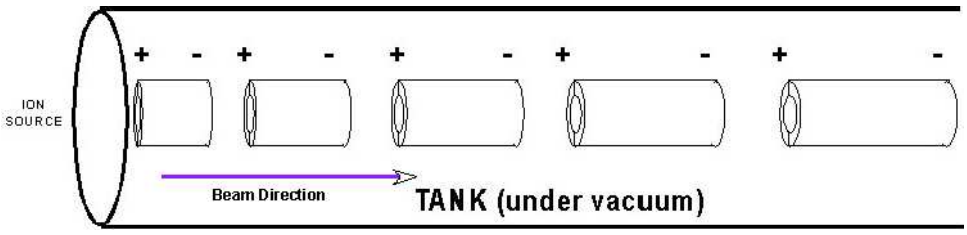

Figure 3.5. Illustration of the Linac. Figure courtesy of Fermilab.

3.1.3 The Booster Synchrotron

The third accelerator is the first synchrotron accelerator that the beam encounters. It is a 1570-foot-circumference synchrotron ring, called the Booster, see Figure 3.7. A debuncher is used to reduce momentum spread of the beam prior to adiabatic capture by the Booster radio frequency (RF) system. As the H^- ion beam leaves the debuncher, it passes through a thin foil of carbon. As the H^- ion passes through the carbon foil, the atoms in the foil interact with the two electrons of the ion and strips them off of the ion. The electrons are discarded, leaving only the bare proton beam.

Dipole magnets in a synchrotron accelerator are used bend the protons and constrain them to a circular orbit, while quadrupole magnets focus the proton beam to keep from diverging. The accelerating fields are formed by a set of RF cavities, which efficiently add momentum to the proton beam as it circles around the ring. The incrementation of both the RF frequency and magnetic field strength are synchronized (characteristic of a synchrotron) to optimally accelerate the proton beam in its circular orbit. The proton beam is formed into a series of about five to seven bunches. Each bunch contains 5-6$\times 10^{10}$ protons. The Booster accelerates the proton beam to an energy of 8 GeV in just 0.033 second (corresponds to 20,000 revolutions around the ring).

Figure 3.6. The Linac. Figure courtesy of Fermilab.

3.1.4 Main Injector

The newly constructed (1999) Main Injector synchrotron is the primary upgrade to the accelerator for Run II, see Figure 3.8. This two-mile-circumference ring replaces the Main Ring that was used in Run I, to solve the mismatches between the Booster, Anti-proton Source and the Main Ring . The Main Injector performs at a significantly higher level than the Main Ring in term of protons delivered per cycle (a factor of three) and transmission efficiency. The Main Injector is located

Figure 3.7. The Booster. Figure courtesy of Fermilab.

tangent to the Tevatron and therefore it reduces the background rates seen in the colliding beam detectors. It also reduces the dead time. The Main Injector accepts seven batches of 8 GeV protons from the Booster and accelerates them to 120 GeV or 150 GeV. The Main Injector performs three functions: deliver the 150 GeV proton beam to the Tevatron and simultaneously deliver a 120 GeV proton beam to the anti-proton production target and a 120 GeV proton beam for fixed-target experiments. It also accelerates the produced anti-proton beam to 150 GeV and then injects that beam into the Tevatron [22].

3.1.5 The Anti-proton Source

At collision energies up to 3 TeV, the production cross section for many processes is higher for anti-proton proton collisions than for that of two proton beams. That is one reason why the Tevatron collider is chosen to be a proton anti-proton ($p\overline{p}$) collider. The task of designing and building an anti-proton source is much more

Figure 3.8. Main Injector. Figure courtesy of Fermilab.

difficult and expensive than that of a proton source. The primary limiting factor for the Tevatron luminosity is the intensity of the $\overline{p}$ beam. As mentioned in the previous subsection, a part of the 120 GeV proton beam from the Main Injector is used to produce the anti-proton beam. A beam of 120 GeV protons from the Main Injector is smashed on to a 10 cm diameter, 2 cm thick disk made of nickel [23] every 1.5 seconds. There are many particles created from the proton-Ni collision, but only about twenty 8 GeV anti-protons for every million protons that hit the target make it into the Accumulator. The anti-protons are focused into a beam line by a cylindrical collection lens made of lithium. The unwanted secondary particles are filtered away by sending the beam through a pulsed dipole magnet. Figure 3.9 helps to illustrate the setup described above.

The anti-protons coming off target are bunched and have very large energy spread. This large energy spread creates inefficiencies in transferring anti-protons to the Accumulator. The Debuncher, an accelerator contained in the same tunnel

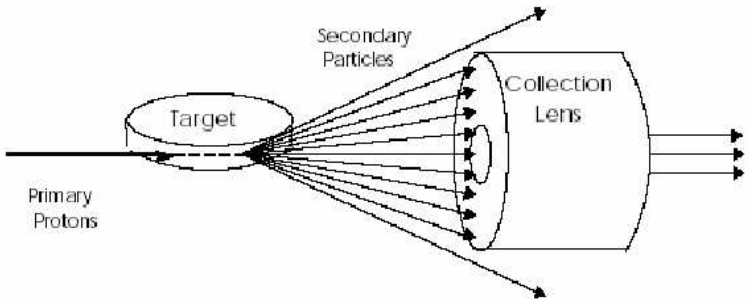

Figure 3.9. Anti-proton production. Figure courtesy of Fermilab.

as the Accumulator, is designed to change the large energy spread and narrow time spread into a narrow energy spread and large time spread. The Debuncher RF cavity causes the anti-protons to feel different RF phases depending on their energies. The low energy anti-protons are accelerated and the high energy anti-protons are decelerated. This process repeats over and over, causing the spread in energy to be reduced. The Accumulator accumulates the anti-protons and arranges them into bunches with the same structure as the protons in the Main Injector [23], see Figure 3.10. This is accomplished by momentum stacking successive pulses of anti-protons from the Debuncher, using RF cavity and stochastic cooling systems. It is done in several hours or days to get accumulating stacks of 10^{12} anti-protons for use in Run IIa. The stack of the anti-protons is then transferred into the Main Injector for acceleration to 150 GeV and injection into the Tevatron.

3.1.6 The Tevatron

The Tevatron is the last in the chain of accelerators. It accelerates the 150 GeV beams of protons and anti-protons delivered from the Main Injector up to an energy of 0.98 TeV. It utilizes superconducting magnets with combined magnetic fields of 4 Tesla and a circumference of 4 miles to achieve the world most energetic proton

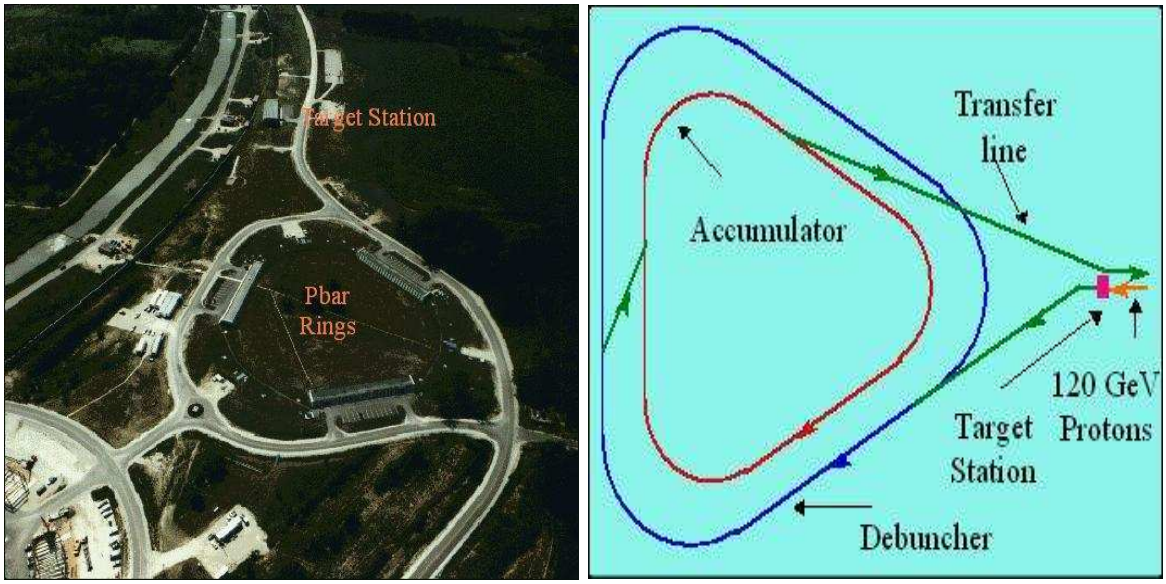

Figure 3.10. An aerial and schematic view of the anti-proton source. Figure courtesy of Fermilab.

and anti-proton beams. Low-beta quadrupole magnets help squeeze the beams to small transverse dimensions and let them cross each other at the designated centers of the 5000 ton Collider Detector Facility (CDF) and DØ detector, located inside the Tevatron tunnel.

The final Tevatron beams are not continuous. The Tevatron beams have protons and anti-protons grouped into bunches with a certain time structure. The Tevatron operates in a 36×36 $p\overline{p}$ bunches mode, with a bunch spacing of 396 ns during Run IIa. A plan to reduce the bunch spacing to 132 ns is designated for Run IIb.

Table 3.1 details some of the Tevatron operation parameters for RunII. Table 3.1.6 summarizes the above mentioned accelerators used at Fermilab.

3.2 The DØ Detector

The DØ detector, a nearly-hermetic multipurpose particle detector, was first proposed in 1983 and started to operate in 1992. It weighs 5500 tons and is 43 feet

Table 3.1

FERMILAB TEVATRON OPERATING PARAMETERS.

Parameters	Run IIa	Run IIb
Typical Luminosity ($\times 10^{32} cm^{-2} s^{-1}$)	0.25	5.2
Integrated Luminosity (pb^{-1}/week)	6	105
Energy (GeV)	980	980
Bunches	36×36	140×108
Proton	2.7×10^{11}	-
Antiproton	7×10^{10}	-
Bunch Spacing (ns)	396	132
Crossing (ns)	2.3	4.8

Table 3.2

FERMILAB ACCELERATOR COMPLEX.

Accelerator	Initial Energy	Final Energy	Acceleration time (s)
Cockroft–Walton	0	750 keV	1.6×10^{-7}
LINAC	750 keV	410 MeV	8×10^{-7}
Booster	410 MeV	8 GeV	0.033
Main Injector	8 GeV	150 GeV	1
Tevatron	150 GeV	980 GeV	20

in height, 35 feet in width and 56 feet in length. The detector is designed to optimize the study of high-mass and large p_T phenomena. Since it initial operation, the detector has been a key contributor to modern experimental high energy physics. An unprecedented example is the discovery of the top quark in 1995 (together with CDF) [24, 25]. A detailed description of the Run I DØ detector can be found in [26].

For Run II, the DØ detector has gone through a major upgrade which builds on strengths of the detector (full coverage in calorimetry and muon detection) while

enhancing the tracking and triggering capabilities. Figure 3.11 gives an overall view of the upgraded DØ detector. A completely new inner-tracking system consists of a silicon vertex detector, surrounded by eight layers of scintillating fiber tracker, installed along with a new superconducting solenoid magnet of 2 Tesla. The upgrade of the calorimeter system is basically only in the readout electronics, whereas the upgrade of the muon systems is in both hardware and electronics for readout. To cope with the higher event rates and complexity, the data acquisition systems were completely upgraded.

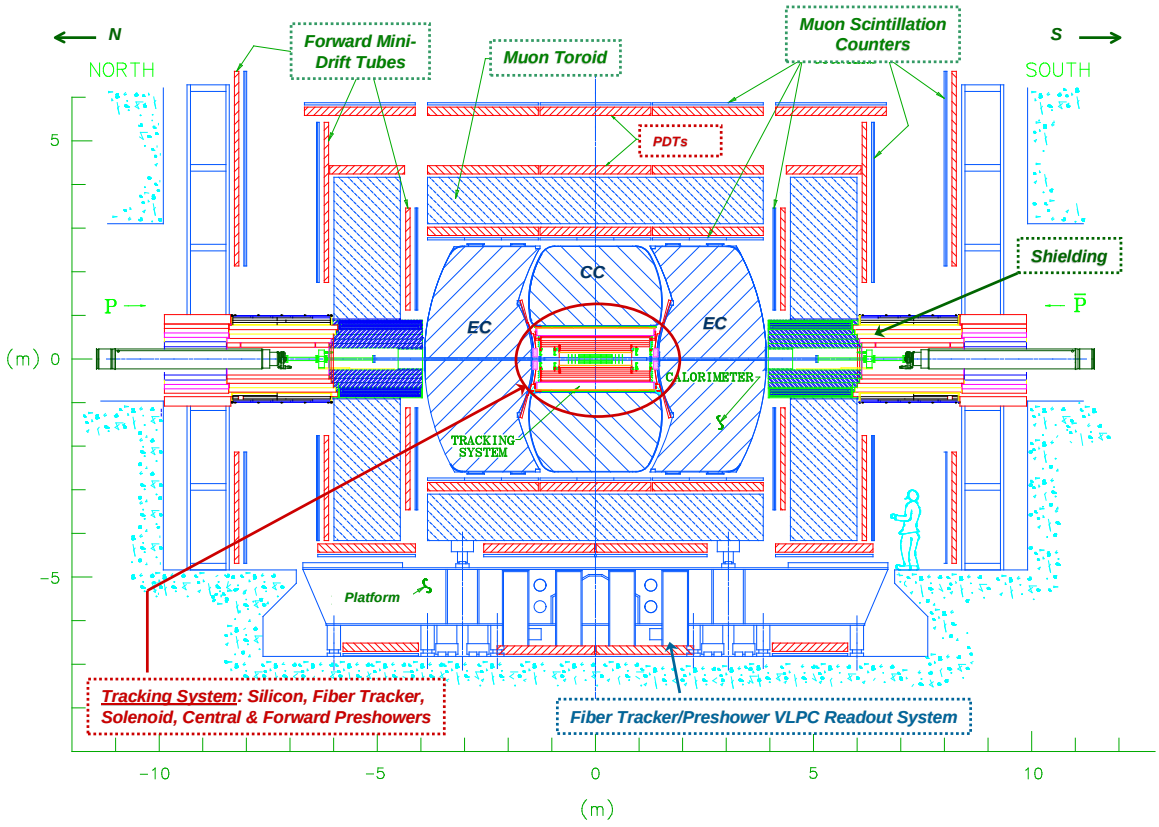

Figure 3.11. Side view of the Run II DØ detector. Adapted from [28].

With the upgraded detector, the physics capabilities of DØ have been expanded

considerably to utilize the new technologies now included in the detector. For example, the B-physics program can now be competitive (with CDF), with the new tracking system; the top quark, W and Z bosons, as well as perturbative and non-perturbative QCD programs are considerably enhanced [27]. The upgrade also extends the search for new particles, searches for the Higgs boson, and other manifestations of new phenomena beyond the Standard Model such as quark and lepton compositeness as in this analysis.

The following sections examines the details of different subsystems of the Run II DØ Detector (relevant to this analysis). For a full list of DØ detector components, see [22, 26] .

3.2.1 DØ Coordinate Systems and Kinematic Variables

DØ uses a standard right-handed coordinate system with the positive $+z$ axis in the direction of the proton beam. The $+x$ axis is defined to be a vector pointing radially outward from the center of the DØ detector. The positive $+y$ axis is defined to be pointing vertically up. The anti-protons travel in the negative $-z$ direction. At DØ the angular coordinates (azimuthal ϕ, and polar θ) are used. The azimuthal angle ϕ is defined as the angle around the $+z$ axis such that $\phi = 0$ in the $+x$ direction and $\phi = \pi/2$ in the $+y$ direction. The polar angle θ is measured from the $+z$ axis. Radial distances are measured perpendicularly to the beam line. Figure 3.12 illustrates the use of the coordinates.

The kinematic variable called rapidity, y^r, is defined as

$$y^r = \frac{1}{2} ln \left[\frac{E + p_z}{E - p_z} \right]. \tag{3.1}$$

It is used instead of the polar angle θ because of the Lorentz invariant property of its intervals. The shape of the particle distribution (dN/dy^r) for example is invariant under boosts along the z-axis.

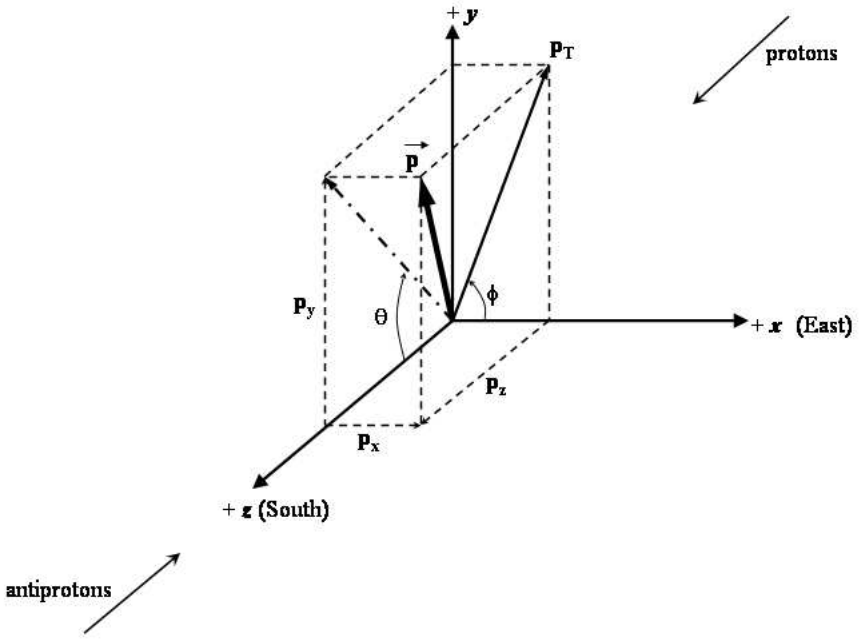

Figure 3.12. The DØ coordinate system. Adapted from [21].

For ultra-relativistic particles it is more convenient to use pseudo-rapidity, η, defined as:

$$\eta \equiv -ln\,[tan(\theta/2)] = \tanh^{-1}(\cos\theta). \tag{3.2}$$

It approximates the true rapidity y in the limit $m/E \to 0$.

Other kinematic variables commonly used at DØ are transverse energy (E_T) and transverse momentum (p_T), where $E_T = Esin\theta$ and $p_T = psin\theta$. They are used instead of total energy E and momentum p partly because of detector ability and partly because of the fact that in $p\overline{p}$ collisions the center-of-mass energy ($\sqrt{s}$) is often not a relevant variable [29]. This is consequence of the parton (quark and gluon) structure of the nucleons being collided. The partons carry only a fraction of the total nucleon energy. Therefore the scattering of these partons (of different energies) results in a center-of-mass frame not coincident with the lab frame. The

total energy of the parton-parton is only a fraction of the total beam energy. Energy balance cannot be used to analyze the outcome of the collision, since a significant portion of the energy is carried away by nucleon remnants (called spectators) down the uninstrumented beam pipe. Hence, transverse energy balance is used because the total transverse energy before the collision is known to be zero. The detectors are also specifically designed to measure nearly all of the transverse energy from the collision.

At DØ , the x and y dimensions of the colliding beams are constrained to be very small, but in the z dimension, it is not as constrained. The primary interaction point has a Gaussian distribution in the z coordinate with mean at $z = 0$ and $\sigma_z =$ 28 cm. Therefore, another pseudo-rapidity, the detector pseudo-rapidity, η_d is used at DØ . The η_d is computed with respect to an interaction point at the center of the DØ detector and whose longitudinal position is set to $z = 0$ [21]. The Gaussian distribution of real interaction points around $z = 0$ causes a slight difference between η and η_d, see Figure 3.13.

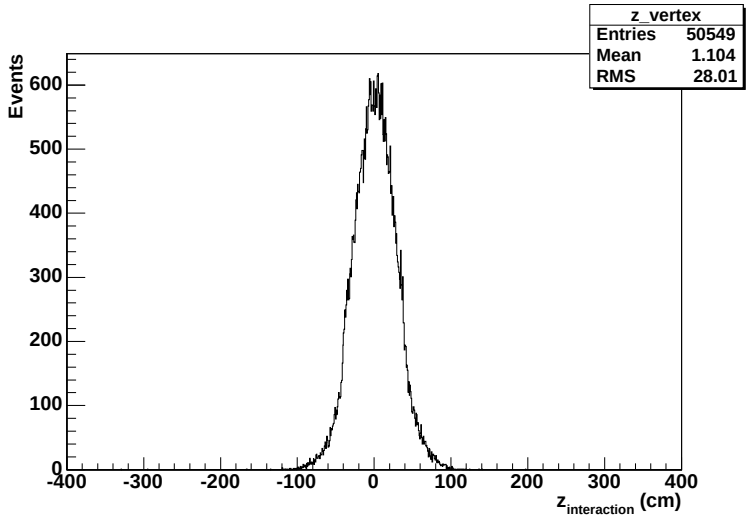

Figure 3.13. Distribution of the interaction point in z-axis.

3.2.2 Solenoid

A superconducting solenoid magnet, which provides a field of 2 Tesla parallel to the beam direction, was installed in the bore of the Central Calorimeter (CC) cryostat. With the solenoid, the charge and momentum of a charged particle can be determined from the curvature of the track in the new central tracking system.

3.2.3 The Central Tracking System

The completely new tracking system consists of two subsystems: the Silicon Microstrip Tracker (SMT) and the Central Fiber Tracker (CFT). The tracking system is designed to achieve several goals: charged particle detection over a large range of pseudo-rapidity ($|\eta| \leq 3$), precision momentum measurements in the solenoidal magnetic field and secondary vertex measurements for the identification of heavy flavors. Figure 3.14 gives an overview of the tracking system.

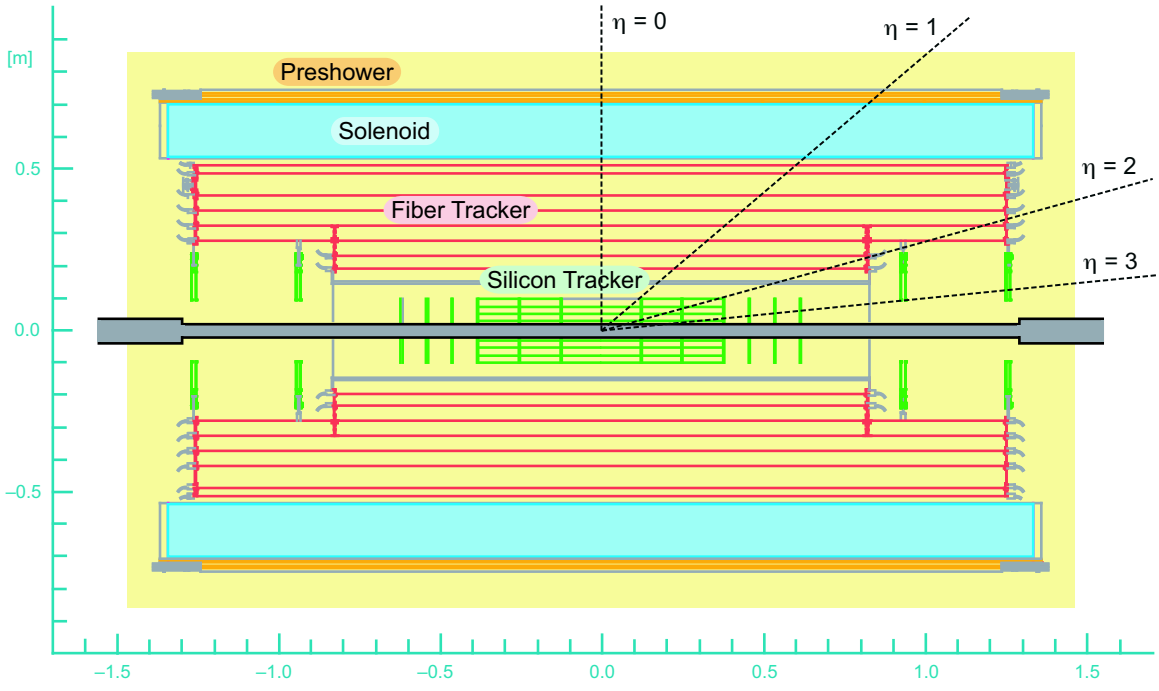

Figure 3.14. The DØ tracking system. Adapted from [30].

The Silicon Microstrip Tracker

The Silicon Microstrip Tracker is the highest resolution sub-detector of DØ and also the one closest to the interaction region. It is the first part of the DØ detector encountered by the particles emerging from the collisions. The following properties of the silicon are taken into consideration when choosing silicon semiconductor tracking:

- low ionization energy (good detectable signal).
- long mean free path (good charge collection efficiency).
- high mobility (fast charge collection).
- low Z (low multiple scattering).
- well-developed technology [27].

(limiting factors are high cost and low radiation resistance of silicon).

Due to the structure of the colliding proton and anti-proton bunches, the interaction point is Gaussian distributed over the z coordinate with mean at $z = 0$ and $\sigma_z = 28$ cm. Therefore, it is difficult to deploy detectors so that particles traverse them at near normal incidence for all η. The hybrid design using barrel (measures primarily the $r - \phi$ coordinate) and disk (measures $r - z$ and $r - \phi$) geometries made from silicon micro-strip detectors provides a solution. In this type of system, the tracks for high η particles are primarily reconstructed by the disks, while the tracks for lower η particles are found with the barrels. The disk and barrel design is shown in Figure 3.15. Conceptually they have the same structure. Their basic unit consists of:

- Silicon microstrip sensor.
- SVX II front end readout chips.
- High density interconnect (HDI) circuit with Kapton strip cable.
- Supporting Rochacell-carbon and beryllium components [27].

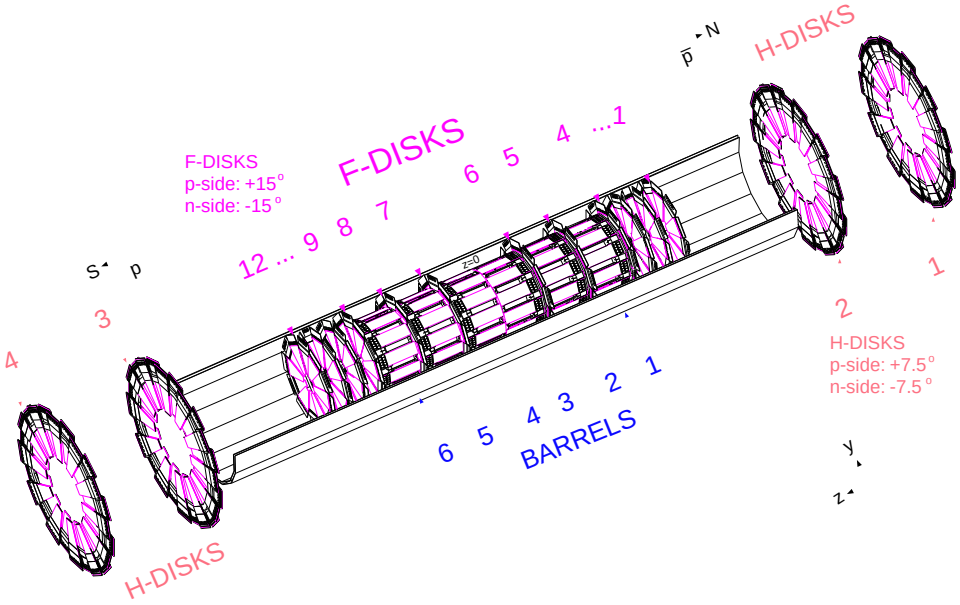

Figure 3.15. The SMT structure. Adapted from [28].

The main part of the SMT is formed by six barrel units. Each barrel, 12.4 cm in length, consists of four concentric layers. The layers are made from silicon ladders with radii ranging from 2.6 cm to 10.0 cm. Layers two and four of all barrels include double-sided small-angle (2 degree) ladders with a 62.5 μm pitch. Layers one and three of the central four barrel modules are double-sided large-angle (90 degree) ladders with a 153.5 μm pitch. Layers one (closest to the beam pipe) and three of the outer two barrels have a 50 μm pitch single-sided ladders. The gap between barrels is small to maintain a high acceptance for low rapidity tracking.

The F-disks, which are interspersed within the barrels are twelve 8 mm-thick disks. Each disk consists of twelve double-sided wedges alternating around a thin cooling channel. To get an effective 30 degree stereo angle, the readout strips on the two sides are placed at $\pm$15 degrees with respect to the symmetry axis of the wedge. The four large area H-disk assemblies with 24 single-sided silicon wedges with a

pitch of 81 μm, are mounted further out from z=0 on both sides to the extreme end of the detector. The H-disks help to maintain a uniform momentum resolution and to extend tracking coverage out to $|\eta|$=3 [28].

The ladders are mounted on beryllium bulkheads to form concentric layers surrounding the interaction point. These bulkheads not only provide structural support, but also serve as an enclosure for the coolant system to keep the operating temperature of 5-10 ^oC [31], see Figure 3.16 and Figure 3.17.

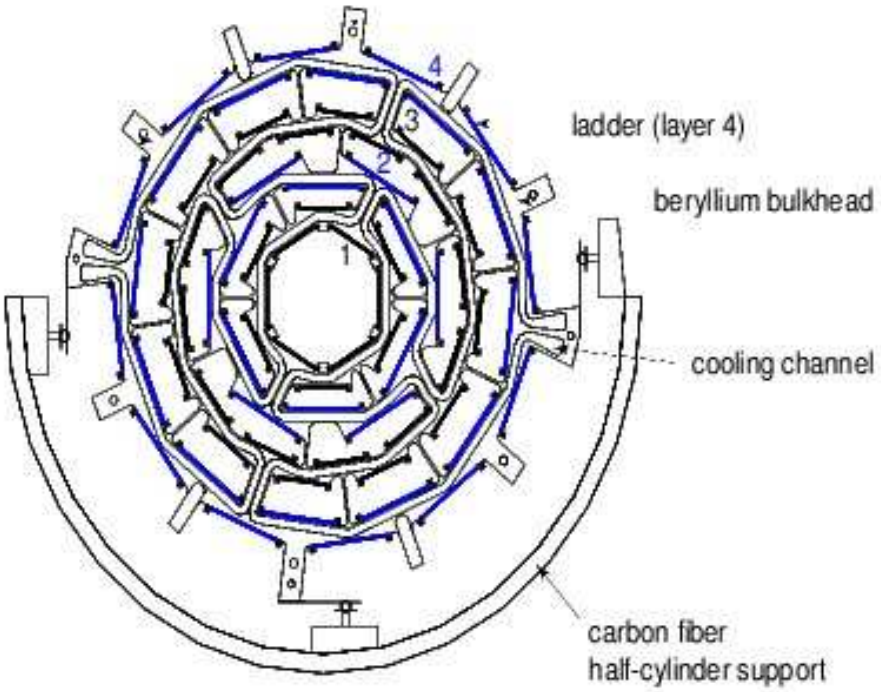

Figure 3.16. A $x-y$ view of the bulkhead. Adapted from [27].

The SMT detector with its 792,576 readout channels is a complicated system with a high level of performance. With an $r\phi$ hit resolution of approximately 10 μm, the SMT helps achieve two goals for the experiment, which have large impact on a number of Run II physics studies. First, it enables the identification and

Figure 3.17. A bulkhead with two ladders. Adapted from [27].

reconstruction of vertices displaced from the primary vertex. An illustration of their finding is shown in Figure 3.18. Second, the hit resolution boosts the momentum resolution for very high p_T tracks. Secondary vertex finding is very important for heavy flavor physics, and good high momentum resolution is equally important for physics searches involving high mass particles as in this analysis.

The Central Fiber Tracker

The Central Fiber Tracker surrounds the SMT as the outer tracking system [32], which covers the central pseudo-rapidity region as shown in Figure 3.19. The CFT serves two main functions:

- Combined with the SMT, it allows efficient track reconstruction and momentum measurement for all charged particles going through the detector within the range $|\eta| < 2.0$. Since the CFT has bigger transverse size, it improves the overall tracking quality, and enhances the charge and p_T resolution of the track.

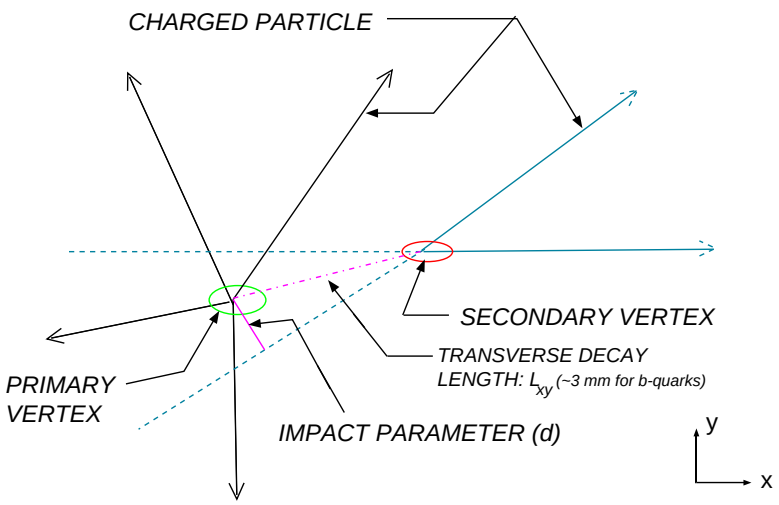

Figure 3.18. Secondary vertex finding. Adapted from [28].

- It provides fast Level 1 track triggering for the range $|\eta| < 1.6$.

The CFT consists of approximately 78,000 scintillating fibers that completely cover eight concentric support cylinders occupying the radial space from 20 to 51 cm and providing full coverage in the central region up to $|\eta| < 1.7$, see Figure 3.19. The inner two cylinders are 1.7 m long and the outer six cylinders are 2.5 m long; such a design accommodates the silicon H-disk detectors located at high-η. Each cylinder is covered by two doublet layers of scintillating fibers. A doublet layer is made from two monolayers of fibers placed in such a way that one layer of the doublet is offset by one half of the fiber spacing with respect to its partner. This configuration provides a compensation for geometric gaps between adjacent fibers in a monolayer, minimizes the dead region, improves the spatial resolution and provides a near unity detection efficiency per doublet layer. The first doublet layer on each cylinder is oriented with the fibers in the axial direction (*i.e.* parallel to the beam line). Another doublet layer is mounted on top of the axial layer at alternating u or v stereo angles of approximately 3 degrees. The u or v stereo angles are alternating

on successive cylinders, so from the inner to outermost cylinder the orientations for the layers are *xu-xv-xu-xv-xu-xv-xu-xv*, where x is the axial doublet layer, see Figure 3.19 [21].

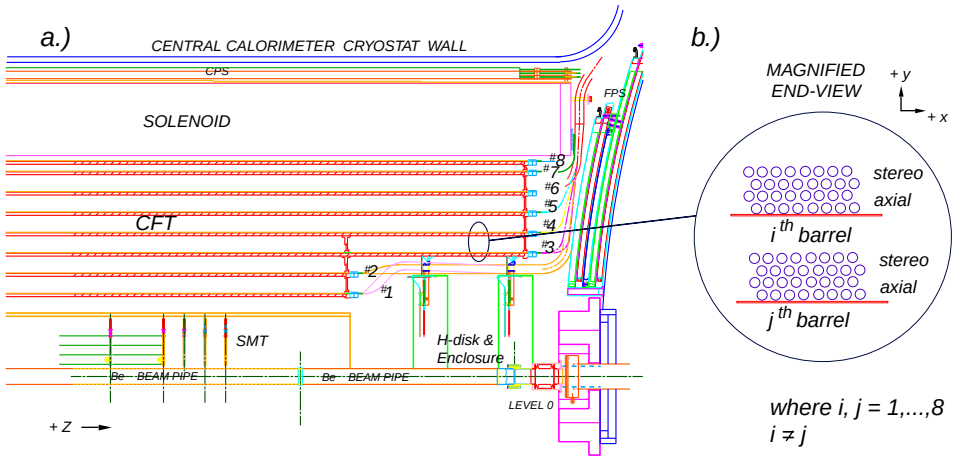

Figure 3.19. A quarter $r-z$ view of the CFT detector with a magnified $r-\phi$ end view of the two ribbon doublet layer configuration for two different barrels. Adapted from [28].

During assembly, fibers are grouped into ribbons. Each fiber ribbon consists of 256 fibers in two layers of 128 fibers. Ribbons are mounted onto the carbon fiber cylinders with an accuracy better than 40 μm [33]. This can help preserve detector resolution and provide enough granularity for detecting tracks and triggering. Figure 3.20 shows data using representative CFT ribbons in a cosmic ray system test and indicates a doublet position resolution of $\approx$ 100 μm for single muons [28].

Each scintillating fiber used in the CFT has a 775 μm diameter fluorescent polystyrene core doped with 1% P-terphenyl (PT) and 1500 ppm 3-hydroxyflavone (3HF) having peak scintillation at 530 nm (yellow-green part of visible light) and surrounded by two thin 15 μm claddings, the inner made from acrylic and the outer from fluoro-acrylic material [34]. The lengths of these fibers range from 166 to 252

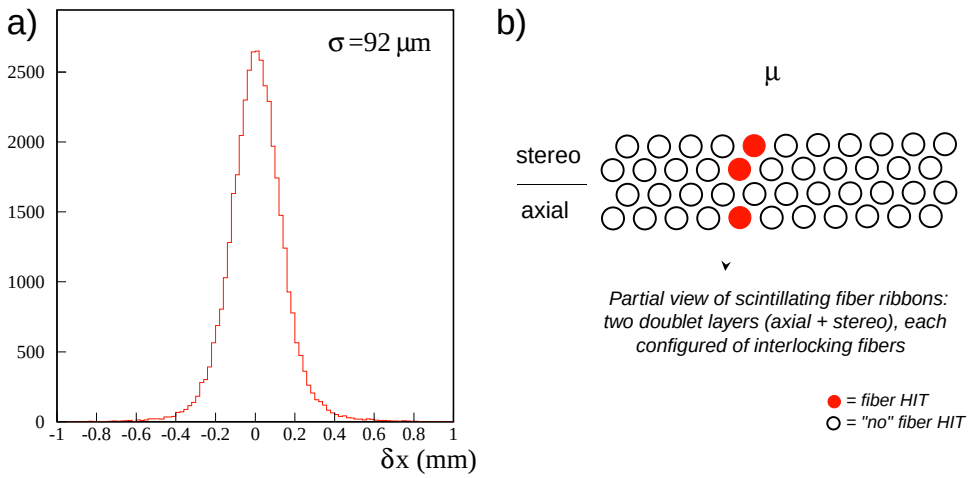

Figure 3.20. a) Distribution for the position resolution measured in the CFT cosmic ray system test. b) An interlocking doublet ribbon configuration. Adapted from [28].

cm.

Figure 3.21 illustrates the basic principle of scintillating fiber trackings.

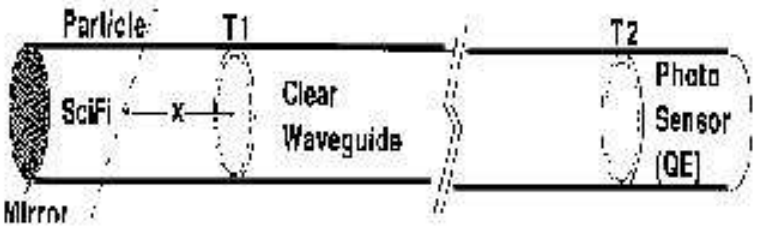

Figure 3.21. Schematic of fiber-tracking element. Adapted from [35].

Charged particles going through the scintillating fiber deposit energy by ionization, a fraction of which is converted into light. A portion of this light is optically trapped inside the fiber, and travels toward an end of the fiber. At one end of the scintillating fiber, there is an aluminum mirror coating that reflects the incoming light back into the fiber. At the other end, the light is collected and transmitted into

the readout portion of the CFT. At this end the ribbon of 256 fibers is inserted into a custom-machined diamond-finished optical connector. The connector is mated to a clear waveguide bundle of 256 fibers. The end of this bundle has also been diamond-finished and equipped with a matching optical connector. The fibers making up this waveguide are structurally and chemically the same as the scintillating fibers, but without fluorescent dyes. The clear fibers are grouped together and contained in a flexible plastic tube, which provides them physical and light protection. Lengths for the waveguides (for CFT) range from 7-12 meters, allowing the light to be transfered to the readout platform, outside the central detector area.

At the read out platform, the waveguides are connected to a series of rectangular modules called cassettes which are set into a liquid helium cryostat [21]. The optical signal is transported through the cassettes to a set of highly sensitive silicon-avalanche photodiodes, known as Visible Light Photon Counters (VLPCs) [34]. The VLPC converts the scintillation light from the CFT into an electrical signal which is sent to the front-end electronics boards for digitization and readout. The VLPCs have quantum efficiency of over 80 %, a gain of 20,000-50,000, a rate capability of at least 20 MHz, and a noise rate of less than 0.1 %. To achieve these characteristics and to have low noise, the VLPCs operate at a cryogenic temperature of 6–15K [32].

Figure 3.22 shows a Spectrum of ADC counts from a VLPC when there is no signal and when there is one. It shows a clean separation of the pedestal (no signal), first, second and third photoelectron peaks.

The CFT readout electronics is almost identical to that of the SMT readout electronics. The VLPC charge signal is sampled by a discriminator called the SIFi Trigger (SIFT) chip and simultaneously pipelined to a Silicon VerteX II (SVX-II) chip. The VLPC signal is also sent to a special "precursor" chip between the VLPC and the SVX-II, a part of the CFT trigger system. This signal is stored in the

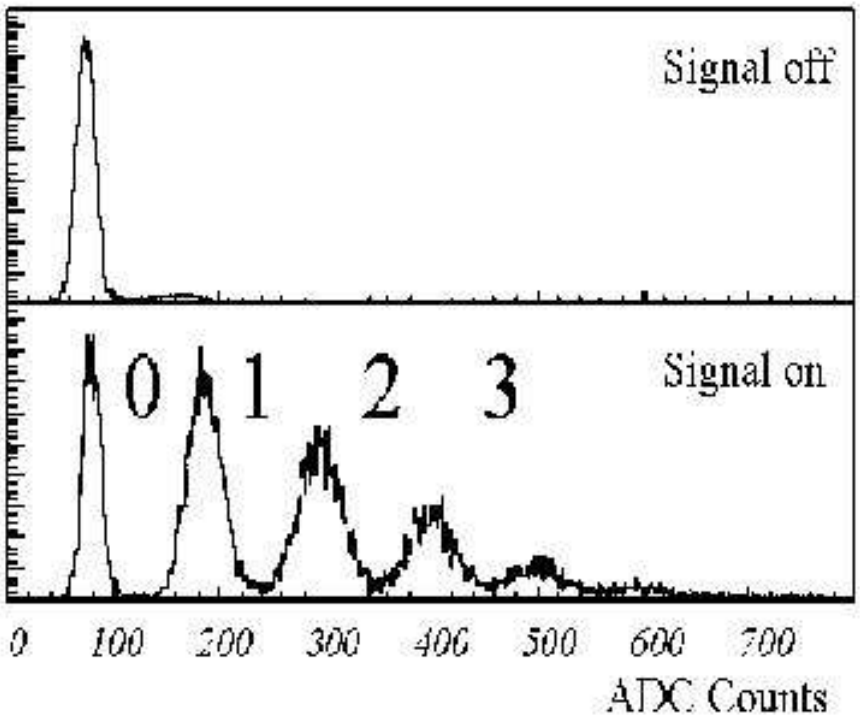

Figure 3.22. Spectrum from a VLPC. Adapted from [35].

SVX-II chip until a trigger decision is made or 32 beam crossings have passed since the signal was produced. The SVX-II digitizes the signal and reads it out, on a Level 1 trigger-accept. The tracker is divided into 80 equal azimuthal sectors for parallel processing in order to speed up this process. The SVX readout information gets appended with the SIFT discriminator pattern, which caused the readout. If no trigger decision is made or 32 beam crossings have occurred, the information is discarded. The Level 1 CFT trigger is implemented using field programmable gate arrays (FPGA). First, only signals from axial layers are used as hits for the trigger. Coincidences between hits on all eight layers form a track. Finally the tracks are combined with triggers from other parts of the detector, such as the

central preshower clusters to form an electron trigger, or the muon system to form a muon trigger. On a Level 1 trigger accept, all the fiber layers will then be read out [21].

3.2.4 The Preshower Detectors

A new set of detectors, preshower detectors, are mounted just beyond the tracking system. The preshower detectors are based on identical scintillation fiber technology as that of the CFT. They are designed to aid in electron and photon identification and triggering and to correct the electromagnetic energy for losses in the solenoid by providing early energy sampling for particles having just traveled through. In this manner they function as a calorimeter. They also function as an additional tracker by providing precise position measurements.

The Central Preshower Detector

The Central Preshower Detector (CPS) functions both as a calorimeter and a tracker in the central region [36]. This detector, as shown in Figure 3.23, is cylindrical in geometry with a radius of 72 cm and is mounted in the nominal 51 mm gap between the solenoid coil and the central calorimeter cryostat. It covers the region of -1.2 $< \eta <$ 1.2. The detector consists of three concentric cylindrical layers of scintillating strips arranged in axial (the innermost layer) and stereo (the two outer layers) views. The *u,v* stereo angles are $\pm$22.5 degrees. The scintillating strips are about 2.6 m long, with the wavelength-shifting (WLS) fibers split at $z = 0$ to effectively double the segmentation along the beam direction. The saw-tooth form of the strip is used to improve position resolution when light-sharing information between adjacent strips is used, see Figure 3.23. The WLS fibers are connected to clear fiber optics to transmit scintillation light from the CPS to the VLPC system. There are 48 bundles of clear fibers and a total of 7680 channels of readout in the CPS. The

readout from the CPS axial layer is integrated with the CFT readout as a ninth layer and used in the Level 1 electron trigger [28].

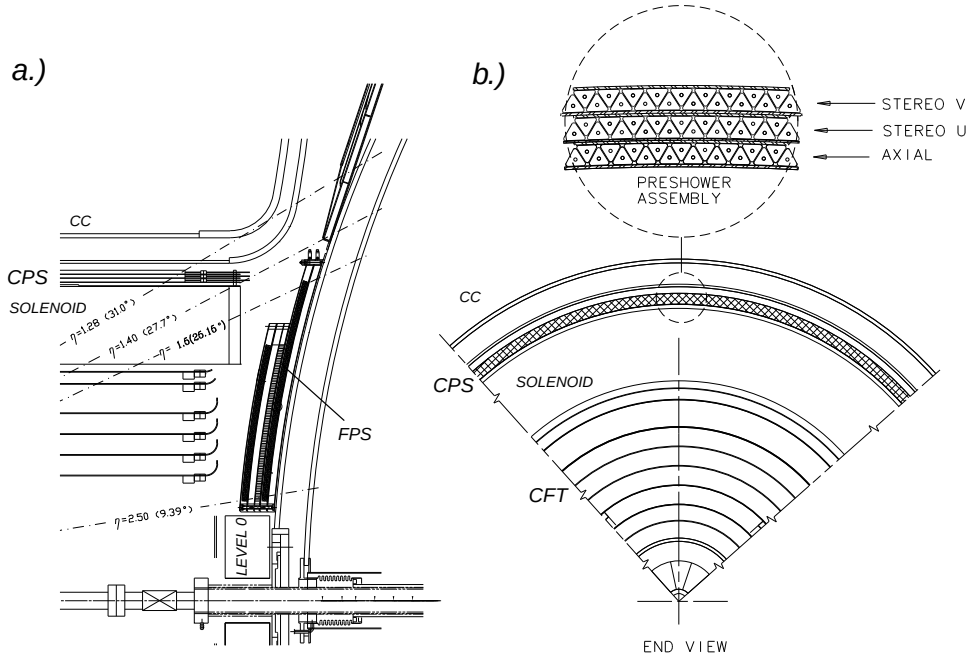

Figure 3.23. a) A $r-z$ semi-quarter view of the CPS detector. b) A cross-sectional $r-\phi$ end view of the CFT and CPS detectors. Adapted from [28].

The Forward Preshower Detector

The Forward Preshower Detectors (FPS) are mounted on the two inner faces of the end calorimeter cryostats. The detector consists of a two radiation length thick lead absorber sandwiched between two scintillation planes. Each plane is composed of one u and one v sublayer, see Figure 3.24. The outer scintillator plane covers a region of $1.4 < |\eta| < 2.5$. The same triangular strips as those in the CPS are used in these active scintillation layers. As with the CPS, clear fibers are routed about the circumference of the FPS for transmitting scintillation light from the detector to the platform below the detector, where the VLPCs are housed. The FPS has a

total of 16,000 readout channels, using the same VLPC system as used for the CFT and CPS [37, 28].

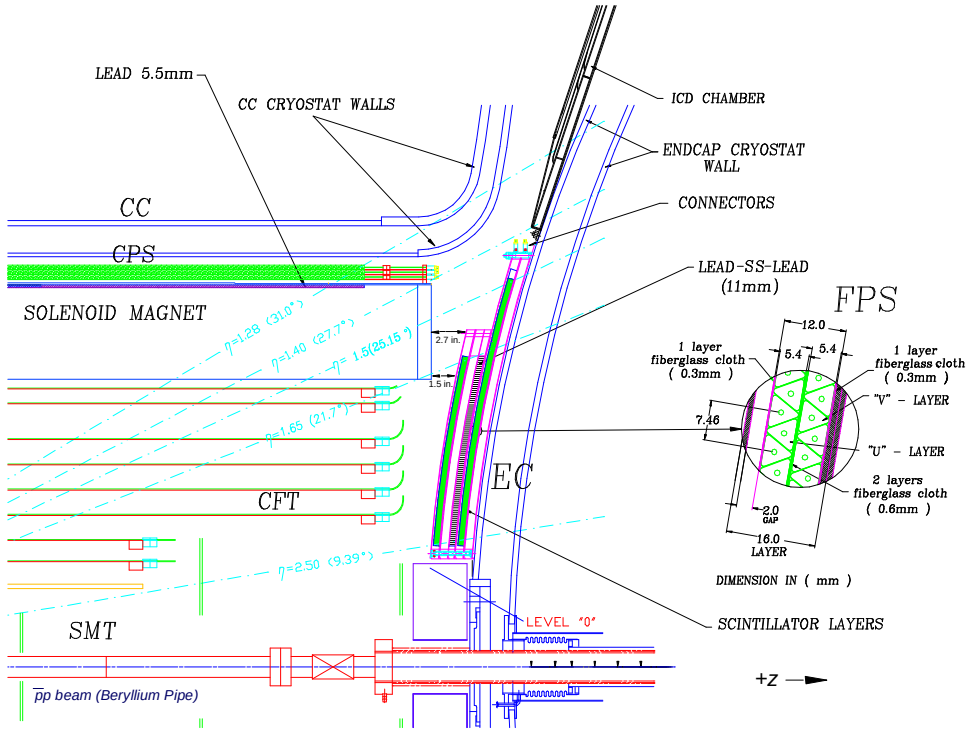

Figure 3.24. A quarter $r - z$ view of the FPS detector. Adapted from [28].

3.2.5 The Calorimeter

The Calorimeter is the most important and fundamental component of the DØ detector. It plays a vital role in the detection of key signatures from $p\bar{p}$ interactions. This calorimeter makes it possible to measure with high resolution energies and direction of electromagnetic (electrons, photons) and hadronic objects (pions, jets) over a broad range in η. While the energies of these objects are measured by determining the ionization produced by these objects, the identification of electro-

magnetic (EM) and hadronic (HD) objects are realized by means of distinguishing the types of showers that these objects create in the calorimeter.

EM objects (electrons and photons) interact primarily with the uranium in the detector via the following complementary processes: pair production ($\gamma \rightarrow e^+e^-$) and bremsstrahlung ($e \rightarrow e\gamma$). The number of secondary particles (particle multiplicity) increases but the average energy per particle decreases for each successive interaction. These are known as electromagnetic showers.

For hadron objects, the interaction with the detector occurs with the uranium nuclei through inelastic collisions via the strong nuclear force. These interactions produce secondary particles, of which about a third are neutral pions (π^0). The π^0s produce electrons and photons which interact electromagnetically, but other secondaries interact strongly. This type of particle shower is known as hadronic shower [35].

Hadronic showers as described above, generally contain electromagnetic shower components. Their parameters, however, is determined by a large variety of specifically hadronic phenomena. A hadronic shower is larger (than electromagnetic shower) and tends to develop more slowly over long distances. This is reflected in the design of the calorimeter.

The DØ calorimeter is designed as a compensating sampling calorimeter, using liquid argon (LAr) as a sampling medium and depleted uranium as well as copper and steel as absorbers [26, 27]. In order to accommodate access to the Central Detector, it is required that the calorimeter is contained in three vessels or cryostats, where the argon is kept at a temperature of 78K. The calorimeter has three modules: the Central Calorimeter (CC) covering a region of $|\eta| \leq 1.2$, the North Endcap Calorimeter (North EC) and the South Endcap Calorimeter (South EC) extending the coverage to $|\eta| \approx 4.5$, see Figure 3.25. The boundary between CC and EC is

chosen to be more or less perpendicular to beam direction to reduce degradation in the measurement of missing transverse energy [27].

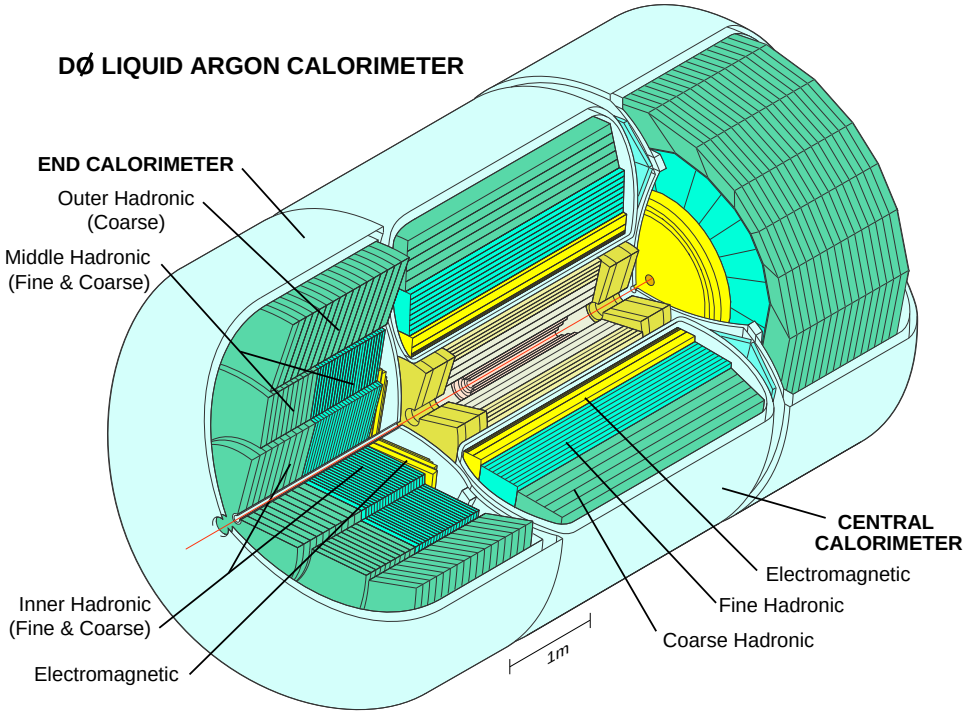

Figure 3.25. The DØ calorimeter. Adapted from [28].

The calorimeter is highly modular and finely segmented in the transverse and longitudinal direction. In the CC and ECs, there are three sections: the electromagnetic section (EM), the fine hadronic section (FH), and the coarse hadronic section (CH). The EM sections, closest to the interaction point, consist of four relatively thin and closely spacing separate layers EM1, EM2, EM3, and EM4. These EM subsections are radial layers for the CC, and for the ECs they are layered in increasing z. In CC (EC), each layer uses 3 mm (4 mm) thick nearly pure depleted uranium plates as an absorber. The FH modules each have three or four layers with 6 mm thick uranium-niobium (2 percent) alloy absorber plates. The outer CH modules

consist of only one layer of relatively thick (46.5 mm) plates made of either copper for the CC or stainless steel for the EC. Details of the depth of each layer for the three calorimeter layers in units of radiation lengths (X_0) and absorption length (λ) are shown in Table 3.3 [27].

Table 3.3

DEPTHS OF THE CALORIMETER LAYERS. ADAPTED FROM [27].

	EM	FH	CH
CC Depth	2, 2, 7, 10 X_0	1.3, 1.0, 0.9 λ	3.2 λ
EC Depth	0.3, 2.6, 7.9, 9.3 X_0	1.2, 1.2, 1.2 λ	3.6 λ

From the readout point of view, each layer is considered a discrete set of readout cells. The transverse sizes of a cell are $\Delta\eta = 0.1$ and $\Delta\phi = 2\pi/64 \approx 0.1$, typically. The EM3 layer, however, is twice as finely implemented in both η and ϕ to determine more precisely location of the EM shower centroid. A series of cells, one cell from each layer, aligned in the outward direction (direction of a shower) constitutes a tower, see Figure 3.26.

Each readout cell is a combination of several adjacent unit cells. A schematic view of a typical calorimeter unit cell is shown in Figure 3.27. There is a gap between the adjacent absorber plates filled with liquid argon. Electron-ion pairs created via ionization of the liquid argon by charged particles from a shower are collected by electrodes in the unit cell. Metal absorbers are used as ground electrodes (cathodes) and the resistive coats on the readout board at a voltage of +2.0 to 2.5 kV, in the center of the gaps, are used as anodes [27]. In most of the modules, the readout board is a sandwich of copper pads between two 0.5 mm plates

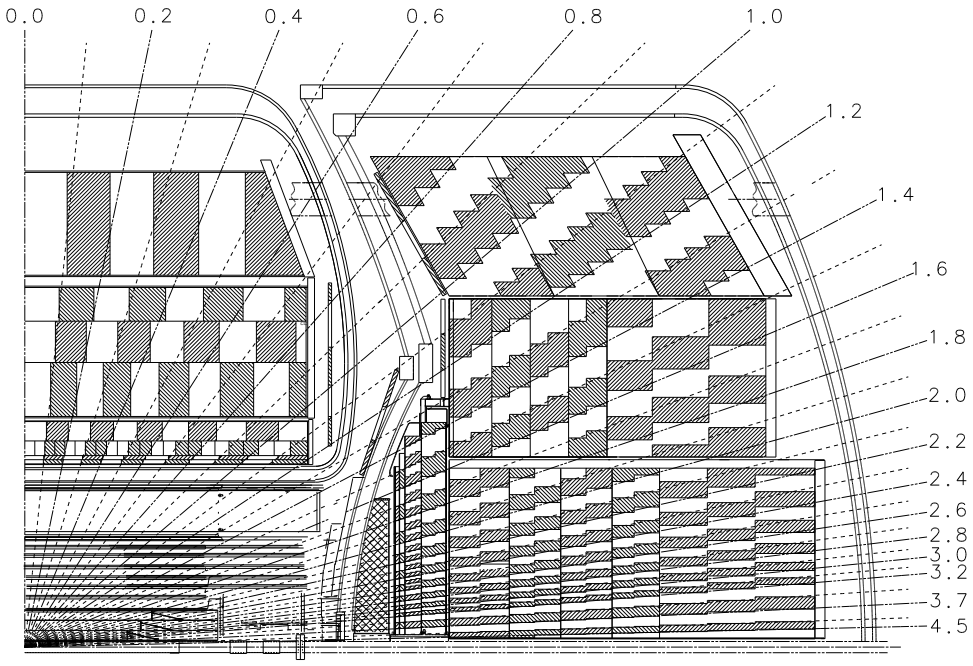

Figure 3.26. A $r - z$ view of one quarter of the DØ calorimeter. Adapted from [28].

of G10 plastic covered with the resistive epoxy coating. If a high voltage is applied to the entire resistive coat, then the charge collected by this resistive coat induces a charge on the copper readout pads via capacitiative coupling. An analog signal from the readout pad proportional to the energy deposited by the shower in the liquid argon active media is sent to the electronics, see Figure 3.28 for more details. Coaxial cables carry the signal to several electronics boards (feed-through boards). These boards reorganize the outputs from the module structure to a physics scheme where the readout channels are formed into a pseudo-projective η-ϕ tower arrangement. The signal is then sent to charge-sensitive preamplifiers and signal shaper. After the signal is shaped, it is split into two paths. One path goes to the Level 1 calorimeter trigger. Another goes to the baseline subtraction system (BLS). The BLS, as from the name, uses a previous signal taken from the previous interaction as a baseline and subtracts the baseline from the current signal. The BLS helps to

clean up the signal coming from the event to be recorded from previous collision remnants and to remove the intrinsic electronic noise from the signal before it is read out and digitized. Following a trigger decision to keep the event, the BLS output is read out and digitized by Analog-to-Digital Converters (ADC). This digitized signal is merged with signals from other detector systems to form an event [27].

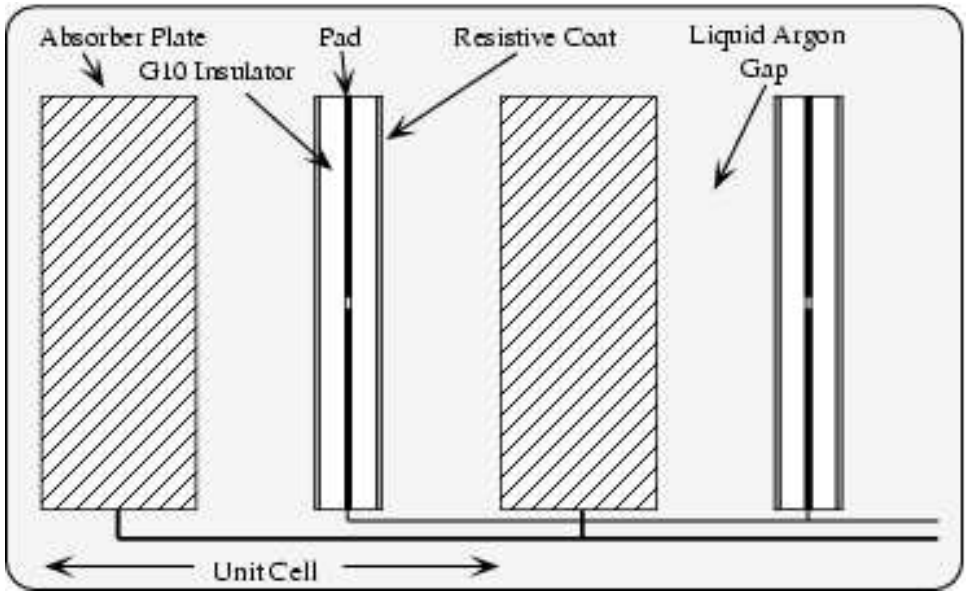

Figure 3.27. Calorimeter unit cell. Adapted from [28].

3.2.6 Intercryostat and Massless Gap Detectors

As can be seen in Figure 3.26, in the region of $1.1 < |\eta| < 1.4$ between the CC and EC of the calorimeters, there is a large amount of uninstrumented material. Cryostat walls, calorimeter support, and cabling for the detector readout constitute most of this material [27]. To help instrument this region, scintillator-fiber technology detectors have been mounted on each of the EC cryostat walls, facing the gap. Each intercryostat detector (ICD) has 384 scintillating tiles, each of size $\Delta\eta = \Delta\phi = 0.1$,

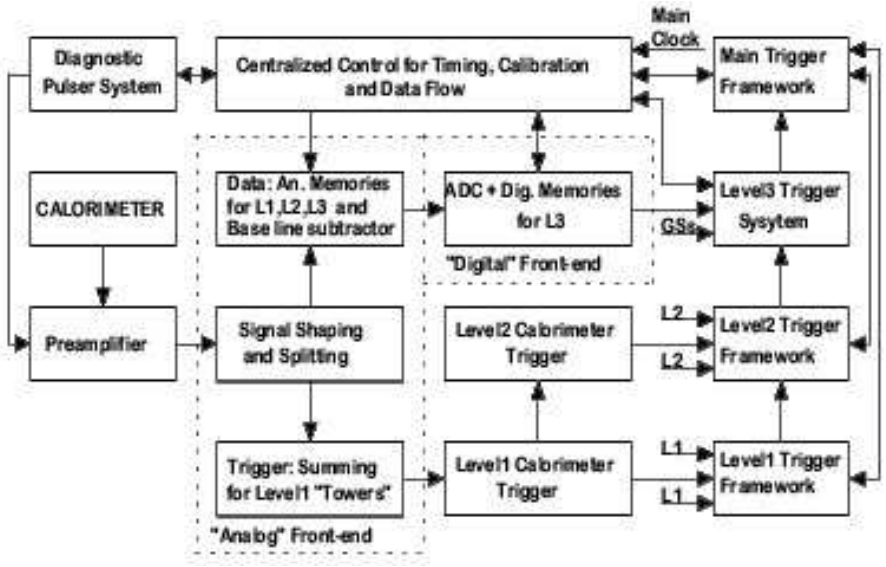

Figure 3.28. Full calorimeter data flow. Adapted from [27].

exactly matching the calorimeter cells. In addition, separate single calorimeter-like readout cell structures, called massless gaps, are installed in both the EC and CC calorimeters. Much of the readout electronics for the ICD and massless gap detectors is similar to that of the DØ calorimeters. The ICD and massless gap detectors not only provide a good approximation to the standard calorimeter readout, within this special region, but also enhance the performance of the DØ calorimeter system in some measurements such as the hadronic jet energy.

3.2.7 The Muon System

The Muon System, surrounding the DØ Calorimeter, is the outermost and physically largest sub-detector of the DØ detector system. Muons are much heavier than electrons and therefore they typically do not lose as much energy via bremsstrahlung as electrons do. Muons can penetrate a significant amount of material and have energy loss mostly due to ionization of the detector media, which is a low energy-loss, low cross section absorption process. Hence, muons with energy above a certain

energy threshold (∼3GeV) can pass through the entire DØ detector. Therefore, muon systems are designed to be the outermost sub-detectors in most high energy physics experiments. The DØ muon system, located outside the calorimeter, is well shielded from unwanted debris originating from hadronic and electromagnetic showers by the thick calorimeter material.

The DØ muon detector consists of three major components, as is shown in Figure 3.29:

- Solid-iron toroid magnet producing a 1.8 Tesla field
- Wide Angle Muon Spectrometer (WAMUS) covering a range of $|\eta| < 1$.
- Forward Angle Muon Spectrometer (FAMUS) covering a range of $1 < |\eta| < 2$ [27].

The muon system is design to perform muon identification and provide an independent measurement of muon momenta. In Run I, since there was no magnetic field in the central tracking region, the muon momentum measurement was performed using only the toroid. In Run II the muon momentum measurement is predominantly performed with the upgraded central tracking system, but the muon system toroid still can be used for an independent measurement. Momentum information from the toroid can be combined with that from the central tracking systems to further improve the overall momentum measurement for muons at DØ [21].

Toroid Magnet

The toroid magnet is a 1.09 m thick square annulus, which weighs 1973 tons [38]. The magnetic field of 1.8 Tesla is generated by a current of 1500 A. Its field lines are designed to be in a plane perpendicular to the beam axis, vertically in the side parts of the magnet and horizontally in the top and bottom.

The magnet is subdivided into a central system (covering the WAMUS region) and two forward systems (covering the FAMUS region). The magnetic field causes

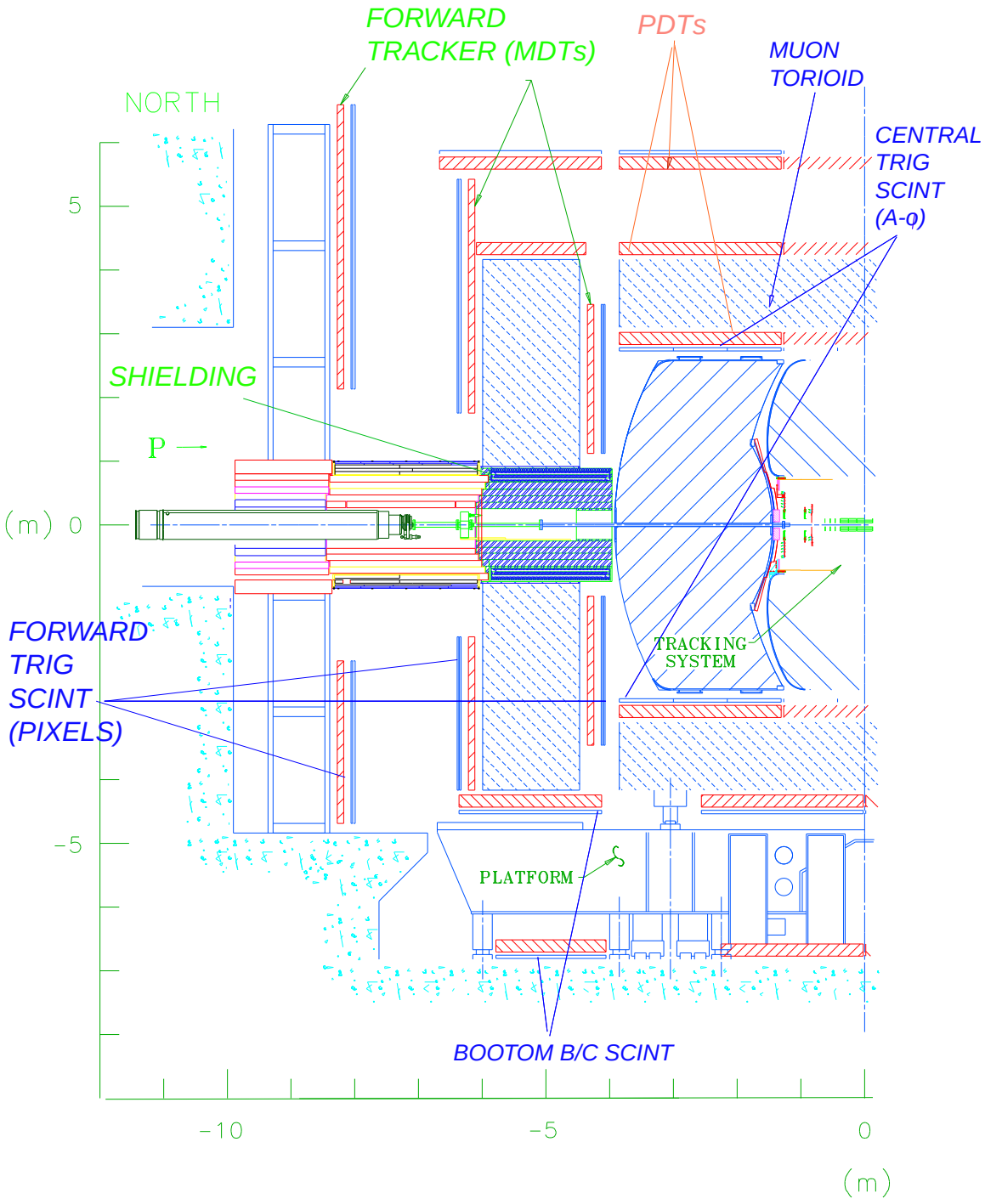

Figure 3.29. DØ Muon System. Adapted from [28].

the muon's deflections in the $r - z$ plane such that the muon's momentum can be determined by measuring how much a B- and C-layer track bends with respect to the matching A-layer track.

WAMUS

The WAMUS are separated into three detection layers, increasing radially outward and labeled as: A, B and C. The A layer is instrumented in between the calorimeter and the toroid magnet, while the B and C layers are separated from A, positioned outside the toroid. Within the WAMUS, each layer is constructed as a combination of proportional drift tube (PDT) chambers and scintillators.

Proportional Drift Tube

The PDT chambers are made from extruded aluminum tubes and are of varying size, with the largest being around 250×575 cm^2. The A layer consists of four decks of tubes with the exception of the bottom with three decks of tubes. The B-layer and C-layer each have three decks of tubes. The tubes are 10.1 cm across and 5.5 cm high. There are 24 tubes per chamber. Each tube has an anode wire in the center, oriented along the magnetic field lines, in order to provide a position measurement of the bend coordinate for momentum determination. Besides the anode wire, each tube also contains two vernier pads, at the top and the bottom of the tube, used as cathodes. The tube is filled with a non-flammable gas mixture of 80 % argon, 10 % CH_4 and 10 % CF_4. When it is in operation with voltage of 2.5 kV for the pads and 5.0 kV for the wire, the drift velocity is about 10 cm/μs, and a maximum drift time of 500 ns. The uncertainty in hit position due to diffusion in this gas is approximately 400 microns [38].

A-ϕ Counters

Scintillators for the WAMUS are categorized as the A-ϕ counters and the Cosmic Caps. The A-ϕ counters cover the PDTs in the A-layer between the calorimeter and the toroid. They are segmented in ϕ slices of 4.5 degrees with a length of around 85 cm along the beam direction. Each scintillator slice is connected to a photo-multiplier tube (PMT), used for readout, through WLSs. These scintillators with a timing resolution of $\sim$4 ns provide a fast signal used for triggering and rejecting out-of-time muons from cosmic rays and backscattered particles from the forward regions [38].

Cosmic Caps

The Cosmic Cap scintillators cover the top, sides, and part of the bottom of the muon system. They are located outside the toroid, outside the C-layer PDTs and at the bottom partly outside the B-layer. These scintillators, with a timing resolution of $\sim$5 ns, which can be improved by offline corrections to 2.5 ns, provide a fast signal to identify cosmic ray muons. The signal, together with that from the A-ϕ counters, give a time stamp on a muon to determine with which beam crossing the muon is associated [38].

FAMUS

The FAMUS consists of three layers, again called A, B and C as in the WAMUS, but instead of PDTs, Iarocci mini-drift tube (MDT) chambers are used. Scintillators for the FAMUS are pixel counters. The shielding around the beam pipe in the forward region ($2.5 < |\eta| < 3.6$) behind the EC cryostat wall is also considered a as major part of the FAMUS system. Containing a series of 50 cm thick iron and 15 cm thick polyethylene shielding with 5 cm thick lead skins, the shielding is to reduce aging of

the detectors and backgrounds from interactions of the beam with the quadrupole magnets and beam pipe by a factor of two to four [21].

Mini-Drift Tube

The MDT sections are made up of four drift planes for the A-layer and of three drift planes for the B-layer and C-layer. Each plane is divided into octants. Each plane consists of tubes, each having eight cells, see Figure 3.30. The individual cells provide an internal cross-sectional area of 9.4×9.4 mm^2 and contain a 50 μm tungsten-gold wire as the anode. The gas mixture in the cell consists of 90 % CF_4 and 10 % CH_4. This mixture under an operational cathode voltage of 3.1 kV, gives a maximum drift time of near 60 ns, which is well within the 396 ns beam crossing time. With this configuration, a position resolution in the drift plane of approximately 0.7 mm is achieved [38].

Pixel Counter

Single planes of scintillator, called the pixel counters are mounted on the face of each of the MDT tubes. Each plane is divided into eight octants with each octant consisting of slabs of scintillating material [38]. The pixel counter ϕ segmentation is 4.5 degrees, the η segmentation is 0.12 for the outer nine rows and 0.07 for the inner three rows, see Figure 3.31. The FAMUS pixel counters are read out with a WLS and PMT system with operating voltage of 1.8 kV. For a threshold of 10 mV, the efficiency for detecting a particle is 99.9 % with a time resolution of less than 1 ns.

3.2.8 Trigger and Data Acquisition Systems

Collisions happen at a very high rate at DØ, but roughly a few in a million are of physics interest. In this category are events in which a W or Z boson or even

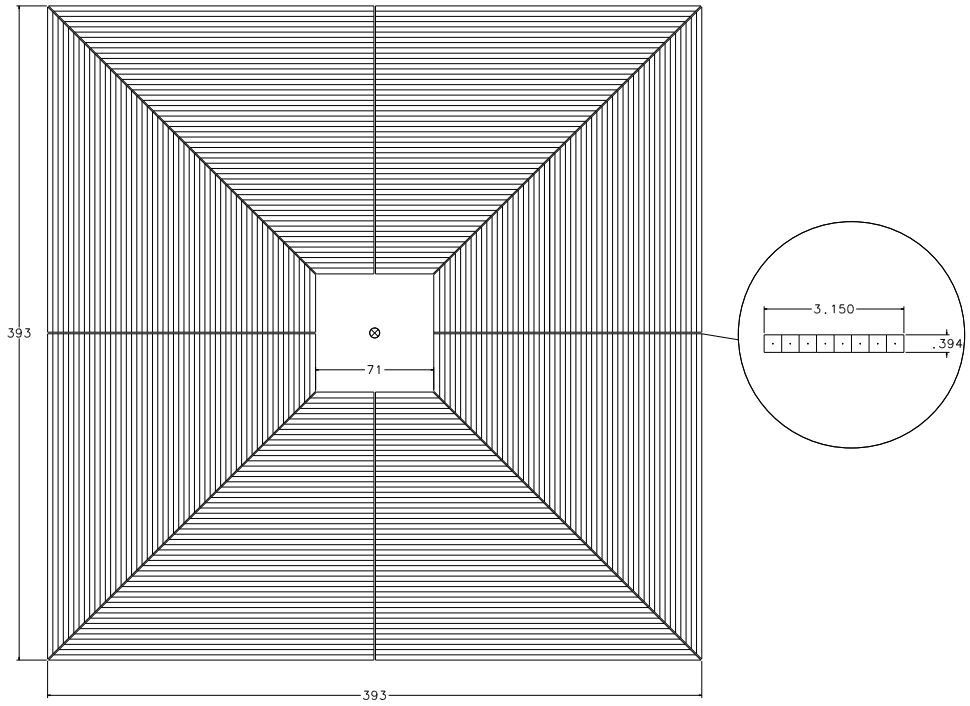

Figure 3.30. A $r - \phi$ view of one plane of the muon mini-drift tube. Adapted from [28].

a top quark are produced. Even a smaller fraction of these events is expected in searches for Higgs and other new phenomena. The majority of events coming from a $p\overline{p}$ collision at the Tevatron are due to low-p_T non-diffractive $p\overline{p}$ scattering and parton scattering. These processes have been thoroughly studied in the past, and therefore they are of little interest at DØ [27]. Apart from this, the beam crossing frequency at the center of the DØ detector is 4.7 MHz and the average event size is 250 kB. This is much too high a bandwidth to write to tape. It is necessary to design a system to filter out interesting events, with a proper balance between different physics processes based on the research priorities, and discard the rest. The DØ trigger system is a combination of hardware and software selecting the relatively few interesting collisions from a very high-rate background. A trigger looks at coarse detector information and quickly decides whether to keep or reject

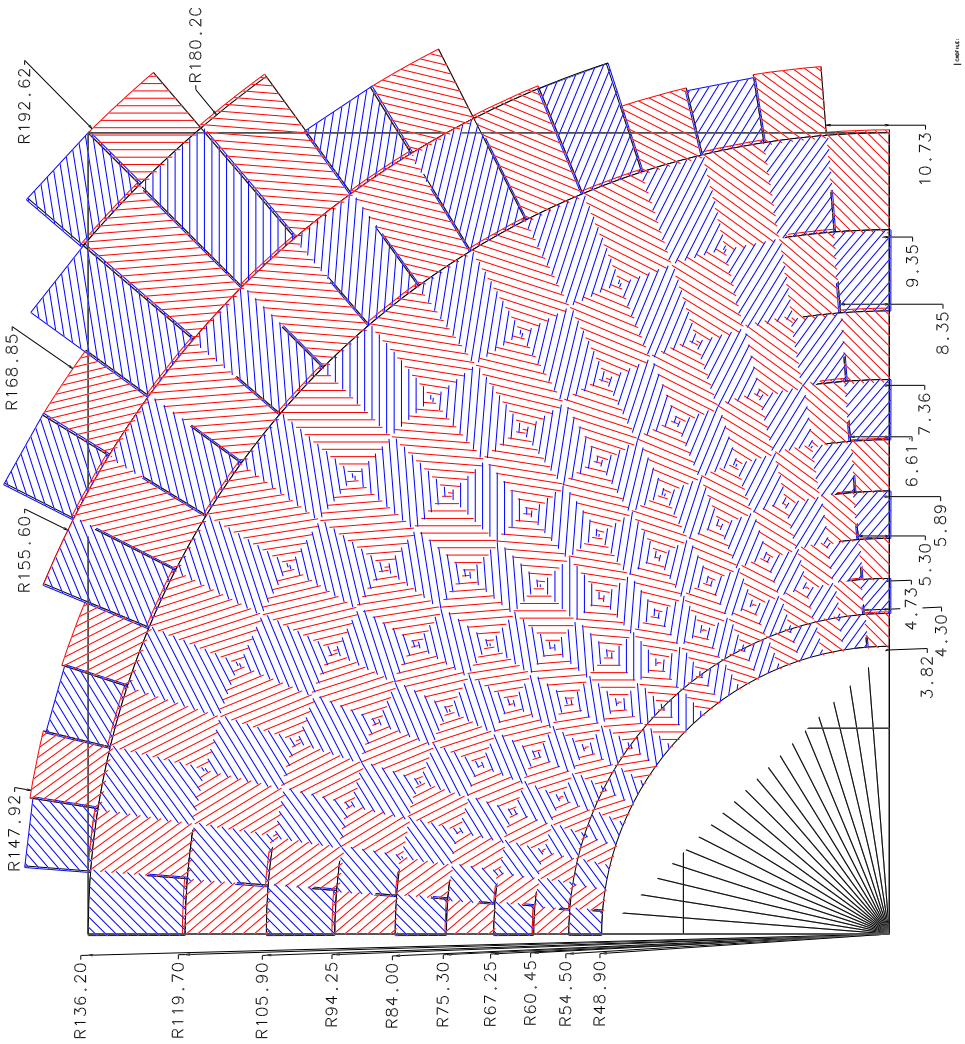

Figure 3.31. A $r - \phi$ view of the segmentation of the FAMUS scintillator pixel counters Adapted from [28].

the event, according to a specified pattern corresponding to a particular type of event. The information is typically based on the characteristics of some well known physics process. A trigger also has to be designed to be flexible enough to recognize and accept events that may contain new physics.

At DØ the trigger consists of four main decision levels: three hardware triggers (L0, L1, and L2) and a software trigger (L3). With each progressive trigger level, event selection is performed with an increasing sophistication and at a corresponding decreased output rate, see Figure 3.32.

The L0 trigger indicates the presence of an non-diffractive inelastic collision with high efficiency and provides fast determination of the Z-coordinate of the event vertex to pass to the next level of trigger.

The L1 trigger system is a flexible and programmable hardware system based on simple algorithms implemented in Field Programmable Gate Arrays (FPGAs). It collects raw information from the various detector systems in parallel, see Figure 3.33, and make a very fast trigger decision after combining and comparing them with 128 criteria (triggers). The upgraded Level 1 trigger system includes the scintillating fiber tracker, the central/forward preshower, the calorimeter, and the muon detectors.

There are two distinct stages in the L2 trigger: the preprocessor stage and the global processor stage. An L2 Framework is used to coordinate the operation of L2 and send a decision to the L3 trigger system. The hardware consists of 500 MHz Alpha processors residing in VME crates on a VME bus, running Linux and using custom built Magic Bus interfaces for 320Mb/s data handling [27]. In the preprocessor stage, each detector system builds a list of trigger information. The L2 trigger at its global stage correlates the information from the different sub-detectors and creates physics object candidates found in the event.

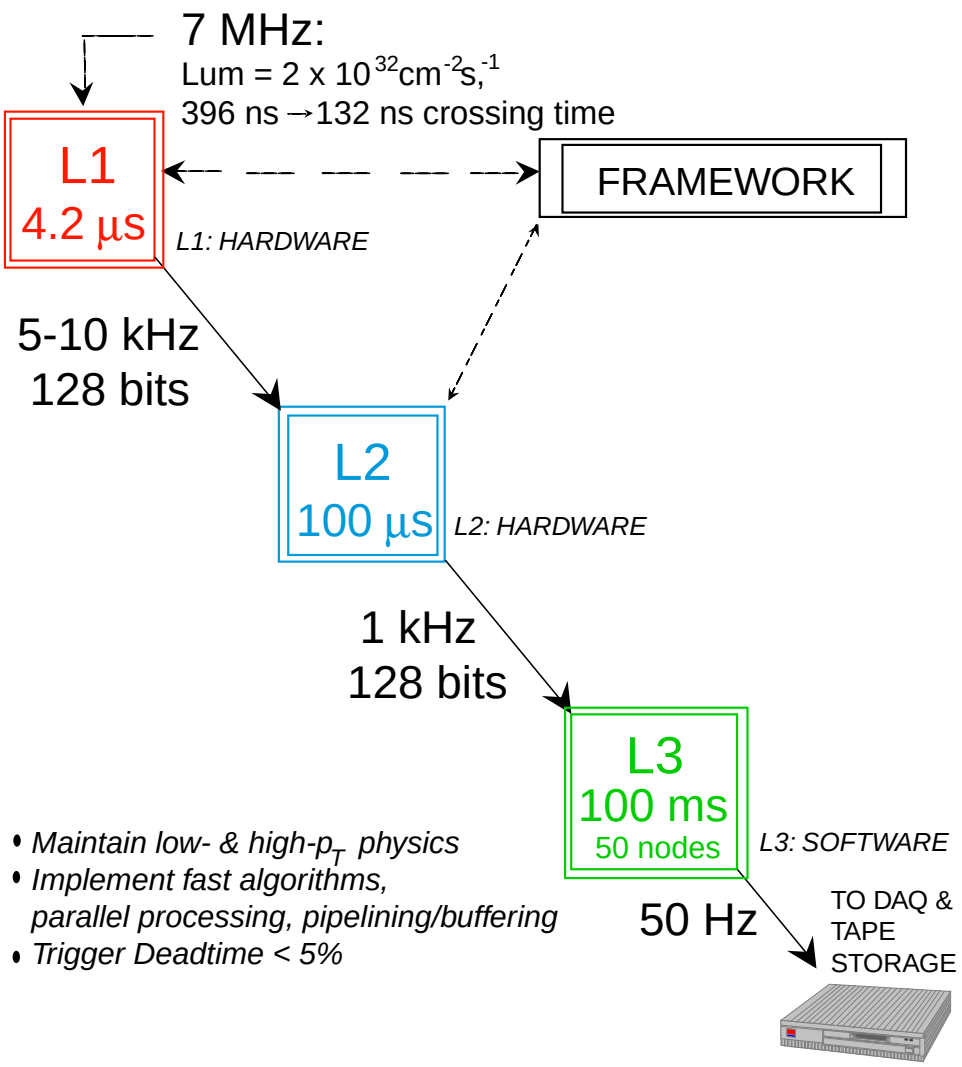

Figure 3.32. The DØ trigger layout and typical trigger rates. Adapted from [28].

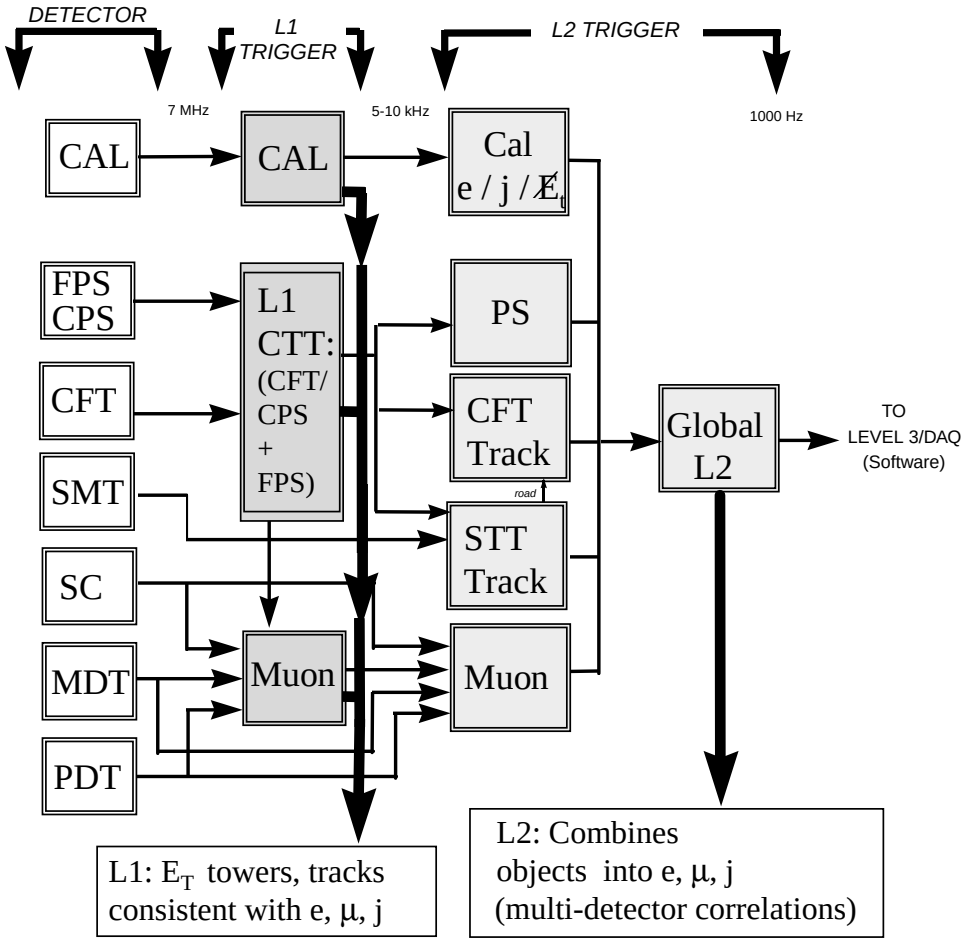

Figure 3.33. Level 1 and Level 2 trigger data flow paths. Adapted from [28].

The L3 system works as the Data Acquisition System (DAQ) as well as the L3 software trigger. When the L2 trigger system issues an accept, L3 initializes full detector readout and collects information from about 70 sub-detector readout crates (ROCs). The L3 system is characterized by parallel data paths which transfer data from detector front-end crates to a farm of Linux PC's. It combines and partially reconstructs full data for each event [27]. Figure 3.34 shows a schematic diagram of the L3/DAQ system.

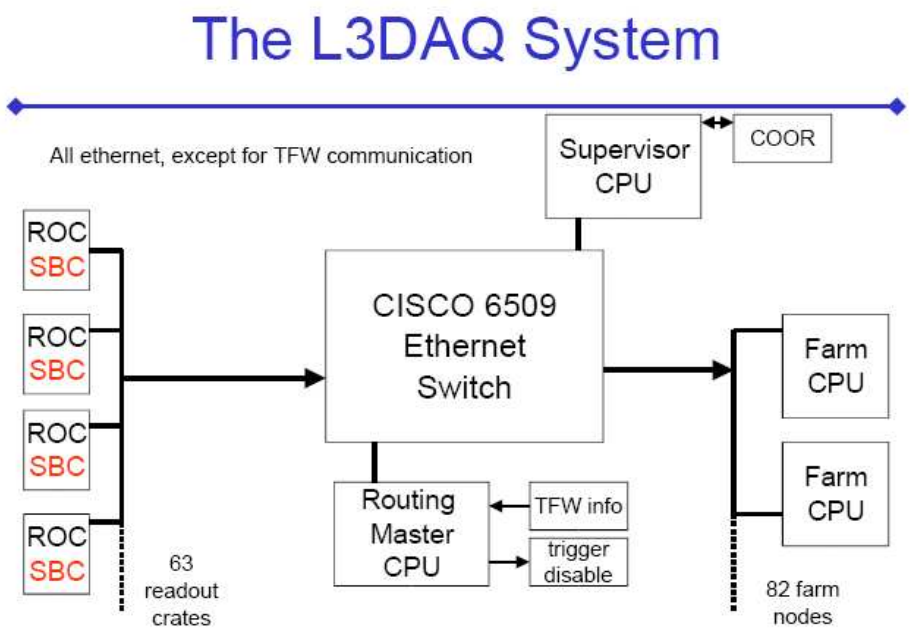

Figure 3.34. The L3 and DAQ system layout. Adapted from [27].

As can be seen from the figure, the ROCs are a set of 70 VME crates, each of which corresponds to a section of a sub-detector or the trigger framework. A data block (per event) is created from each front end crate, is moved independently through the data system and is recombined into single event at an L3 processor node. The data is read out by Single Board Computer (SBC) placed in each VME

crate. The SBC, powered by 933 Pentium-III processors with 128 MB of RAM, then send the data, 1-10 kB in size over Ethernet to one of the L3 processor farm nodes (currently 48 nodes). The L3 processors, each have an independent copy of the L3 filtering software, perform event filtering and event building. Event filtering utilizes a series of software filter tools, each tool having a specific function related to the identification of a type of physics object or event characteristic [35]. Tools, which are associated in particular combinations, exist for tracks, EM objects, muons, jets, scalar E_T, $\not\!\!E_T$, as well as other physics objects or interesting event topologies. If an event (with total size now about 250 kB) passes, it is sent via the network to a collector machine to be logged and recorded on storage media at a rate of 50 Hz for offline analysis.

CHAPTER 4

COMPOSITENESS ANALYSIS

In $p\bar{p}$ collisions at DØ at the Tevatron, quark-lepton compositeness can be studied through events containing a dilepton pair. In Run I, DØ pioneered the search for compositeness through the dielectron channel. However, because of limitation of the apparatus, it could not exploit the other lepton channels such as the opposite and same charge dimuon channels. In Run II, those channels become feasible with the upgraded DØ detector.

In this chapter the details of the search for quark-lepton compositeness in the dimuon channel at DØ using approximately 400 pb^{-1} collected in Run II are presented. The Monte Carlo (MC) simulation of a compositeness signal and the dominant Drell-Yan (DY) background is described. An overview of collider runs used in this analysis and details of the imposed selection cuts are given. No evidence for quark-lepton compositeness is found. Limits on the characteristic energy scale of compositeness for different quark and lepton chiralities are set, which represents to date the best limits for the given search channels.

4.1 Monte Carlo Studies

Dimuon events are generated using the parton-level leading order (LO) Monte Carlo generator of Reference [39] and another LO MC generator used in [40, 41]. The former MC includes the Standard Model (SM) DY contributions, Kaluza-Klein gravi-

ton exchange contributions and their interference in dimuon production [39]. The latter MC also includes SM DY contributions, but the contact interaction in different helicity channels, and their interference. They are merged into a single process, keeping all but irrelevant parts. Some parts seem redundant (e.g. two subroutines to calculate SM DY contribution or two momentum resolution functions); however, they are used for consistency checks. This has no obvious effect on speed of the MC. Instead of simulating the actual response of the muons in the DØ detector and performing the event reconstruction, the muon detection is parametrized in terms of muon energy and momentum resolutions. This parametrization includes the effect of detector acceptance, detection efficiencies, initial state radiation and the effect of different parton distributions. The leading order parton distribution functions CTEQ5L are used for the nominal prediction. The Z data are used to tune the parameters of the detector model [42]. The geometric acceptances for muons in the MC are adapted from [43] as a look-up table for the fast MC. The parametrization for the transverse momentum of the dimuon system is tuned to data. The parametrization, based on the DØ Run II data sample of Z$\rightarrow$ e^+e^-, is adapted from [42]. It is expected to yield better results at higher p_T than would be achieved with the tracking system in modeling the true dimuon p_T. The template function used in the parametrization is:

$$F(p_T) = (1.327 * 10^{-7} + 426.9p_T - 28.19p_T^2 + 0.7768p_T^3)e^{-0.1711p_T} \tag{4.1}$$

The fast MC uses this function for the generator level cross section simulation.

In order to be consistent with others in the collaboration, momentum smearing (actually 1/p smearing) is done using a $1/p_T$ resolution function of the form:

$$\frac{\sigma(\frac{1}{p_T})}{\frac{1}{p_T}} = \sqrt{\frac{(Ap_T)^2}{L^4} + \frac{B^2}{L\sin\theta}} \tag{4.2}$$

where A accounts for the physical position resolution of the detectors and B accounts for multiple scattering. L is the normalized tracking bending arm and is determined by the following:

$$L = \begin{cases} 1.0 & \text{if } |\sin\theta| > 0.358 \\ |\tan\theta|/\tan(0.366) & \text{otherwise} \end{cases} \tag{4.3}$$

The sinθ term accounts for more material the muons must pass through at higher η. Then we set

$$\frac{1}{p_T}^{smeared} = \alpha \frac{1}{p_T}^{generated} + \beta \tag{4.4}$$

where α is chosen to be 1 (it is easier to determine the $1/\mathrm{p}_T$ counter part of α, see below). β is the value of function (4.2) convoluted with a normalized Gaussian function.

In the study [43] it is found that to best describe the data a scaling factor C is applied to the smeared p_T by the following:

$$p_T(final) \; = \; C \; \times \; p_T(smeared) \tag{4.5}$$

B and L were taken directly from [44] and A and C from [43] and are given below:

$$A \; = \; 0.00272$$

$$B \; = \; 0.0258$$

$$C \; = \; 0.985$$

Adapting the work of [43], the Gaussian form (of the random number generator) used to simulate p_T smearing in the fast MC is augmented to include more non-Gaussian tails in the high mass region. It is done by adding a flat function to the

standard Gaussian functional form used to generate random numbers in the fast MC in the domain of [-50,50]:

$$f(x) \;=\; 0.0015 \;+\; \frac{1}{\sqrt{2\pi}} e^{\frac{-x^2}{2}} \tag{4.6}$$

A 4% systematic error due to the choice of p_T smearing for both signal and background is taken into consideration and is included in the limit setting procedure.

The MC includes Standard Model DY contributions ($Z/\gamma*$), as well as the contact interaction and their interference in dimuon production. Since we use a LO generator, the effects of next-to-leading order (NLO) are modeled by adding a transverse momentum to the dimuon system based on the transverse momentum spectrum observed in the data. The transverse part of the NLO processes is taken into account by applying a random p_T-kick to the system, based on the p_T spectrum of dielectron events observed in the data. The scattering angle θ^* is defined in the dimuon helicity frame, i.e. relative to the direction of the boost of the dimuon system, see Figure 4.1. The number of events is corrected for higher orders using a constant K-factor (defined earlier as ratio of NLO to LO cross section) of 1.3 [19]. The same factor is used for the compositeness signal. A 10% systematic uncertainty on the value of the K-factor is assigned and included in the limit setting procedure.

4.2 Muon Identification

Different muon subdetectors reconstruct muon tracks from various hits. They convert the raw hits and time information into three dimensional position information. The group of close hits in each layer is fitted to a line to form a track segment. It is done separately for segments before and after the toroid magnet. The segments are matched to form the tracks. Momentum is determined from the bending of track while passing through the toroid magnet. This measurement, corrected by

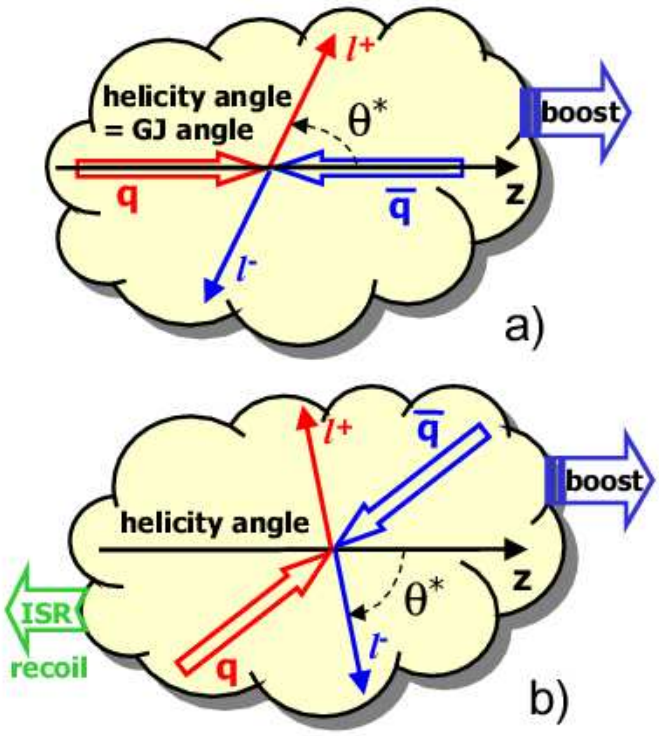

Figure 4.1. a) Definition of the angle θ^* at the parton level. b) Definition of the angle θ^* at NLO. Here GJ stands for the Gottfried-Jackson frame. ISR refers to initial state radiation. Adapted from [45].

the loss of energy in the calorimeter provides an independent measurement of the momentum in the local muon system. Later on, this can be used to improve the momentum resolution in a global fitting with the associated charge particle tracks in the central detector and the event vertex.

The grouping of hits above can be used to classify the type of reconstructed muons. A number called *nseg* is assigned depending on which muon system layer the corresponding segments came from and on whether the muon segments have been matched to tracks associated with the charge particle in the central tracker. A positive or zero *nseg* indicates that the there is a central track match and negative indicates there is no central track match. Table 4.1 shows a list of different muon

types with their corresponding values of *nseg*.

Table 4.1

THE DIFFERENT MUON TYPE.

nseg	Muon Type	Central Track Matching Algorithm
3	Central track + A and BC-layer	Muon to central if local muon track fit converge
2	Central track + BC only	central to muon
1	Central track + A only	central to muon
0	Central track + muon hit or central track + MTC	central to muon or central to calorimeter
-1	A segment only	no match
-2	BC segment only	no match
-3	A + BC segment	no match

Here MTC stands for "Muon Tracking in the Calorimeter".

Another parameter used to classify muons is the *quality*. The muon quality can be *tight*, *medium* and *loose*. The definitions of different muon qualities are given in Table 4.2.

4.3 Data Set and Event Selection

This analysis extends the search for quark-lepton compositeness through the dimuon final state. It is based on all data collected with the DØ detector in Tevatron Run II, corresponded to a run range from 151810 to 196586 (viz Figure 4.2). These runs were recorded from August 2002 until August 2004. It has been reconstructed with several versions of the DØ reconstruction (d0reco) program such as p13, p14.03.00, p14.03.01, p14.03.02, p14.05.00, p14.05.02, and p14.06.00. This could create a problem of inconsistency for analysis using part or all of those data. In addition, there

Table 4.2

MUON QUALITY DEFINITIONS.

	nseg=3
tight	At least two A-layer wire hits At least one A-layer scintillator hit At least three BC-layer wire hits At least one BC-layer scintillator hit A converge local fit ($\chi^2_{loc} > 0$)
medium	At least two A-layer wire hits At least one A-layer scintillator hit At least two BC-layer wire hits At least one BC-layer scintillator hit
loose	*medium* but allowing one of the criteria to fail
	nseg=2
medium	At least one BC-layer scintillator hit At least two BC-layer wire hits *If located in the bottom part of the detector, $\lvert\eta_d\rvert < 1.6$
loose	*medium* but no * requirement
	nseg=1
medium	At least one A-layer scintillator hit At least two A-layer wire hits *If located in the bottom part of the detector, $\lvert\eta_d\rvert < 1.6$
loose	*medium* but no * requirement

could be duplicate events. The former problem was solved by the DØ Common Sample Group who applied fixes to the older version of the reconstructed data for them to be compatible with data reconstructed with versions 14.05.02 and 14.06.00. Due to the high p_T signature of compositeness, only isolated high p_T dimuons are chosen (see below).

The data sample used is the DØ New Phenomena group dimuon skim [46], provided by the DØ Common Sample Group to create a loose high-p_T dimuon sample called 2Muhighpt, see [47]. The selection criteria for the skimmed data are:

- At least two muons with "loose" quality (specified by the muon identification group)
- Both must have $p_T > 15$ GeV/c (as measured from matched central tracks)

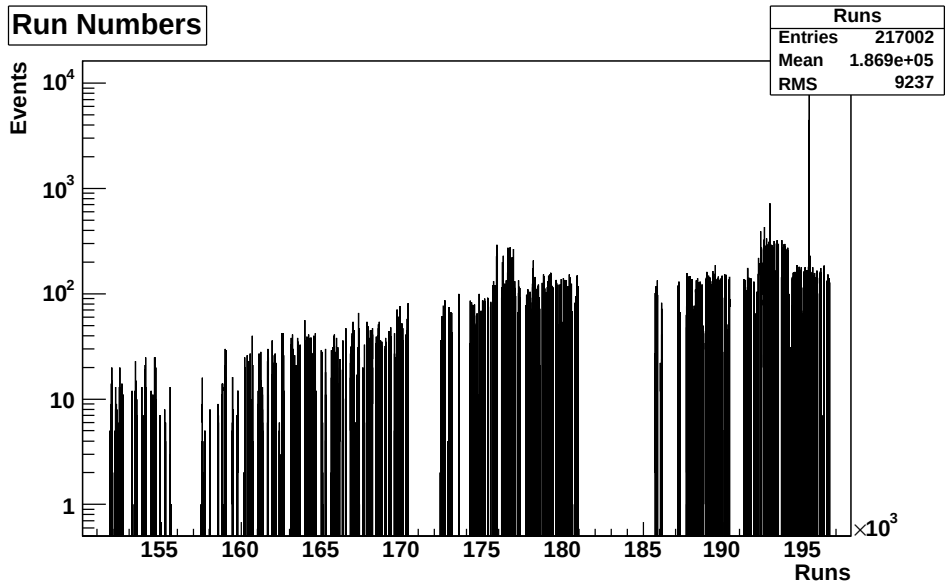

Figure 4.2. Run number for the entire data set.

The skimmed data are in the DØ compressed data format called *thumbnail*; they are then run through a package called *d0correct*, version v00-00-06a to get certified muons in $TMBTree$ format (an object-oriented container class, which can be accessed using ROOT methods [48]). Only muons with positive *nseg* values are chosen. Those $TMBTrees$ with 217002 events are then processed by a package called *d0root_analysis* for this analysis.

The quality of the data has been checked by each DØ subdetector group. The group provides a list of runs which are marked bad if there were problems with a particular subdetector. The quality of the runs then is stored in the Offline Run Quality Database.

From the Database a list of bad detector quality runs (muon, or CFT or SMT) is retrieved and used to remove those bad runs from this sample. Runs ranging from 168618 to 169295 are also excluded because of PDT readout problems in the muon system. This reduces the data sample to 171757 events.

There are a large number of duplicate events in the sample because of the use of different versions of d0reco. The duplicate events are removed keeping only the instance of events with the latest version of d0reco. The sample is reduced to 169221 events after duplicate removal.

All muons are required to lie within the geometrical acceptance of the detector, which is defined as the region of $|\eta| < 2.0$ and outside the bottom hole. The hole is defined to be the region where $|\eta| < 1.25$ and $4.25 < \phi < 5.15$ (see Figure 4.3).

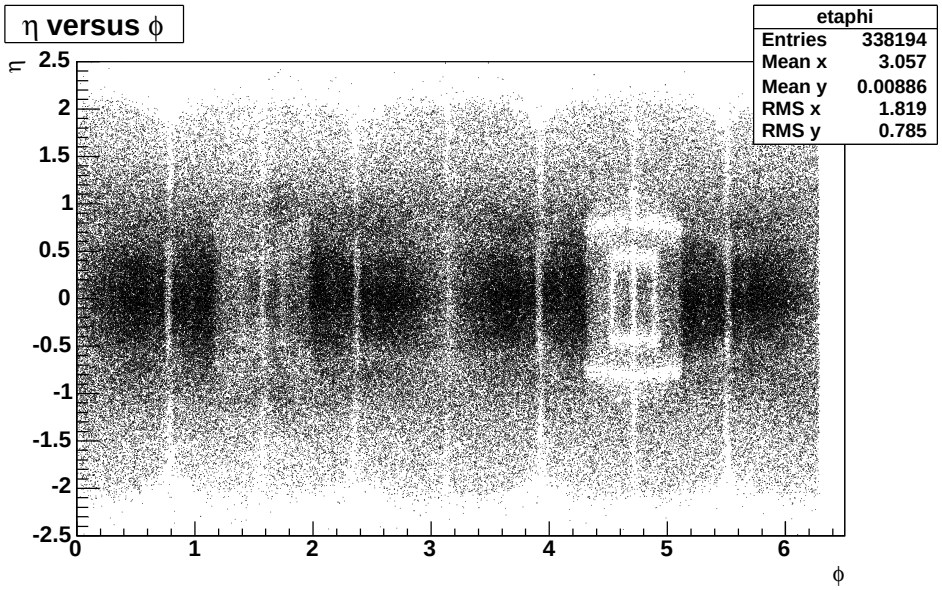

Figure 4.3. η versus ϕ of muons before acceptance cuts.

Even though only the effective luminosity is used, for a consistency check, the data are required to fire one of the following dimuon or single muon triggers:

2MU_A_L2M0, 2MU_A_L2M0.TRK10, 2MU_L2ETAPHI, 2MU_A_L2M0_L3L15, MUW_W_L2M3_TRK10 or MUW_W_L2M5_TRK10. The integrated luminosity for these triggers is 406 ± 26 pb^{-1} (about 6%, as calculated in [55]) for this sample.

4.3.1 Event Selection Cuts

Adapted from [49], in order to justify the chosen cut, the following histograms are given for each cut:

- the distribution of the cut variable;
- the distribution of the invariant mass of the dimuon pair M$\mu\mu$ for the events that fail that cut.

These plots help to highlight:

- the degree to which each cut quantity discriminates signal from background;
- the sensitivity of the selected event sample to the chosen cut values;
- the amounts of signal and background exclusively rejected by each cut;
- the level of background remaining in the selected event sample [49].

Muon momentum in this analysis was taken as the momentum from the muon's matched central track. In order to improve the momentum measurement of the muon, quality track cuts are imposed on the tracks. They are required to have at least 1 SMT hit and more than 8 CFT hits. Figure 4.4 shows the distribution of CFT and SMT hits for muon tracks and the invariant mass distribution of events rejected by the track quality selection. There are 94167 events which passed this selection. Since only events with dimuon invariant mass greater than 50 GeV are of interest, a mass cut at 50 GeV is imposed on the sample. It reduces the data sample to 63297 events.

Muons from cosmic rays can pass through the DØ detector; if they pass close enough to the interaction region and within the trigger timing gates, they can be reconstructed as dimuon events. This can represent a major background to the data

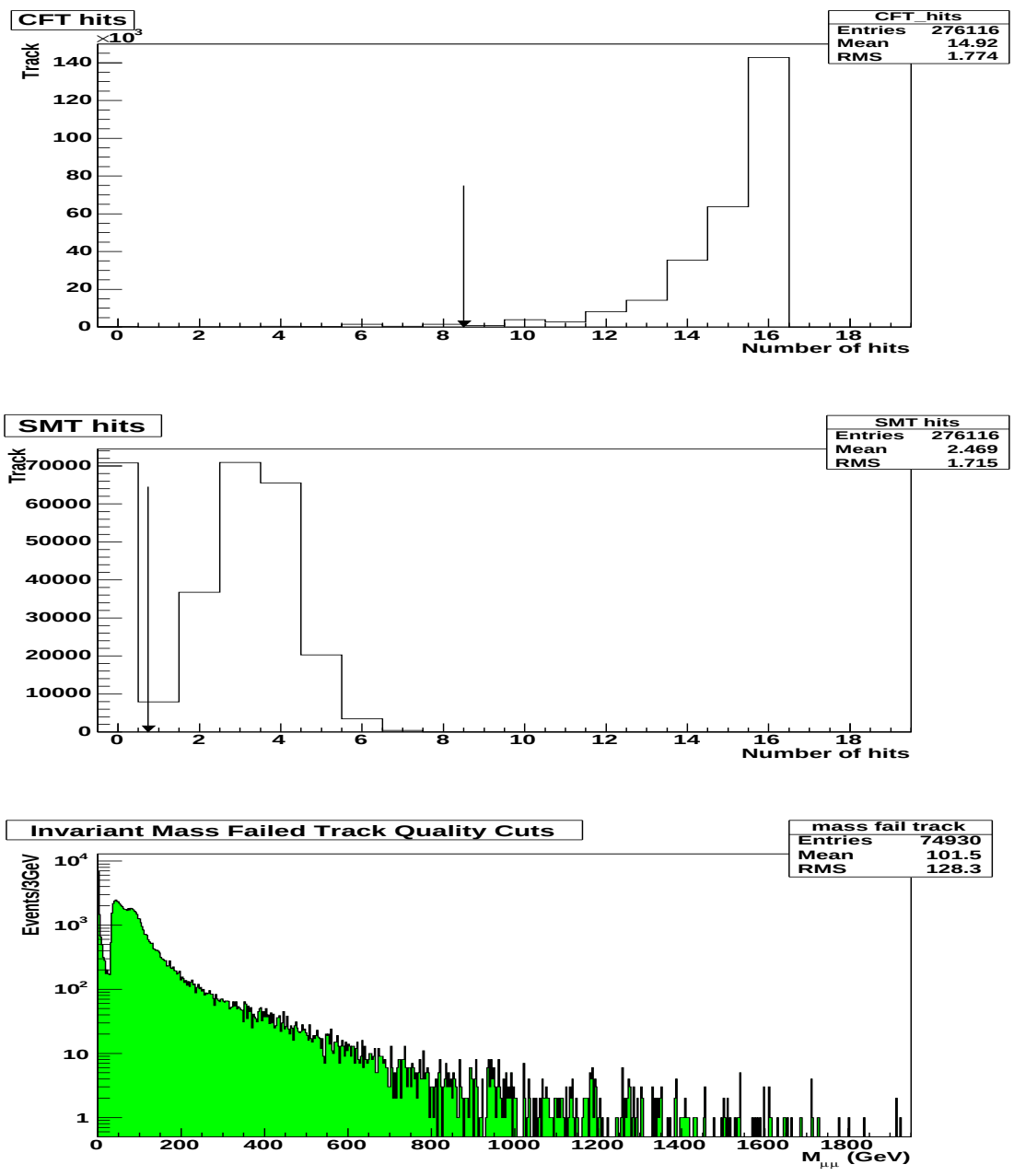

Figure 4.4. Track quality selection. The top two plots are CFT and SMT hits distributions of the muon tracks. The bottom plot shows distribution of M$\mu\mu$ for the events rejected by this track quality selection.

sample. However, the scintillation counters in the muon system can determine very precise times of the detected muons. The counters are calibrated so that muons originating from $p\bar{p}$ collision will have time t = 0. Cosmic muons have to travel a distance of 6m from the top to bottom A–layer of muon scintillators. This will take 20 ns. Therefore the DØ Muon ID group prescribed a standard cosmic timing cut of scintillator time $|t| > 10$ ns in the A or BC scintillator layer of the muon system to cut out-of-time cosmic rays muons. Figure 4.5 shows the distributions of A and BC scintillator times for the data sample and the distribution of M$\mu\mu$ for the events which failed these cuts. There are 41312 events remaining after these cuts.

The loose muon criterion is such that muon can miss one or more scintillator hits and therefore the timing information is lost. The time of such a missing hit is set to zero and the muon will be within the timing window of the standard cosmic cuts. Hence, there is still a significant number of cosmic muons present in the data sample. In order to eliminate the cosmic rays, but keep the muons of loose quality, additional cuts using the signatures of cosmic muons are imposed. Two muons that are from a cosmic ray are back–to–back. That is because the same cosmic muon is reconstructed twice, once as it enters the detector region and once as it leaves. Therefore the two muons from cosmic rays should have $\eta_1 + \eta_2 = 0$ and their acolinearity $\Delta\alpha_{\mu\mu} = |\pi - \Delta\phi_{\mu\mu}| + |\pi - \sum \theta_{\mu\mu}|$ should be close to zero. Therefore a cut on sum of η $[-0.0102 < \eta_1 + \eta_2 < 0.0175]$ [43] as well as cut on acolinearity $[\Delta\alpha_{\mu\mu} > 0.05]$ [49] are used to veto additional muons originating from cosmic rays. These tight cosmic cuts prove to be very effective in rejection of the remaining muons from cosmic rays [43, 49]. The data sample then contains 39828 events.

To minimize the background from heavy quark decays, both muons are required to be isolated in both the calorimeter and the central detector, satisfying the stan-

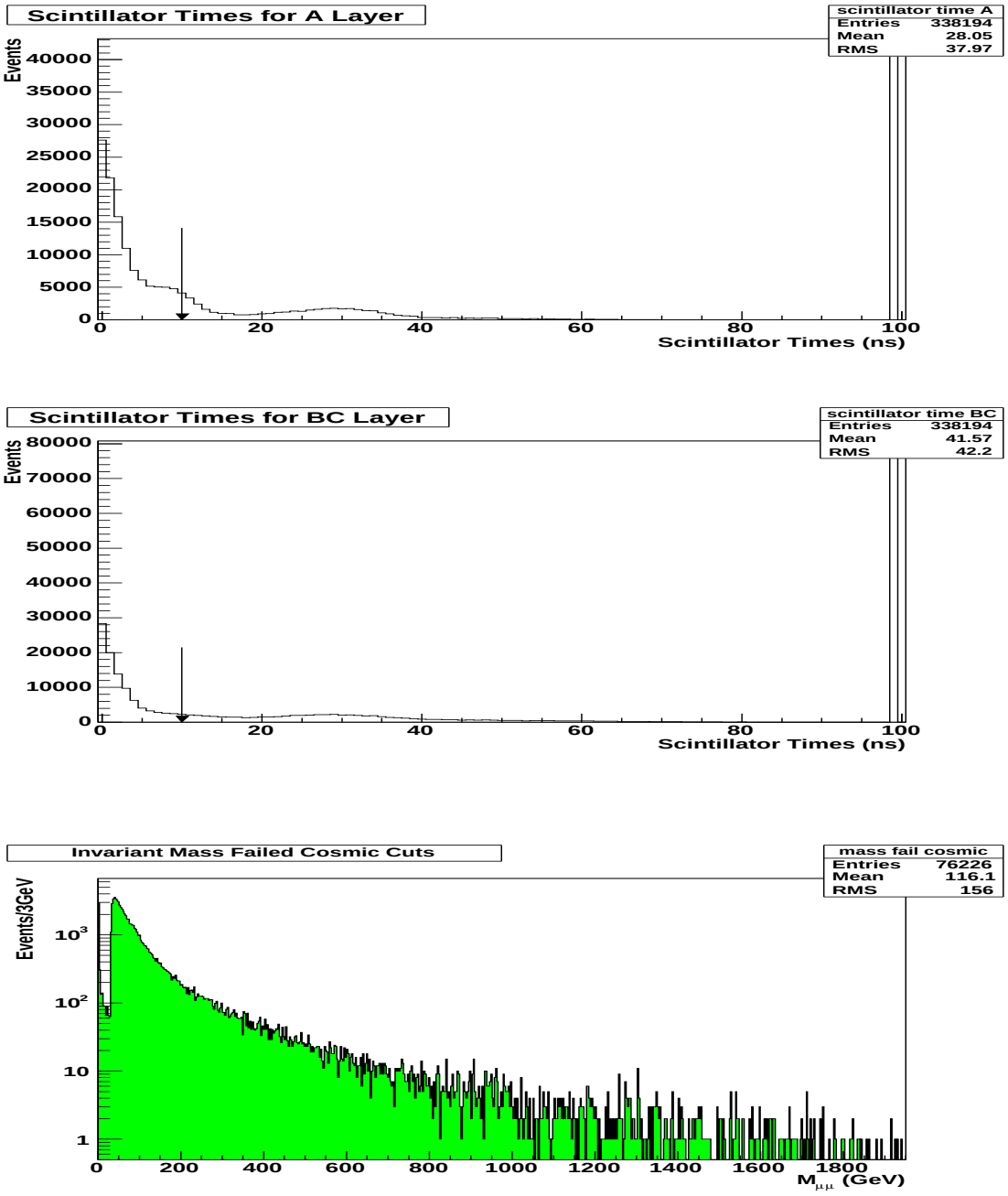

Figure 4.5. Standard cosmic cuts. The top two plots are distributions of A and BC scintillator times of the muons in the sample. The bottom plot shows distribution of M$\mu\mu$ for the events rejected by this selection. Note that with missing hits, d0root_analysis defaults times to 99 ns.

dard isolation criteria:

- $\sum_{cone0.5}(p_T) < 2.5$ GeV, where $\sum_{cone0.5}(p_T)$ is the sum of the p_T of tracks (except the muon track) contained within a cone around the muon of width $\Delta R = 0.5$. This will be referred to as the track halo.
- $\sum_{halo}(E_T) = \sum_{cone0.4}(E_T) - \sum_{cone0.1}(E_T) < 2.5$ GeV, where $\sum_{cone0.4}(E_T)$ and $\sum_{cone0.1}(E_T)$ are the sums of the E_T in calorimeter clusters within cones around the muon of widths $\Delta R = 0.4$ and $\Delta R = 0.1$, respectively. This will be referred to as the calorimeter halo.

A cone of width ΔR is defined in η and ϕ space by $\Delta R = \sqrt{\Delta\eta^2 + \Delta\phi^2}$. Figure 4.6 shows the track halo distribution and the invariant mass distribution for the events which failed this requirement. Figure 4.7 shows the similar distributions for calorimeter halo.

There are 28635 events remaining after both the isolation cuts.

Because of the limited resolution of the tracking system with very high momentum objects such as muons used in this analysis, the momenta of the two muons do not balance in p_T. One of them appears to have much higher p_T than it really has. It is physically reasonable to apply a fix to reduce that effect by balancing the measured muon transversed momenta. This helps to recover some of events with unphysical energy or momentum. Using the idea suggested in previous studies [43], the p_T of each muon track is scaled to a weighted average based on the original measured track's p_T and their errors (see Equation 4.2). The resulting momentum is closer to the momentum with smaller error (which means the smaller momentum). The fix is applied for all events after all cuts were applied. The p_T of each muon track is corrected as follows:

$$p_{T_{1'}} = p_{T_{2'}} = \frac{\sum_{n=1}^{2} w_n p_{T_n}}{\sum_{n=1}^{2} w_n} \tag{4.7}$$

where p_{T_n} are the original measured muon momentum, $w_n = 1/\sigma^2_{p_{T_n}}$, and $\sigma_{p_{T_n}}$ is calculated from Equation 4.2. The measurement of angles is expected to be accurate,

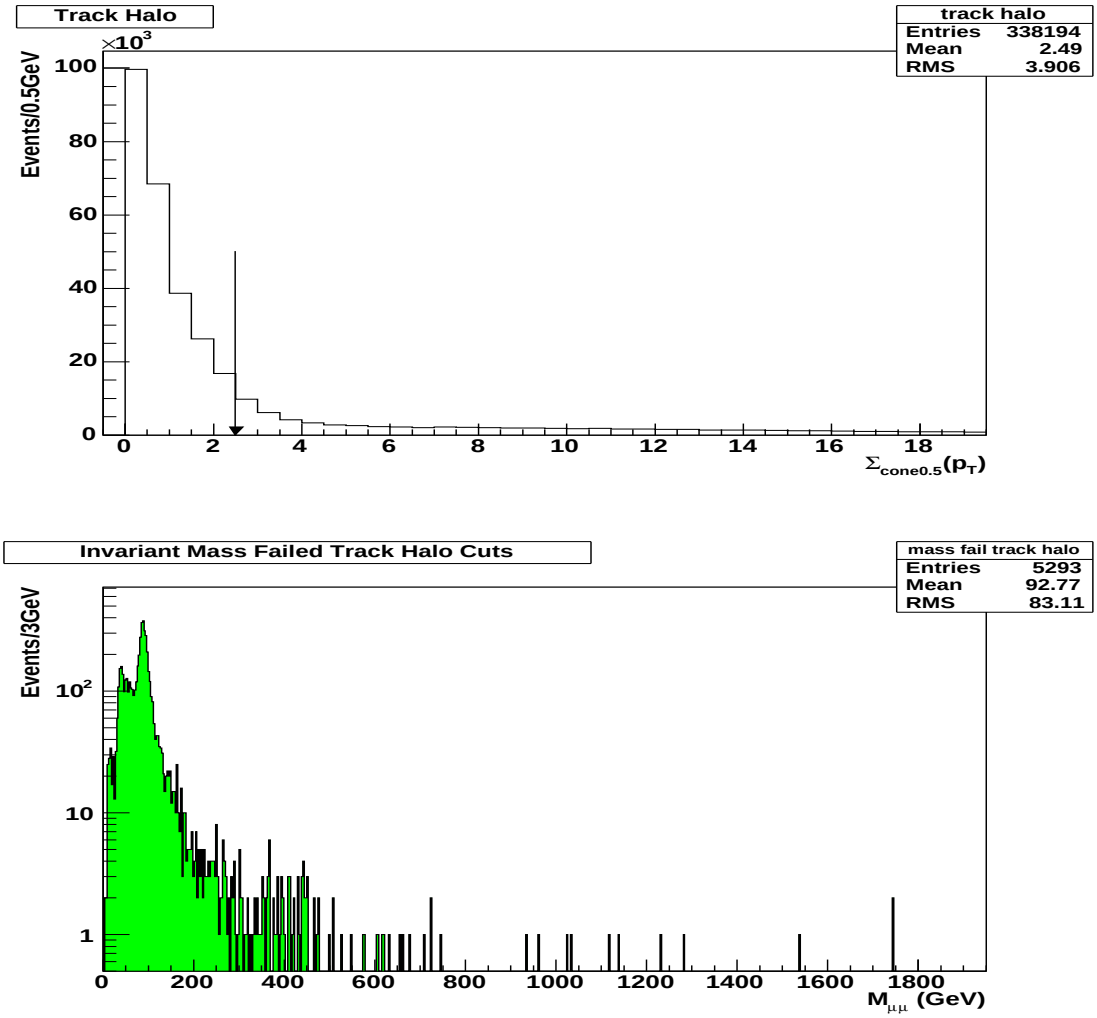

Figure 4.6. Standard isolation cuts. The top plot shows distributions of $\sum_{cone0.5}(p_T)$ of the muons in the sample. The bottom plot shows distribution of M$\mu\mu$ for the events rejected by this selection

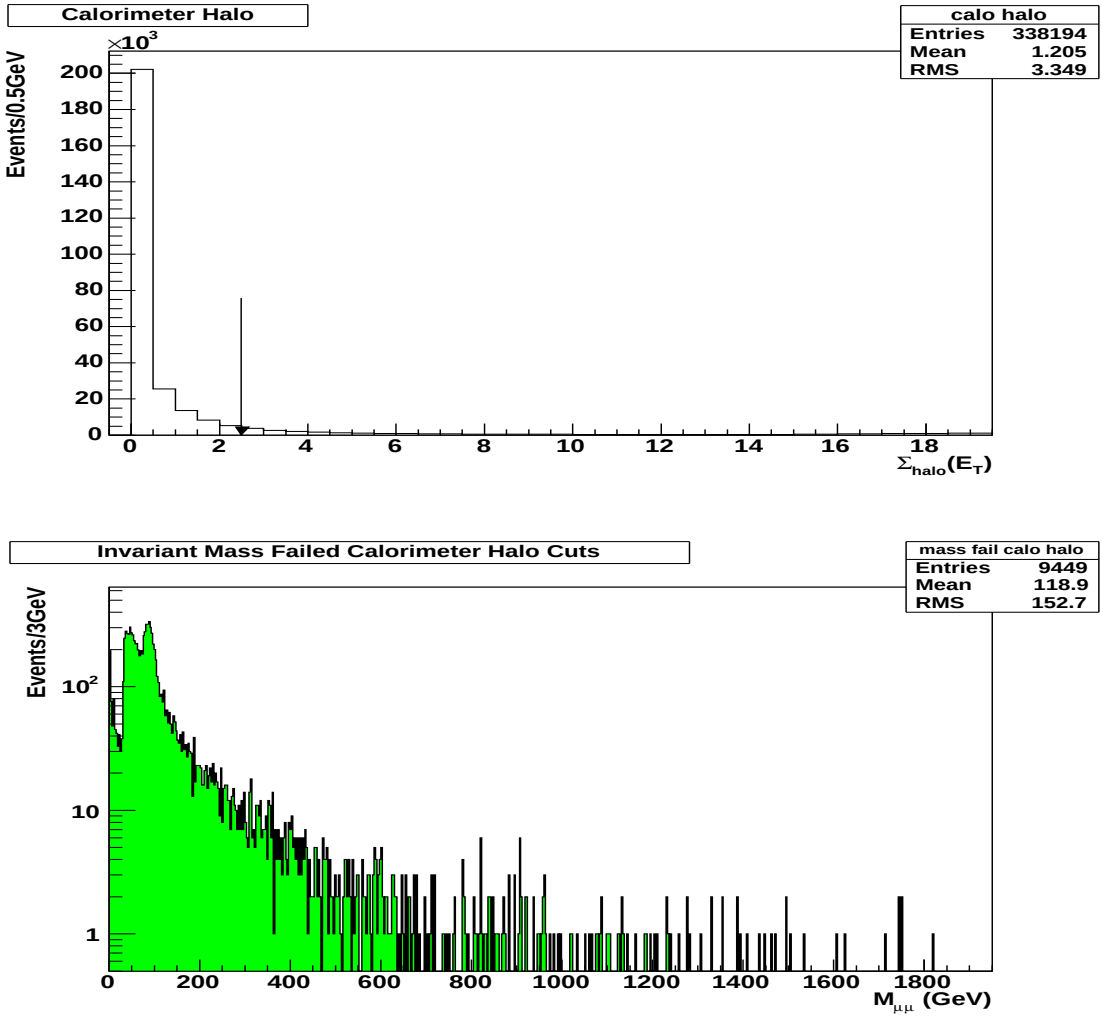

Figure 4.7. Standard isolation cuts. The top plot shows distributions of $\sum_{halo}(E_T)$ of the muons in the sample. The bottom plot shows distribution of M$\mu\mu$ for the events rejected by this selection

so after the fix, a new four momentum is calculated for each muon in the event. From this the mass and $\cos\theta^*$ are recalculated.

The $M_{\mu\mu} > 50$ GeV cut is then reapplied to get a final data set of 28017 events (details in Table 4.3). The same procedure is applied for the MC used in the previous section.

Table 4.3

DATA SELECTION.

Cut	Number of events passing
Initial TMBTree sample	217002
Bad run removal	171757
Duplicate event removal	169221
Track quality cuts	94167
$M_{\mu\mu} > 50$ GeV cut	63297
Standard cosmic cut	41312
Additional cosmic cuts	39828
Isolation cuts	28635
$M_{\mu\mu} > 50$ GeV reapplied after the p_T re-scaling	28017

4.4 Background

The main contributions to the background are dimuon events which are decay products of $\tau^+\tau^-$ or $b\bar{b}$ production. They contribute about 1.1 % of the total DY events. This result is from a study [11] of the near-Z-mass region extrapolated to the higher-mass region. They are included in the SM backgrounds from DY and Z boson production (already included) in the output of the MC used to generate the signal.

4.5 Data and MC Comparison

Figure 4.8 and Figure 4.9 show the comparisons of the dimuon invariant mass for data and for Drell-Yan MC on linear and log scales (after the p_T correction) and of $|\cos\theta^*|$. Figure 4.10 shows the M$\mu\mu$ vs. $|cos\theta^*|$ distributions for data and MC. Together with Figure 4.11, Figure 4.12, Figure 4.13, Figure 4.14, Figure 4.15, Figure 4.16, Figure 4.17, Figure 4.18, Figure 4.19, Figure 4.20, Figure 4.21, Figure 4.22, Figure 4.23, Figure 4.24, Figure 4.25, Figure 4.26, Figure 4.27, Figure 4.28, and Figure 4.29, they illustrate the dependence of signal on Λ (or the parameter β_C). Overall the data agree with the Standard Model Drell-Yan prediction.

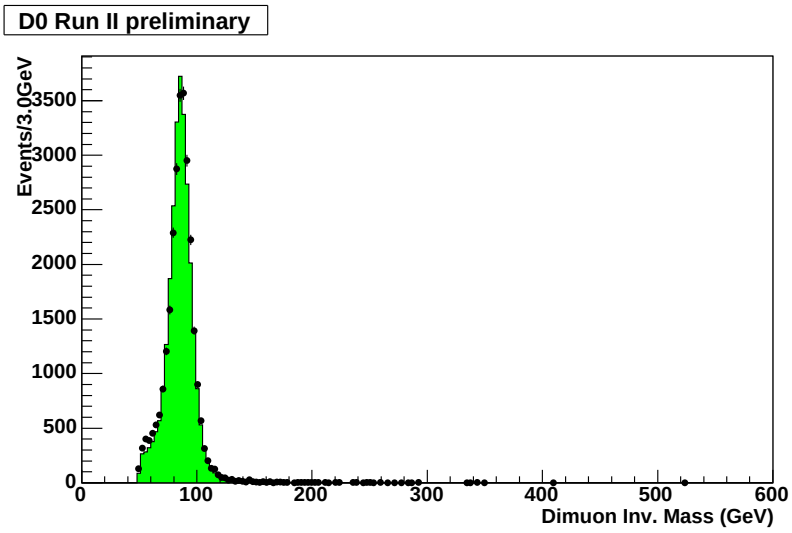

Figure 4.8. Comparison of dimuon invariant mass for the data (dots) and Drell-Yan MC (filled histogram).

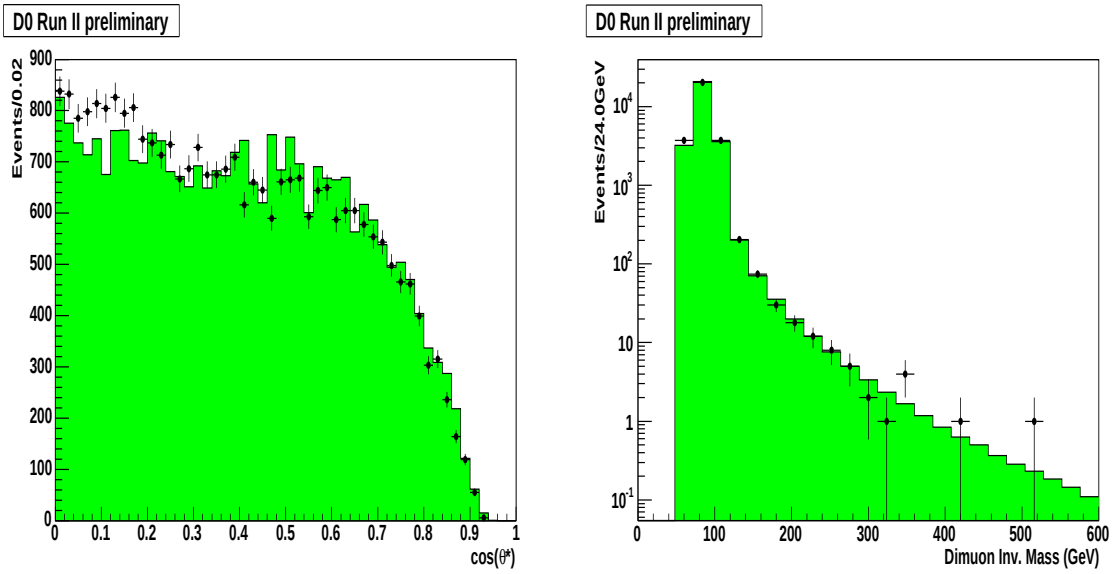

Figure 4.9. Comparison between data (points) and backgrounds (histogram) for $|\cos\theta^*|$ and $M_{\mu\mu}$ distribution.

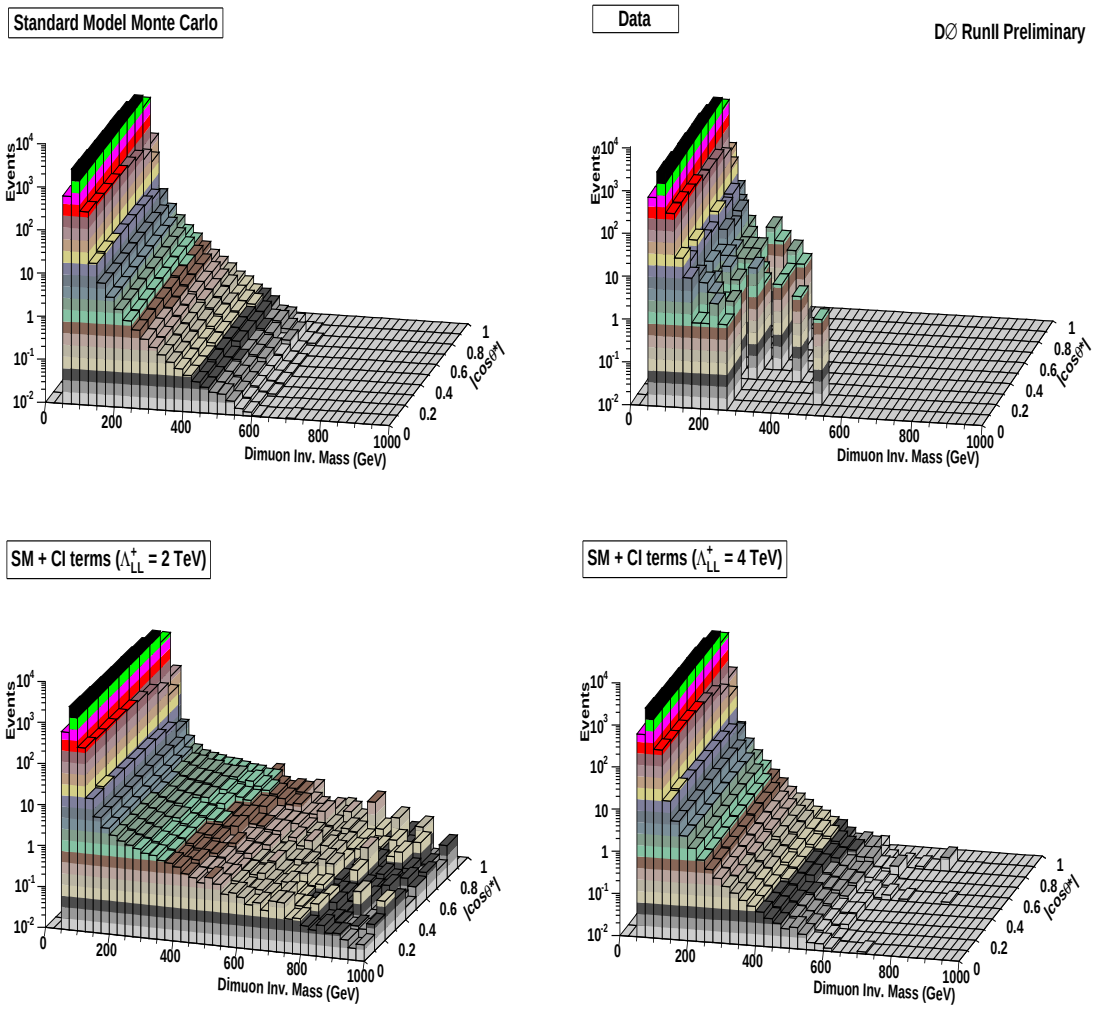

Figure 4.10. The distribution in M$\mu\mu$ vs. $|\cos\theta^*|$ space for data and MC for constructive LL channel. MC is scaled by the effective luminosity.

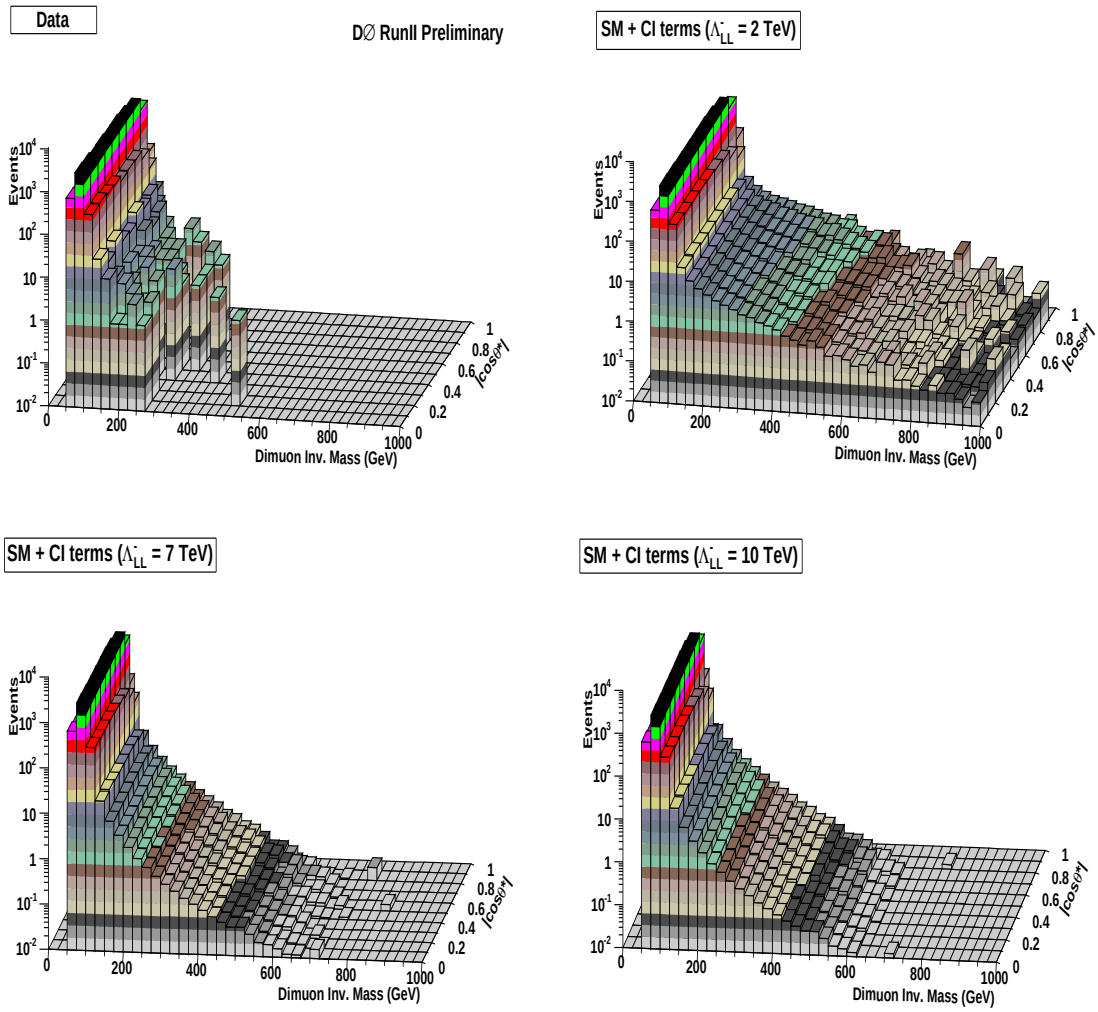

Figure 4.11. The distribution in M$\mu\mu$ vs. $|\cos\theta^*|$ space for data and MC for destructive LL channel. MC is scaled by the effective luminosity.

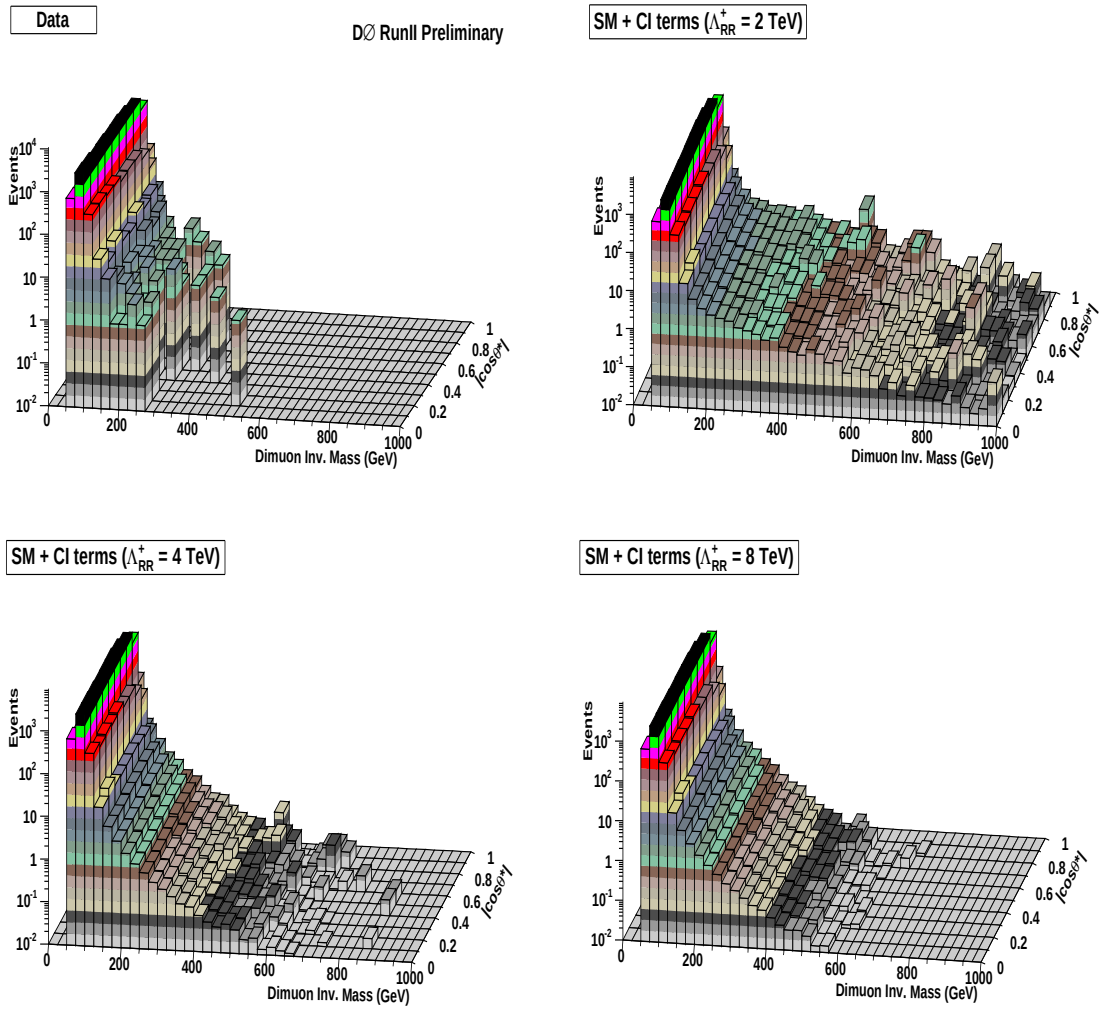

Figure 4.12. The distribution in M$\mu\mu$ vs. $|\cos\theta^*|$ space for data and MC for constructive RR channel. MC is scaled by the effective luminosity.

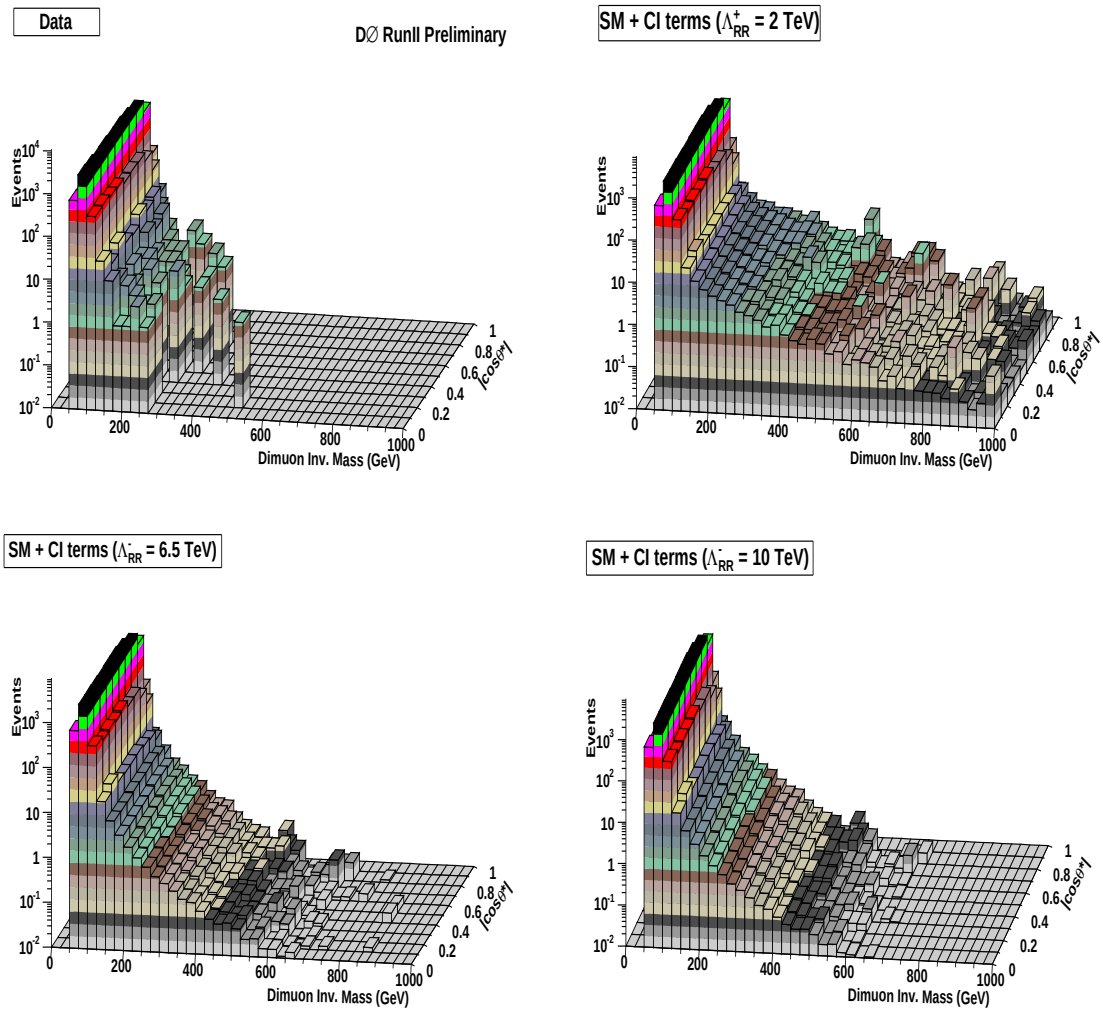

Figure 4.13. The distribution in M$\mu\mu$ vs. $|\cos\theta^*|$ space for data and MC for destructive RR channel. MC is scaled by the effective luminosity.

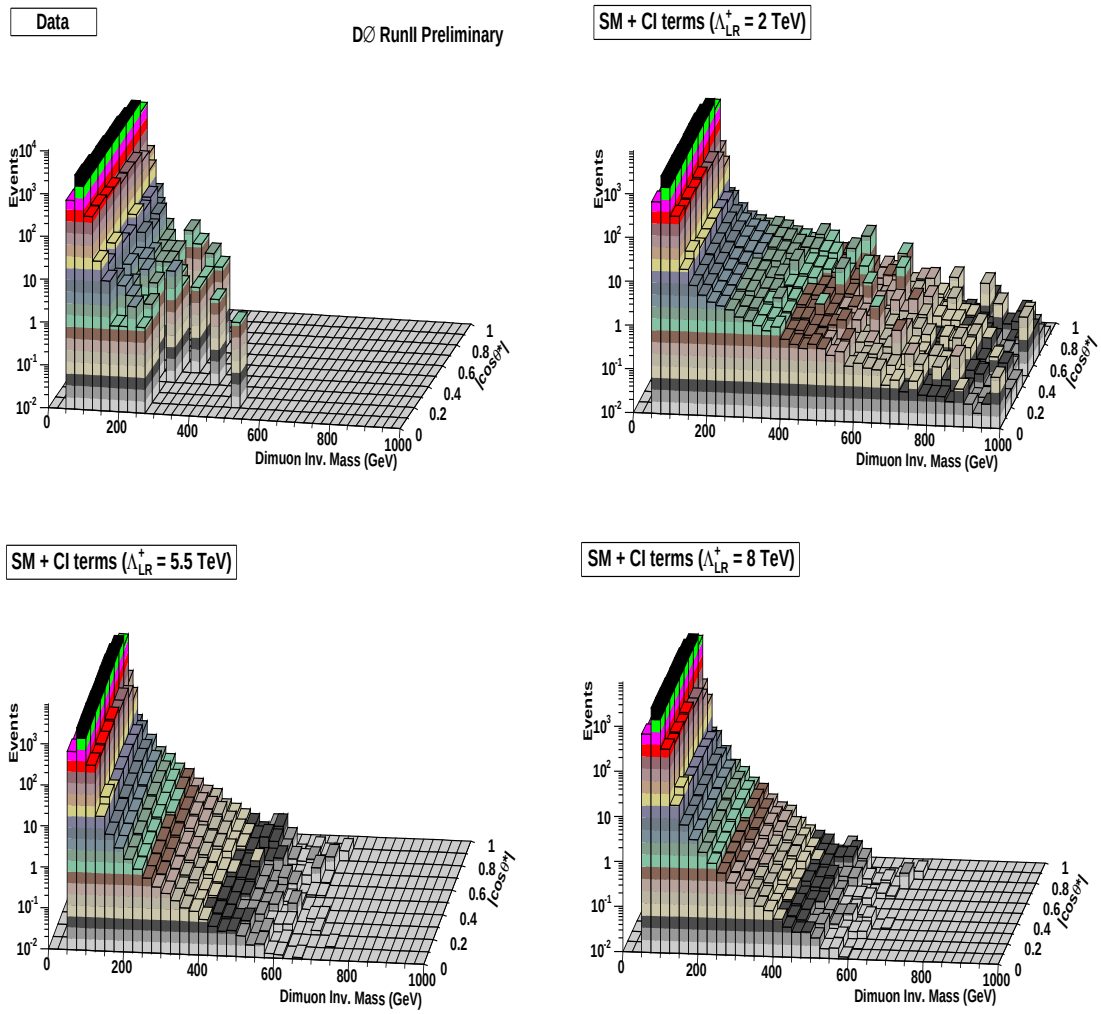

Figure 4.14. The distribution in M$\mu\mu$ vs. $|\cos\theta^*|$ space for data and MC for constructive LR channel. MC is scaled by the effective luminosity.

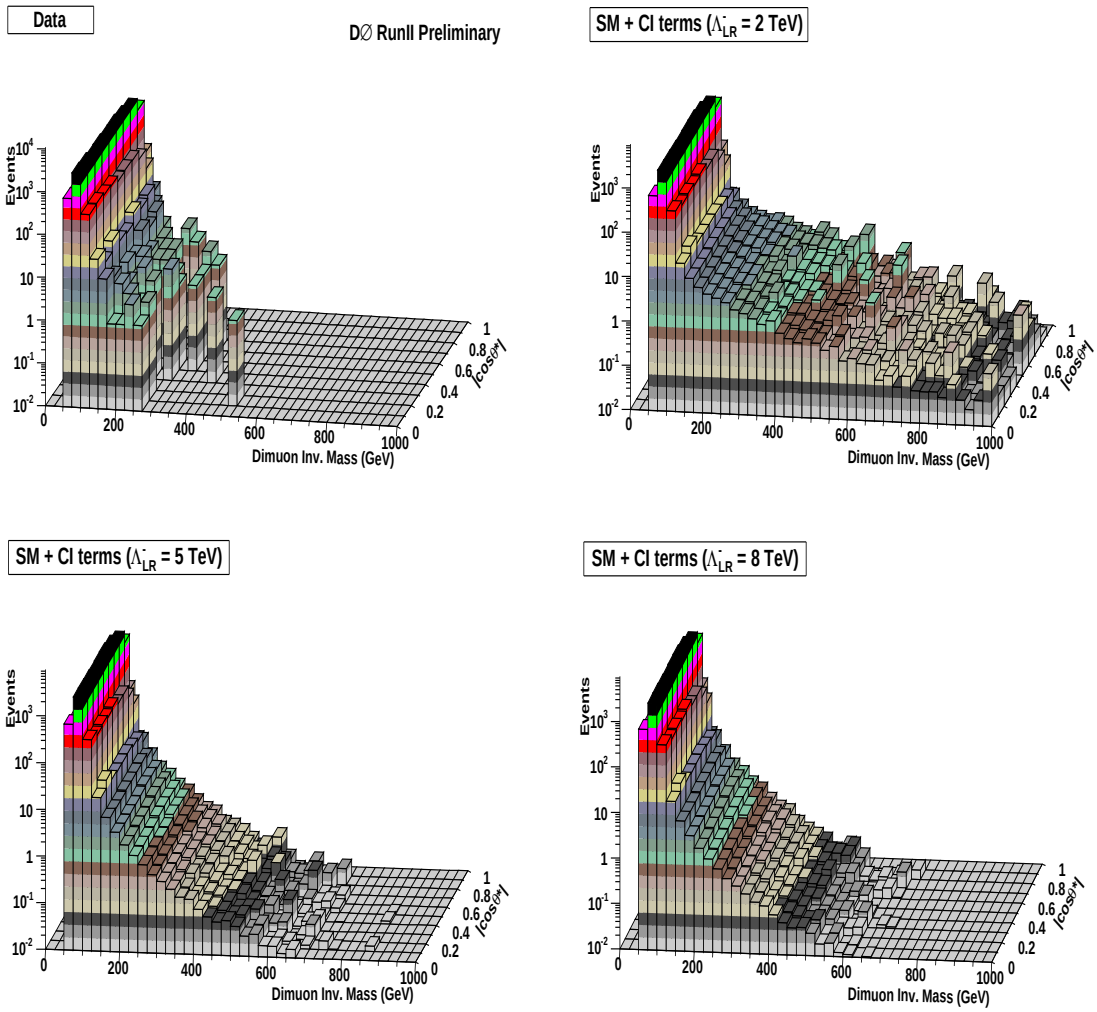

Figure 4.15. The distribution in M$\mu\mu$ vs. $|\cos\theta^*|$ space for data and MC for destructive LR channel. MC is scaled by the effective luminosity.

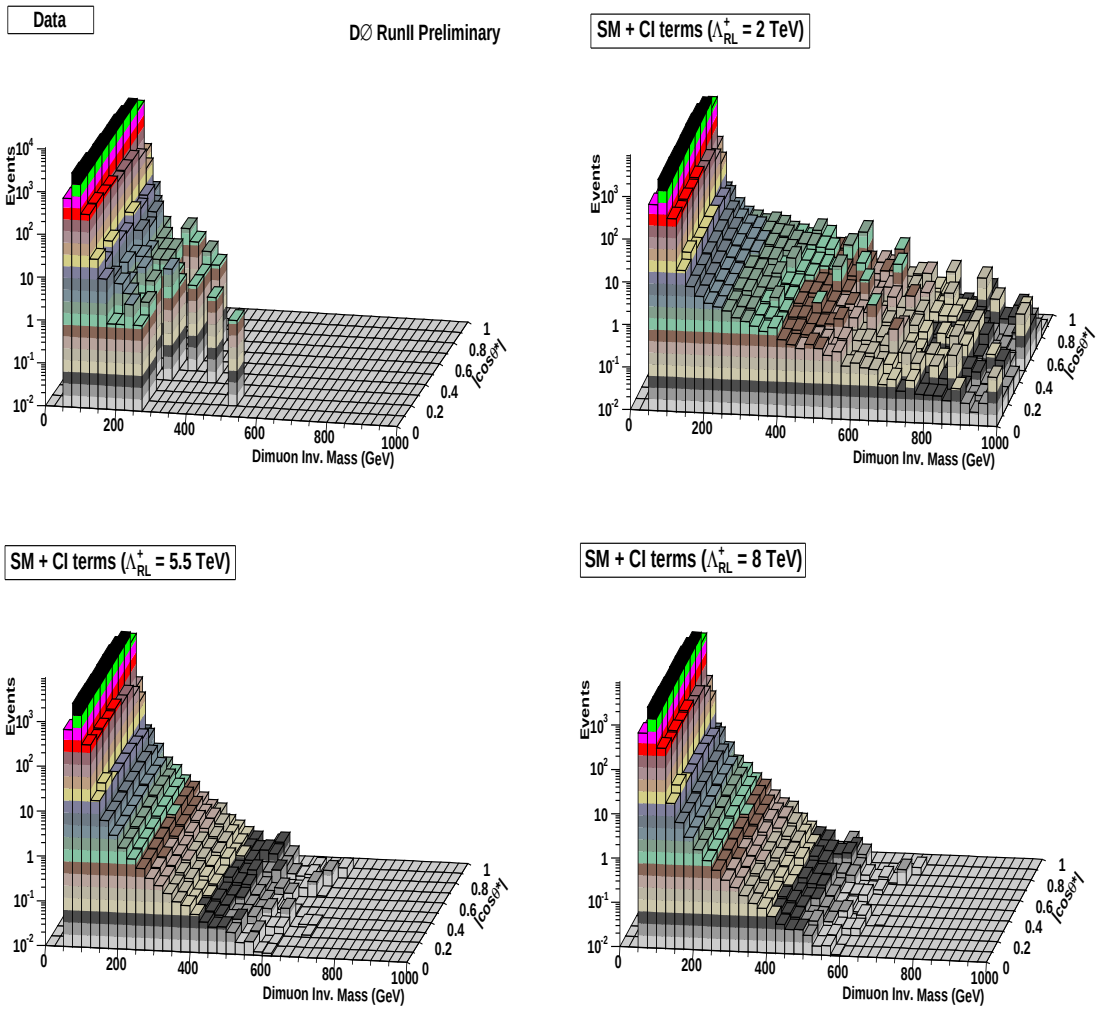

Figure 4.16. The distribution in M$\mu\mu$ vs. $|\cos\theta^*|$ space for data and MC for constructive RL channel. MC is scaled by the effective luminosity.

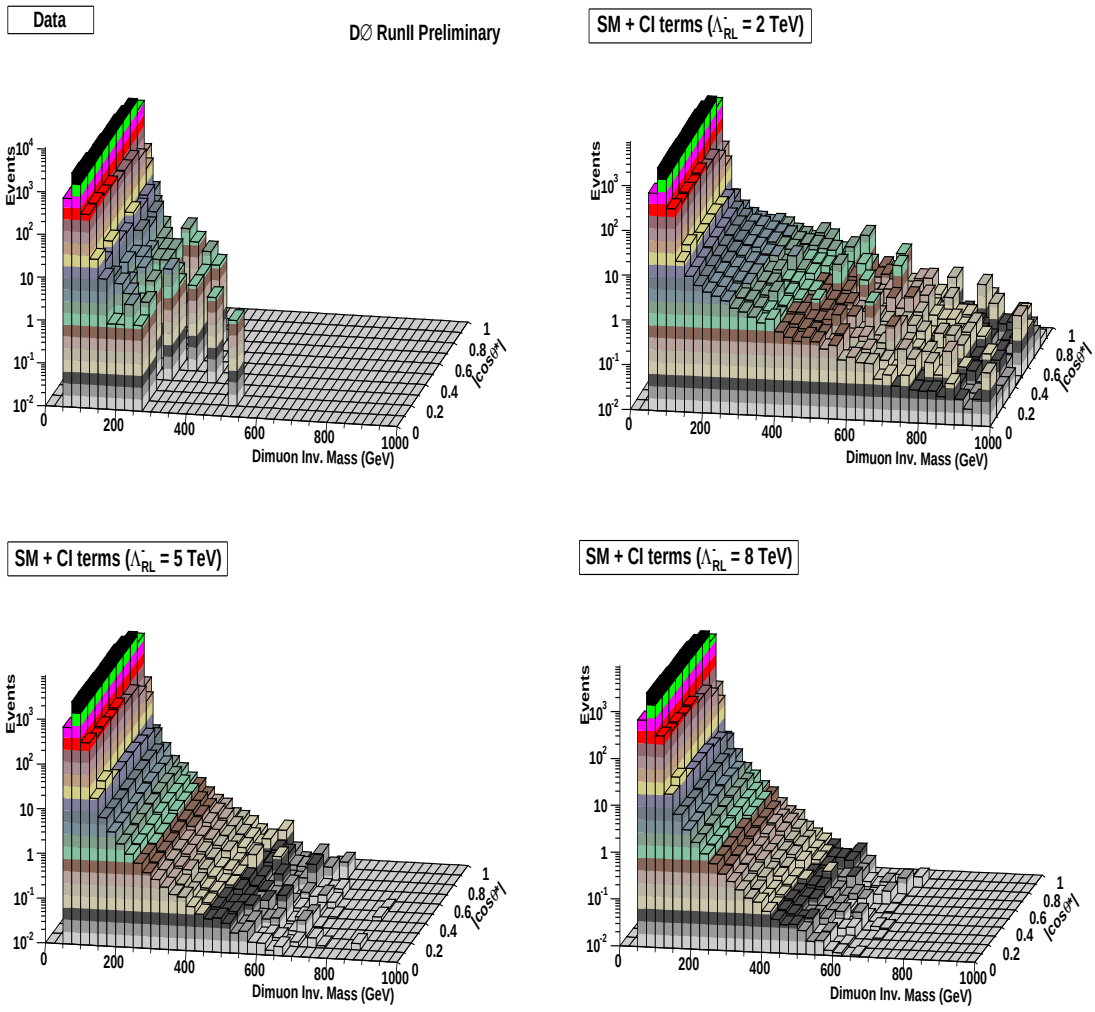

Figure 4.17. The distribution in M$\mu\mu$ vs. $|\cos\theta^*|$ space for data and MC for destructive RL channel. MC is scaled by the effective luminosity.

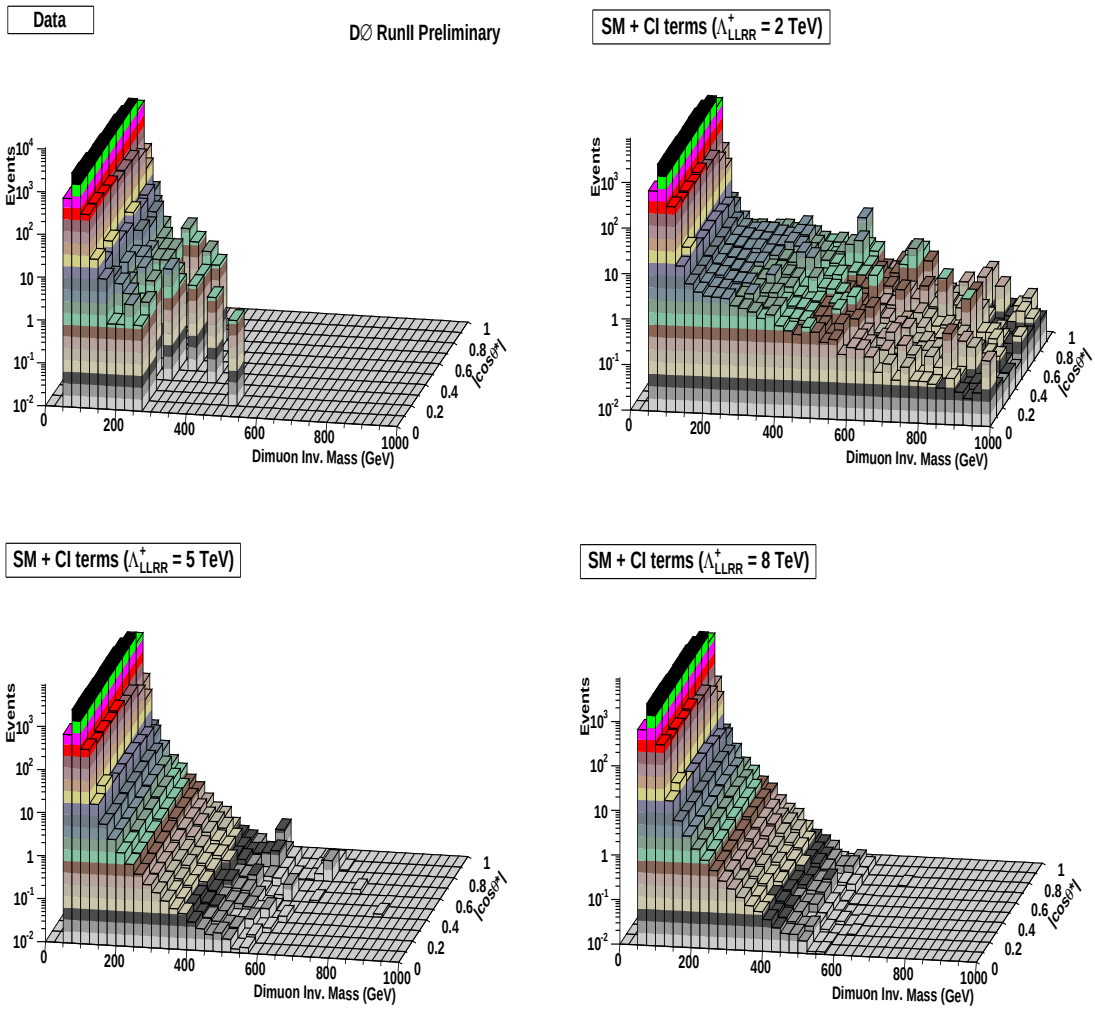

Figure 4.18. The distribution in M$\mu\mu$ vs. $|\cos\theta^*|$ space for data and MC for constructive LLRR channel. MC is scaled by the effective luminosity.

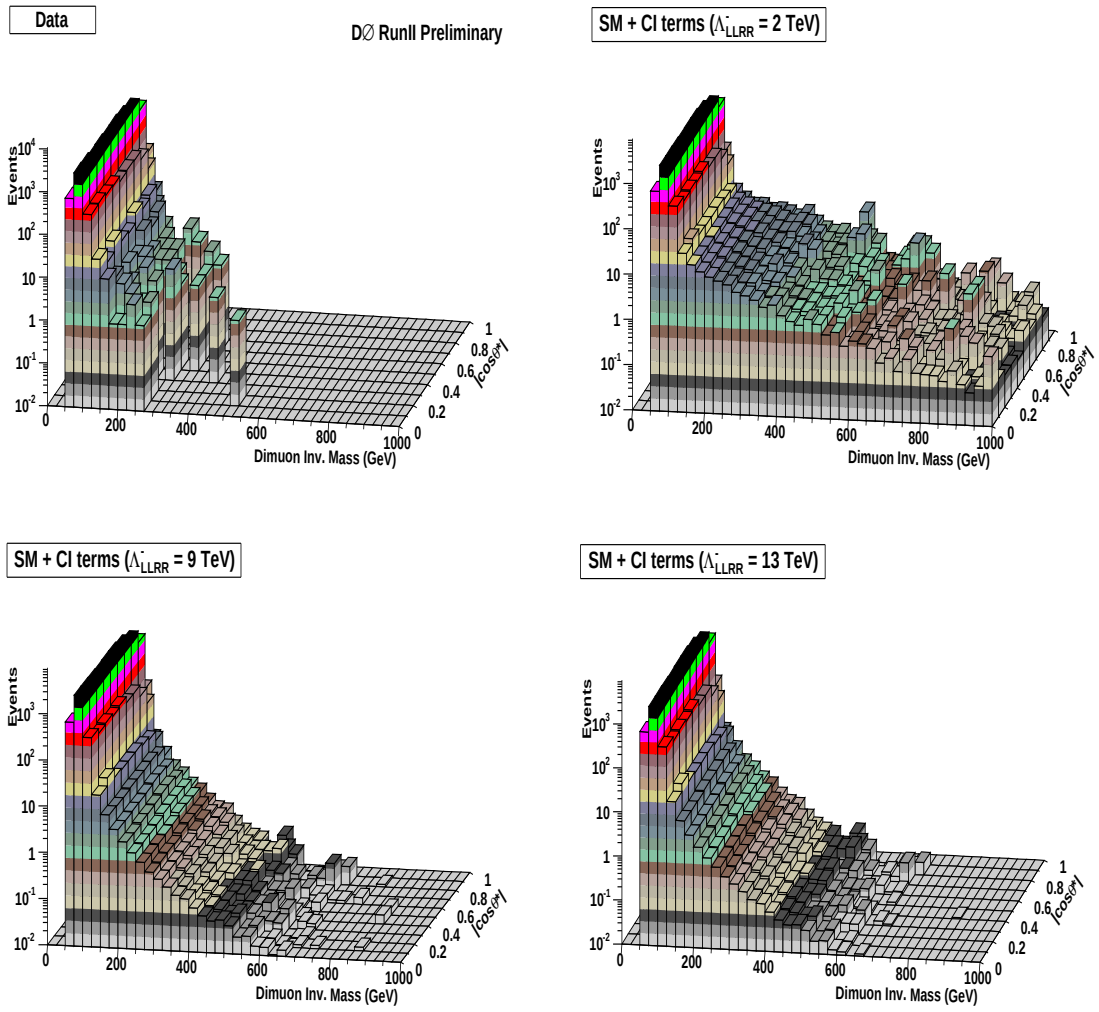

Figure 4.19. The distribution in M$\mu\mu$ vs. $|\cos\theta^*|$ space for data and MC for destructive LLRR channel. MC is scaled by the effective luminosity.

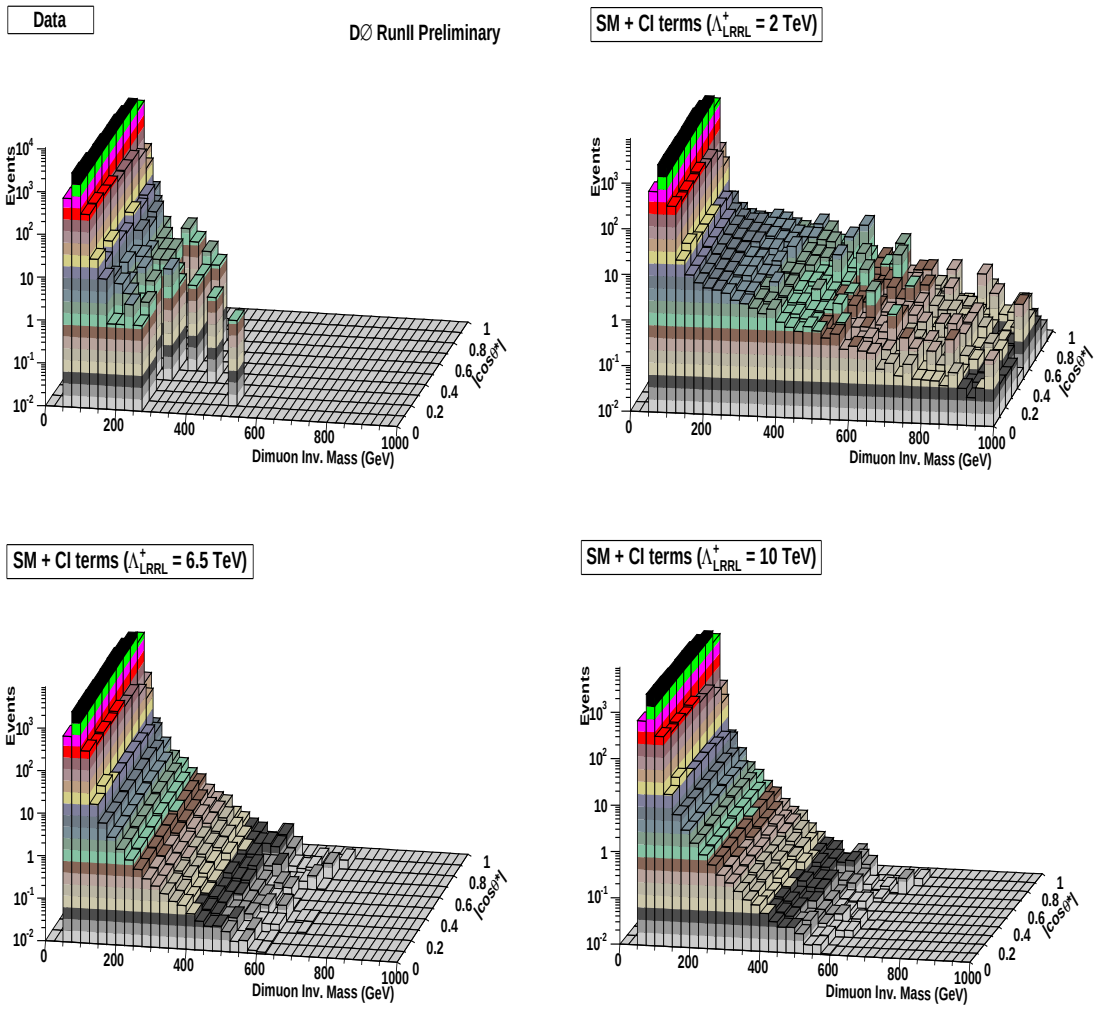

Figure 4.20. The distribution in M$\mu\mu$ vs. $|\cos\theta^*|$ space for data and MC for constructive LRRL channel. MC is scaled by the effective luminosity.

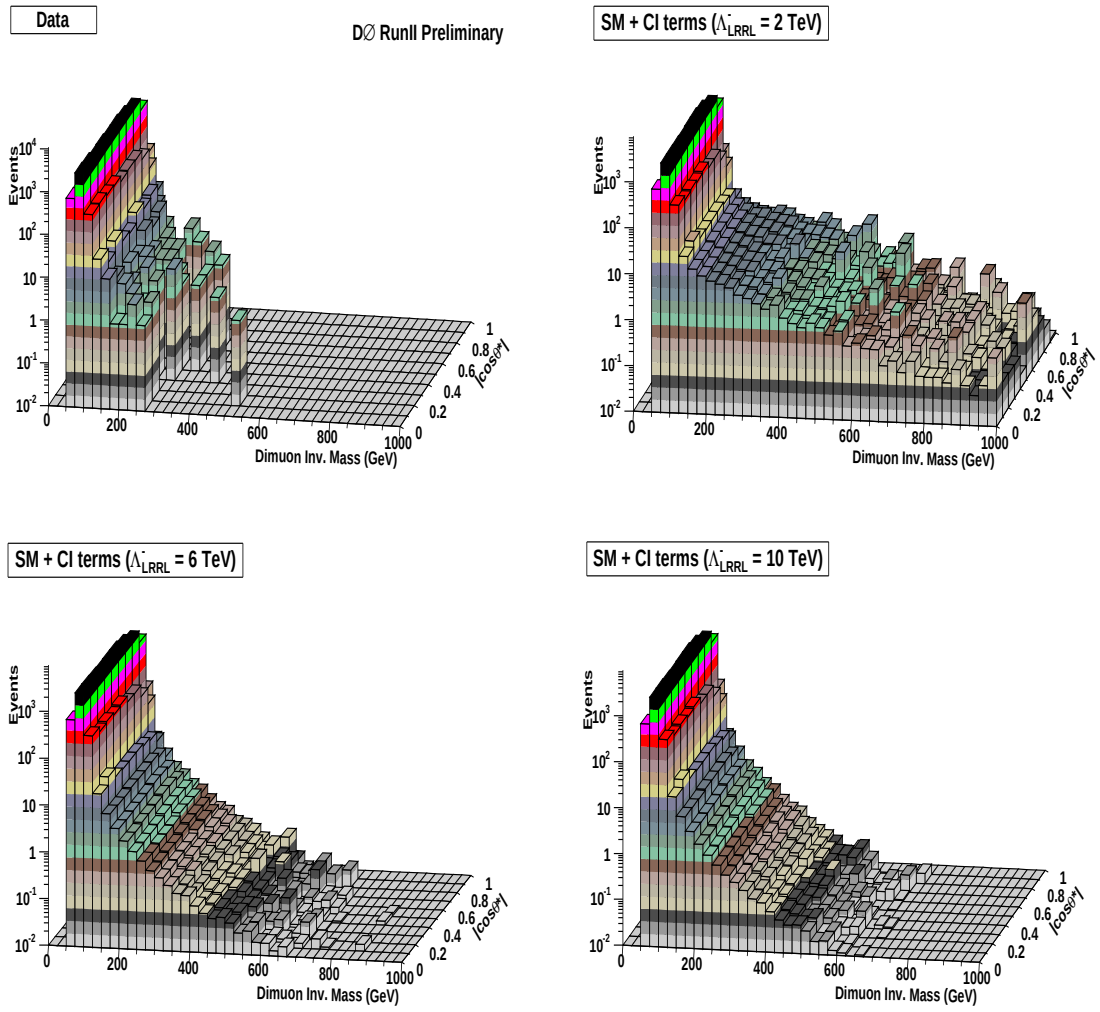

Figure 4.21. The distribution in M$\mu\mu$ vs. $|\cos\theta^*|$ space for data and MC for destructive LRRL channel. MC is scaled by the effective luminosity.

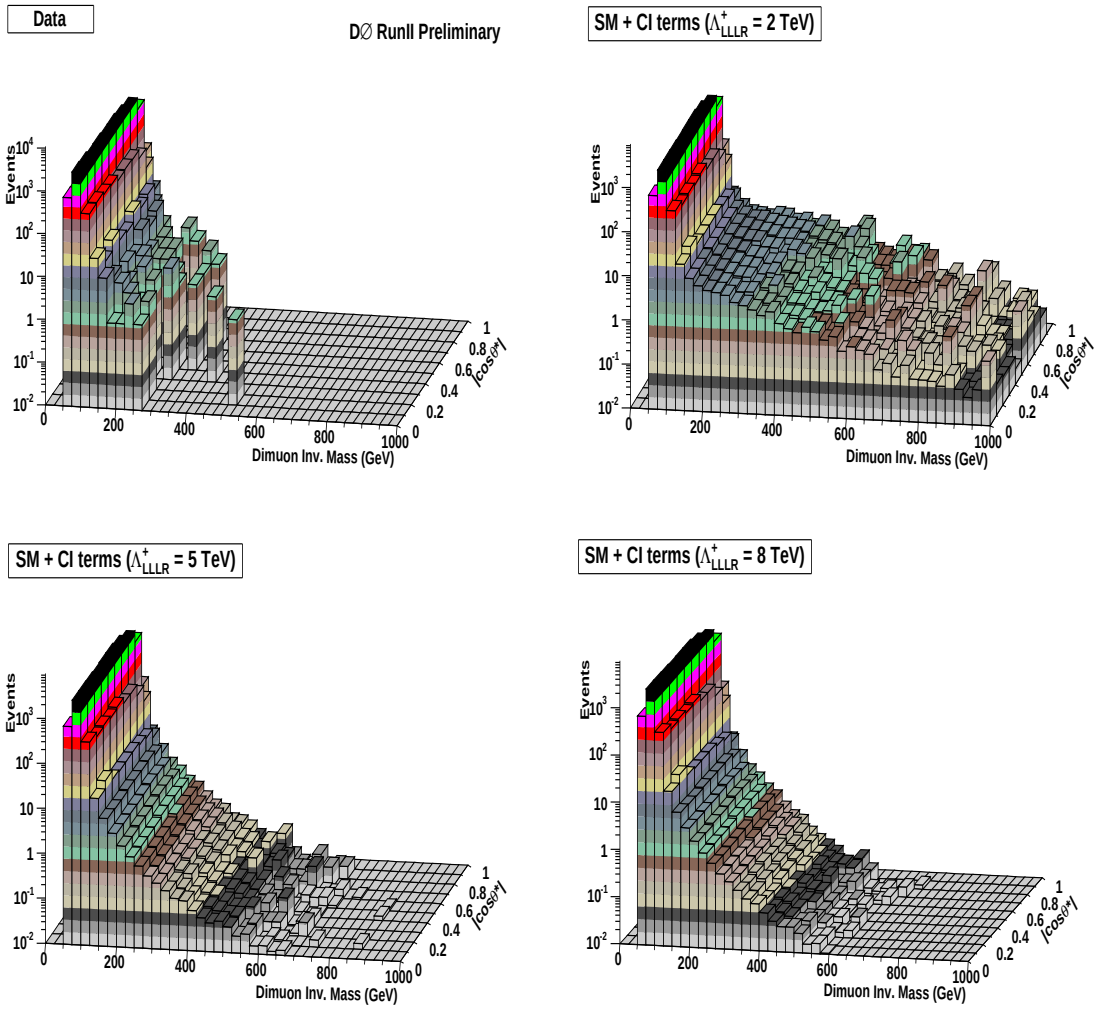

Figure 4.22. The distribution in M$\mu\mu$ vs. $|\cos\theta^*|$ space for data and MC for constructive LLLR channel. MC is scaled by the effective luminosity.

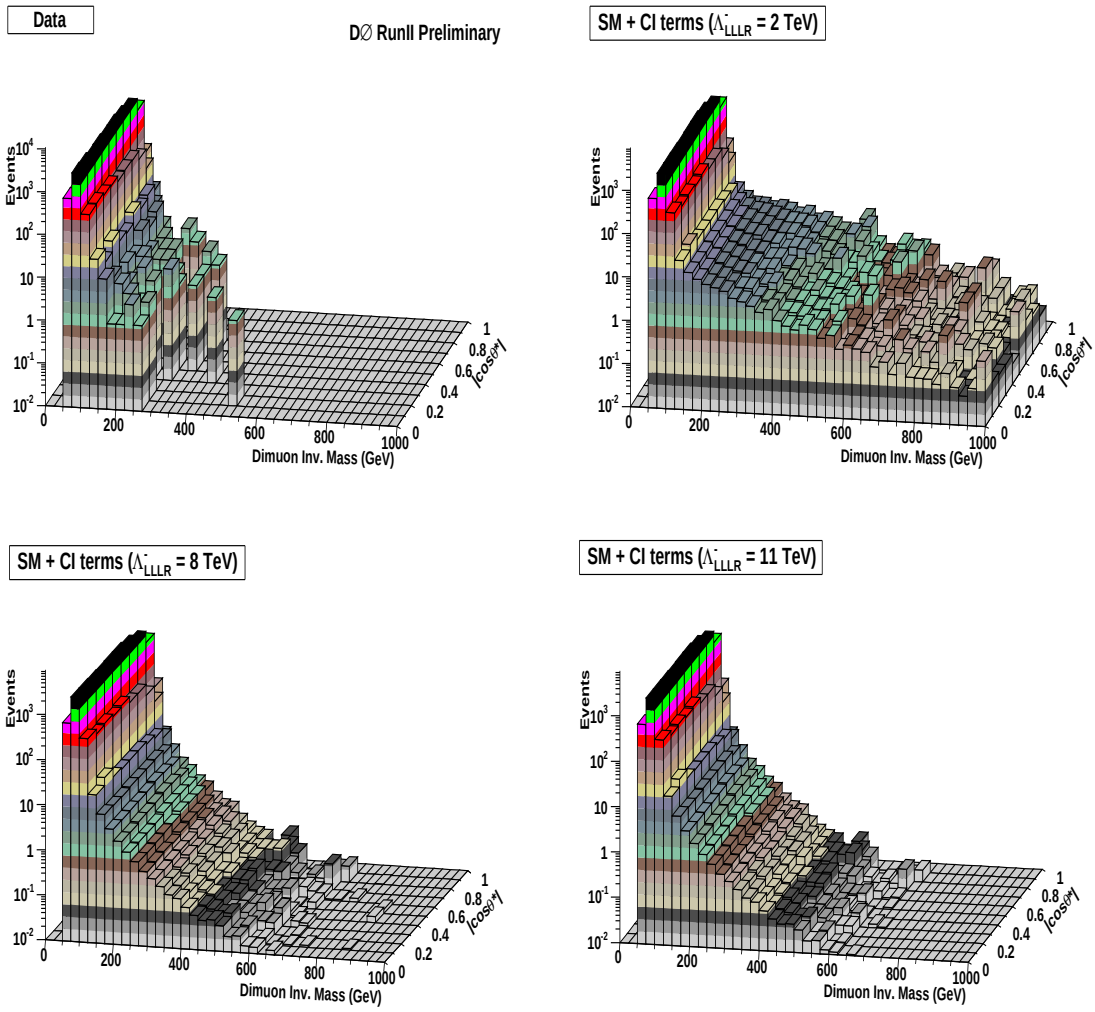

Figure 4.23. The distribution in M$\mu\mu$ vs. $|\cos\theta^*|$ space for data and MC for destructive LLLR channel. MC is scaled by the effective luminosity.

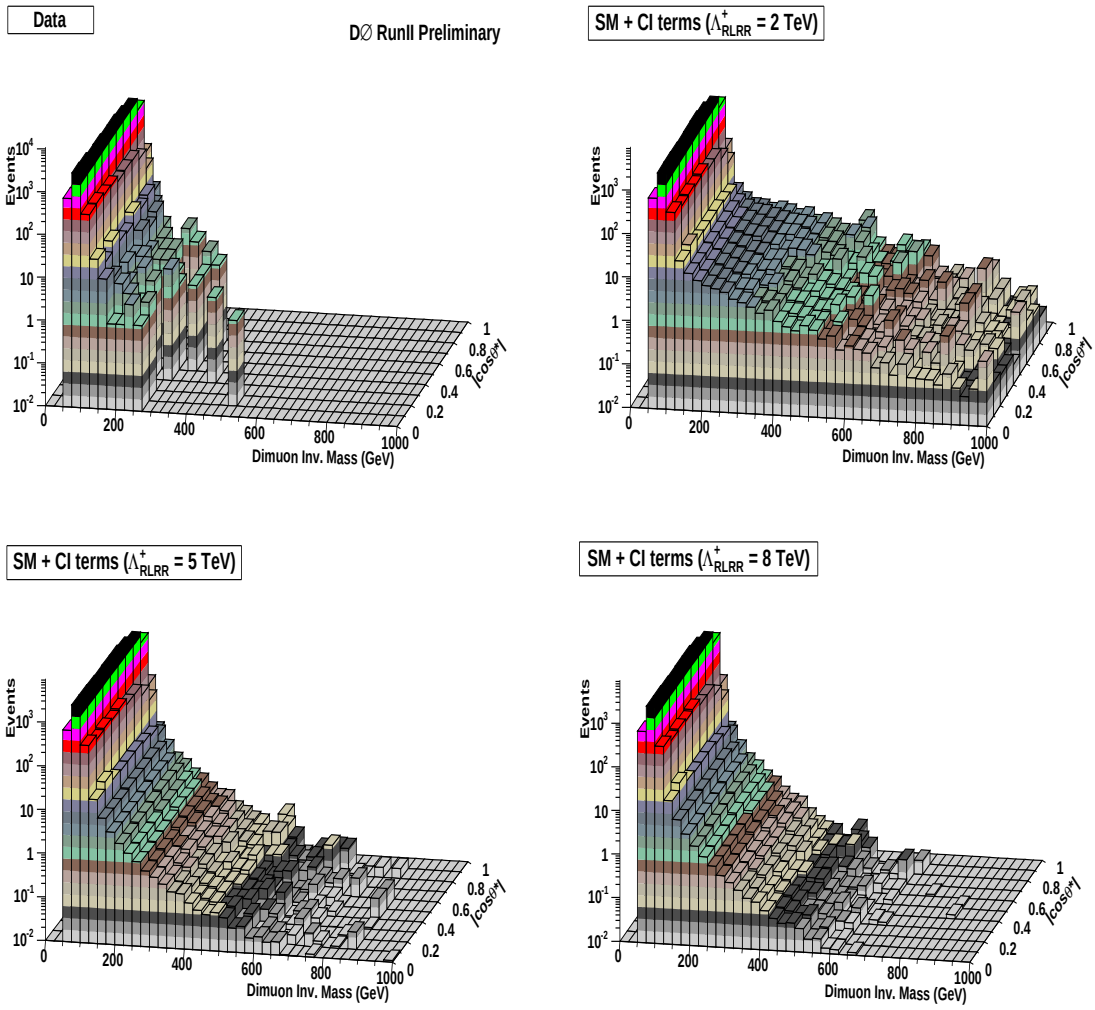

Figure 4.24. The distribution in M$\mu\mu$ vs. $|\cos\theta^*|$ space for data and MC for constructive RLRR channel. MC is scaled by the effective luminosity.

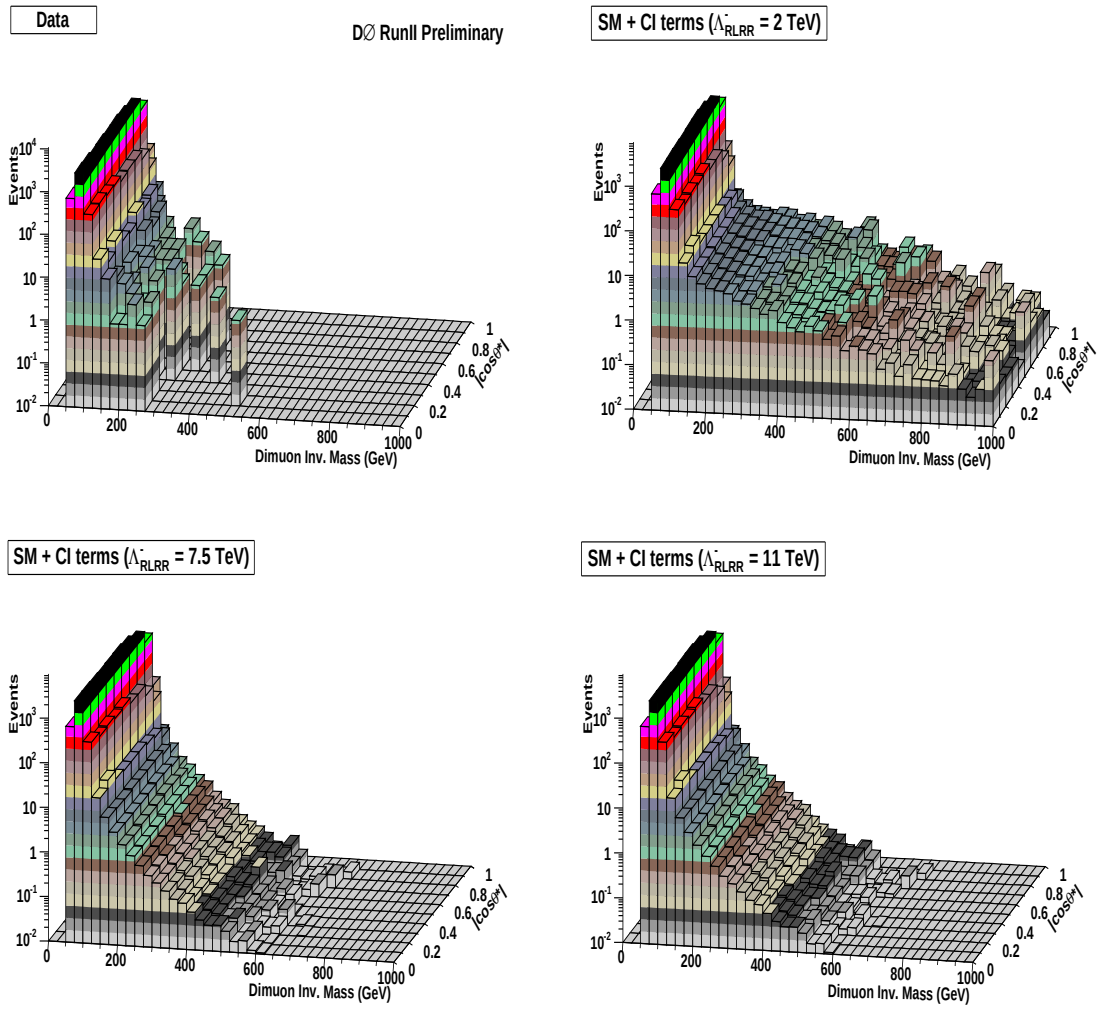

Figure 4.25. The distribution in M$\mu\mu$ vs. $|\cos\theta^*|$ space for data and MC for destructive RLRR channel. MC is scaled by the effective luminosity.

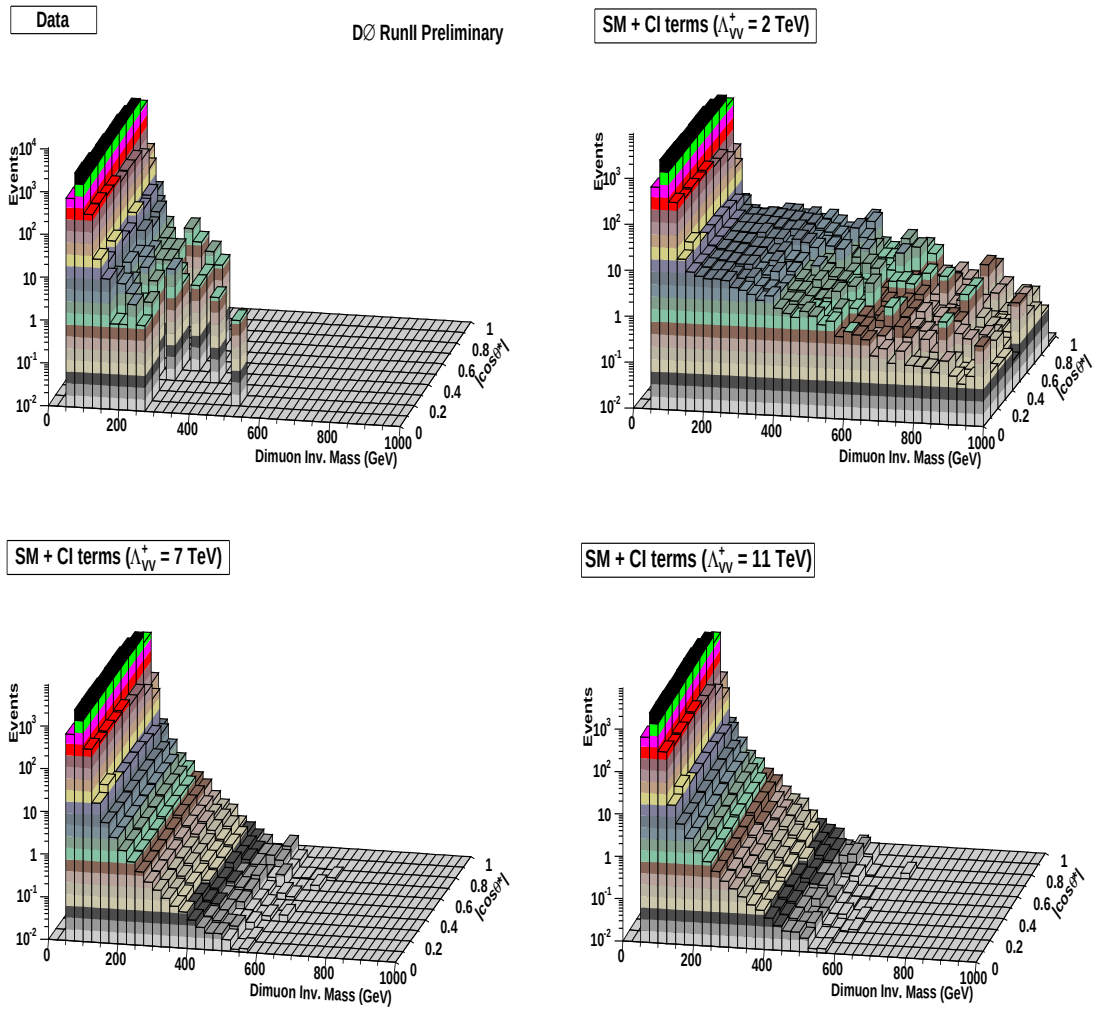

Figure 4.26. The distribution in M$\mu\mu$ vs. $|\cos\theta^*|$ space for data and MC for constructive VV channel. MC is scaled by the effective luminosity.

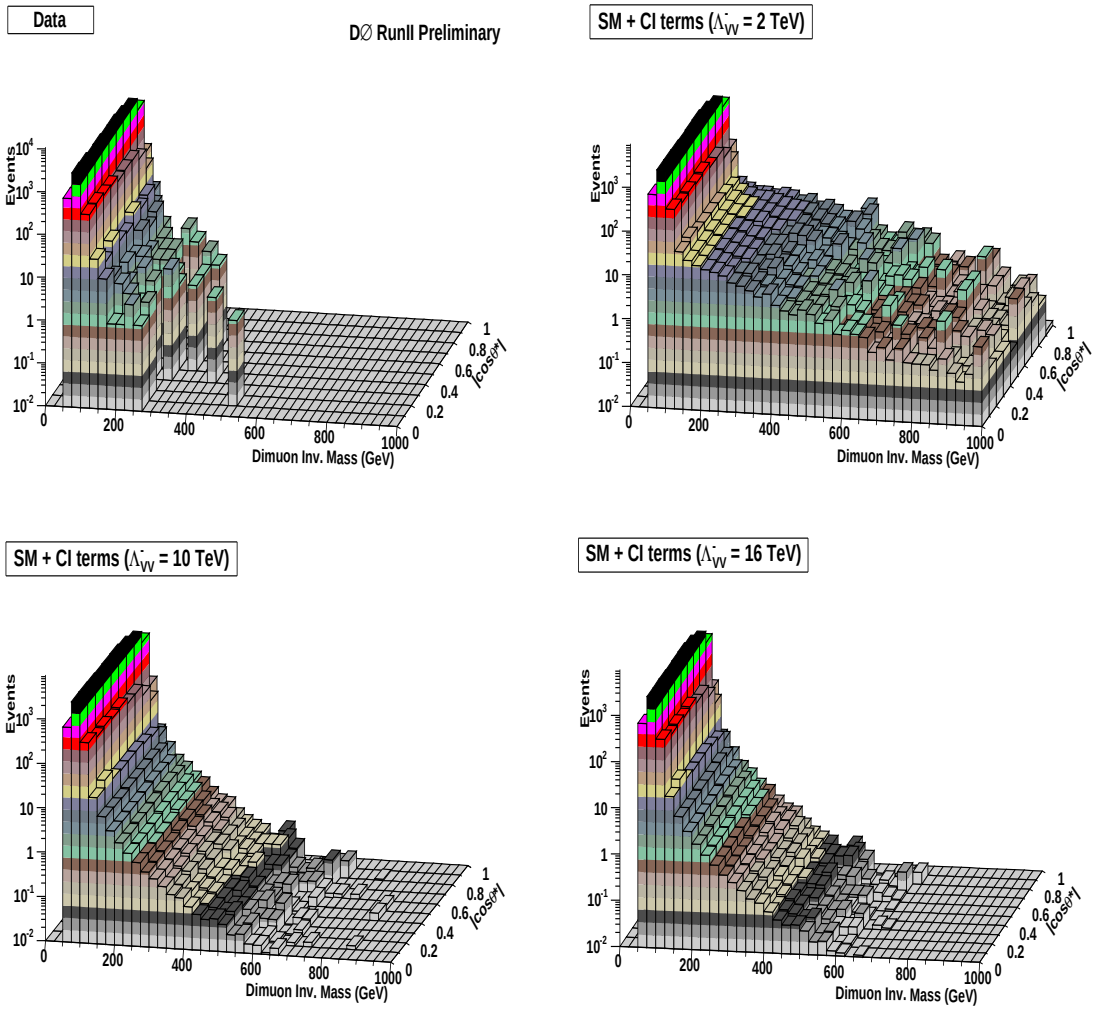

Figure 4.27. The distribution in M$\mu\mu$ vs. $|\cos\theta^*|$ space for data and MC for destructive VV channel. MC is scaled by the effective luminosity.

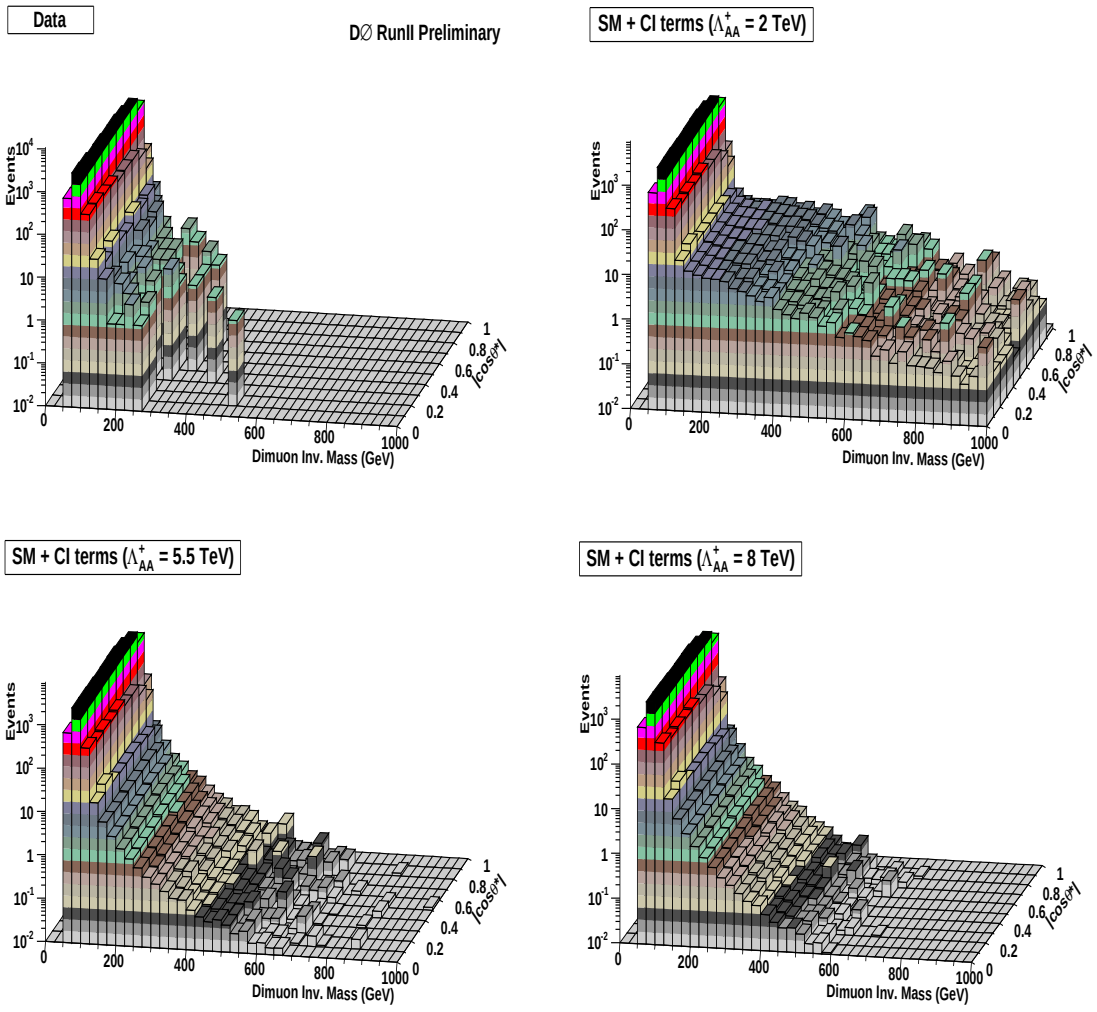

Figure 4.28. The distribution in M$\mu\mu$ vs. $|\cos\theta^*|$ space for data and MC for constructive AA channel. MC is scaled by the effective luminosity.

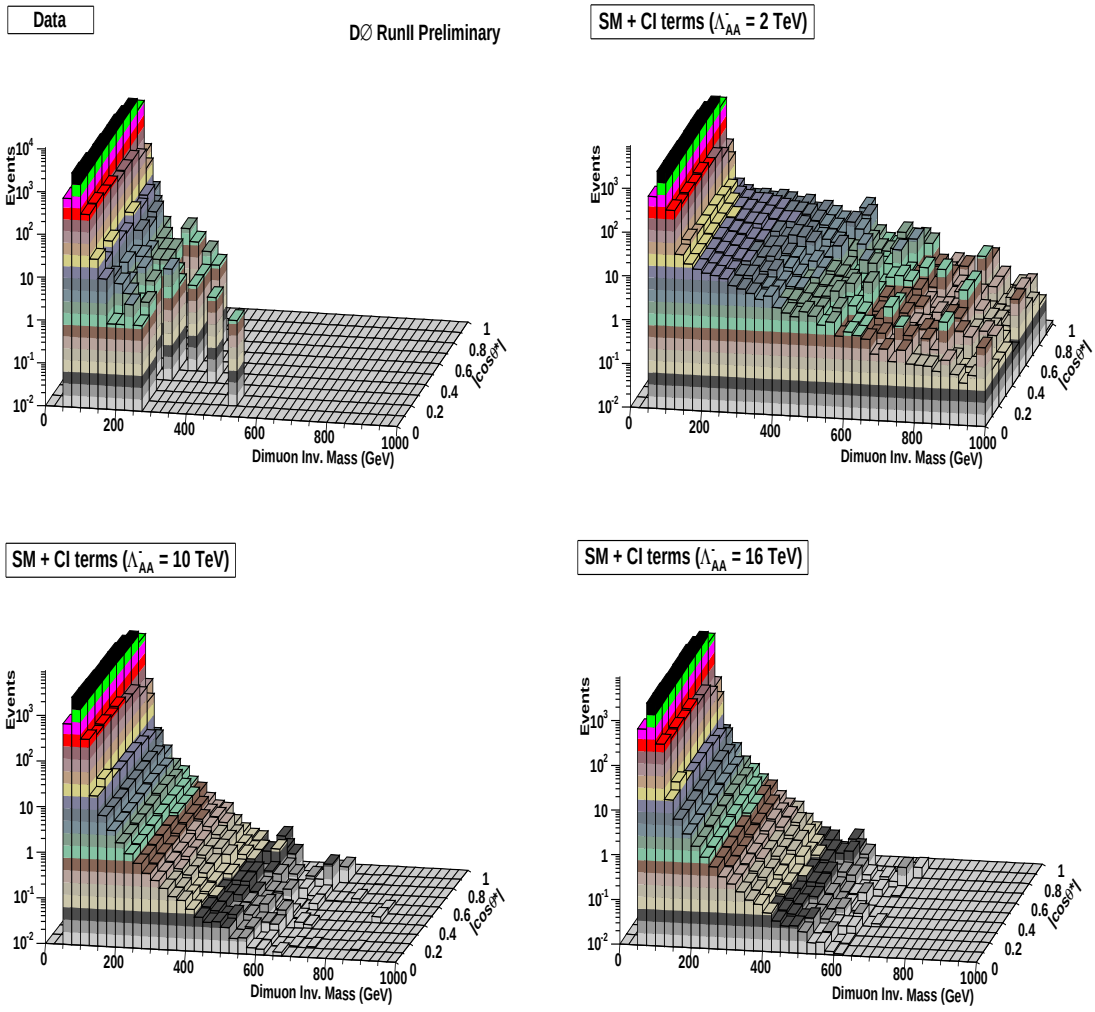

Figure 4.29. The distribution in M$\mu\mu$ vs. $|\cos\theta^*|$ space for data and MC for destructive AA channel. MC is scaled by the effective luminosity.

Further comparisons between data and background are shown in Figure 4.30. The plots also show good agreement between the data and MC (Standard Model prediction).

Table 4.4 helps to quantify the agreement between data and backgrounds, in mass space, by comparing the prediction for the background above a certain mass

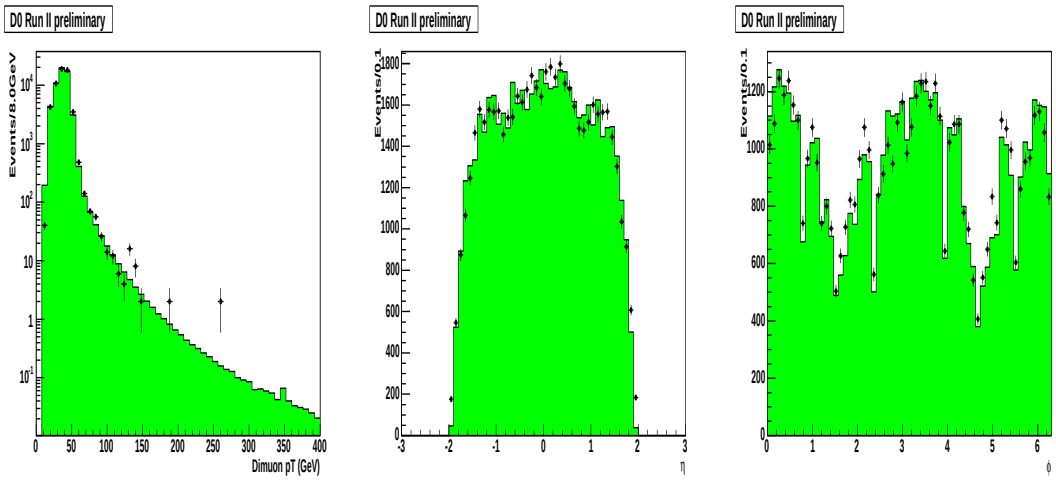

Figure 4.30. Comparison of kinematic variables p_T, η and ϕ for the data (points) and backgrounds (histogram).

cut data. It also gives the Poisson probability for the background to fluctuate to or beyond the observed number of events.

4.6 Cross Section Measurement

Having seen the good agreement between the dimuon data with the SM Drell-Yan background, we can proceed with a determination of the Drell-Yan cross section and setting limits on the compositeness scale Λ.

The probability that one will observe a number of events N_{obs} in an experiment when N_{exp} is the expected number of events is given by the Poisson (likelihood) distribution function:

$$P(N_{obs}|N_{exp}) = \frac{e^{-N_{exp}} N_{exp}^{N_{obs}}}{N_{obs}!} \tag{4.8}$$

The posterior probability that the expected number of events is N_{exp}, given the number of observed events is N_{obs}, can be obtained from the likelihood function

Table 4.4

DATA AND EXPECTED BACKGROUND COMPARISON FOR EVENTS ABOVE CERTAIN DIMUON MASS CUTOFF.

Minimum $M_{\mu\mu}$	Expected background	Data	Poisson probability
120 GeV	366.2	361	0.61
150 GeV	140.7	119	0.97
180 GeV	72.5	59	0.95
210 GeV	41.4	37	0.77
240 GeV	25.2	22	0.77
270 GeV	16.2	13	0.82
300 GeV	10.8	7	0.91
330 GeV	7.4	7	0.61
360 GeV	5.2	2	0.97
390 GeV	3.8	2	0.89
420 GeV	2.9	1	0.94
450 GeV	2.2	1	0.89
480 GeV	1.7	1	0.82
510 GeV	1.4	1	0.75
540 GeV	1.1	0	1.0

(Bayes theorem):

$$P(N_{exp}|N_{obs}) = \frac{P(N_{obs}|N_{exp})P(b,\varepsilon,L,\sigma_{DY})}{Z} \tag{4.9}$$

where b is the expected background, ε is the detector efficiency, σ_{DY} is the DY cross section and $P(b,\varepsilon,L,\sigma_{DY})$ is the joint prior probability. If b, ε, L and σ are considered to be independent then:

$$P(b,\varepsilon,L,\sigma_{DY}) = P(b)P(\varepsilon)P(L)P(\sigma_{DY}) \tag{4.10}$$

The prior probability of the cross section, $P(\sigma_{DY})$, is chosen to be flat i.e.

$$P(\sigma_{DY}) = \begin{cases} 1/\sigma_{max} & \text{if } 0 < \sigma_{DY} < \sigma_{max} \\ 0 & \text{otherwise} \end{cases} \tag{4.11}$$

where σ_{max} is taken to be sufficiently large that the likelihood for $\sigma_{DY} > \sigma_{max}$ is negligible.

Z is determined from the normalization condition:

$$\int_0^\infty db \int_0^\infty dL \int_0^1 d\epsilon \int_0^\infty d\sigma P(N_{exp}|N_{obs}) = 1 \tag{4.12}$$

The posterior probability for the cross section σ_{DY} can be calculated from:

$$P(\sigma_{DY}|N_{obs}) = \frac{1}{Z} \int_0^\infty db \int_0^\infty dL \int_0^1 d\epsilon \frac{e^{-N_{exp}} N_{exp}^{N_{obs}}}{N_{obs}!} P(b)P(\varepsilon)P(L)P(\sigma_{DY}) \tag{4.13}$$

In the high mass bins where no events are observed, a 95% confidence limit on the cross section is set:

$$0.95 = \int_0^{\sigma_{95\%}} d\sigma P(\sigma|N_o) \tag{4.14}$$

Figure 4.31 illustrates the measurement of the cross section in different mass bins. The measured cross sections are determined as the most probable value in those distributions.

4.7 Limit Calculation of Λ

The conditional probability for the observed event distribution to be d_o given the expected event distribution d_Λ can be expressed as the likelihood function:

$$P(d_o|d_\Lambda) = \prod_{k=1}^{n} \frac{e^{-N_\Lambda^k} N_\Lambda^{k N_o^k}}{N_o^k!} \tag{4.15}$$

The inverse of the above function i.e. the posterior probability is used to quantify the possible deviation of the expected event distribution from the observed event distribution. It is obtained using the Bayes theorem:

$$P(d_\Lambda|d_o) = \frac{P(d_o|d_\Lambda)P(b, L, \varepsilon, \Lambda)}{Z} \tag{4.16}$$

where Z is a constant, determined from the normalization condition of the sum of the above probability. $P(b, L, \varepsilon, \Lambda)$ is the joint prior probability for the dimuon detection efficiency ε^k, background b^k, luminosity L and the compositeness scale Λ. Those prior probabilities are assumed to be independent and to be Gaussian about their measured values with the Gaussian widths taken to be the errors in each dimuon mass bin. $P(\Lambda)$ is taken to be proportional to $1/\Lambda^2$ to ensure the assumed flat cross section.

The posterior probability that the compositeness scale is Λ, given the observed event distribution d_o, can be expressed as integration over the nuisance variables :

$$P(\Lambda|d_o) = \frac{1}{Z}\int_0^\infty db \int_0^\infty dL \int_0^1 d\varepsilon \prod_{k=1}^{n} \left[\frac{e^{-N_\Lambda^k} N_\Lambda^{k\,N_o^k}}{N_o^k!} e^{-\frac{1}{2}\left(\frac{\varepsilon^k - \varepsilon_m^k}{\delta\varepsilon^k}\right)^2} e^{-\frac{1}{2}\left(\frac{b^k - b_m^k}{\delta b^k}\right)^2} \right]$$

$$\mathrm{e}^{-\frac{1}{2}\left(\frac{L^k - L_m^k}{\delta L^k}\right)^2} P(\Lambda) \tag{4.17}$$

Calculation of $P(\Lambda|d_o)$ is performed over a range of Λ to get a distribution with respect to $1/\Lambda^2$, using a Monte Carlo integration. The confidence level limit of Λ, Λ_{limit}, can then be determined as numerical solution to the equation:

$$CL = \int_{\Lambda_{limit}}^{\infty} d\Lambda P(\Lambda|d_o) \tag{4.18}$$

Figure 4.32, 4.33, 4.34, illustrate the process described above for the one-dimensional analysis in mass for three chirality channels.

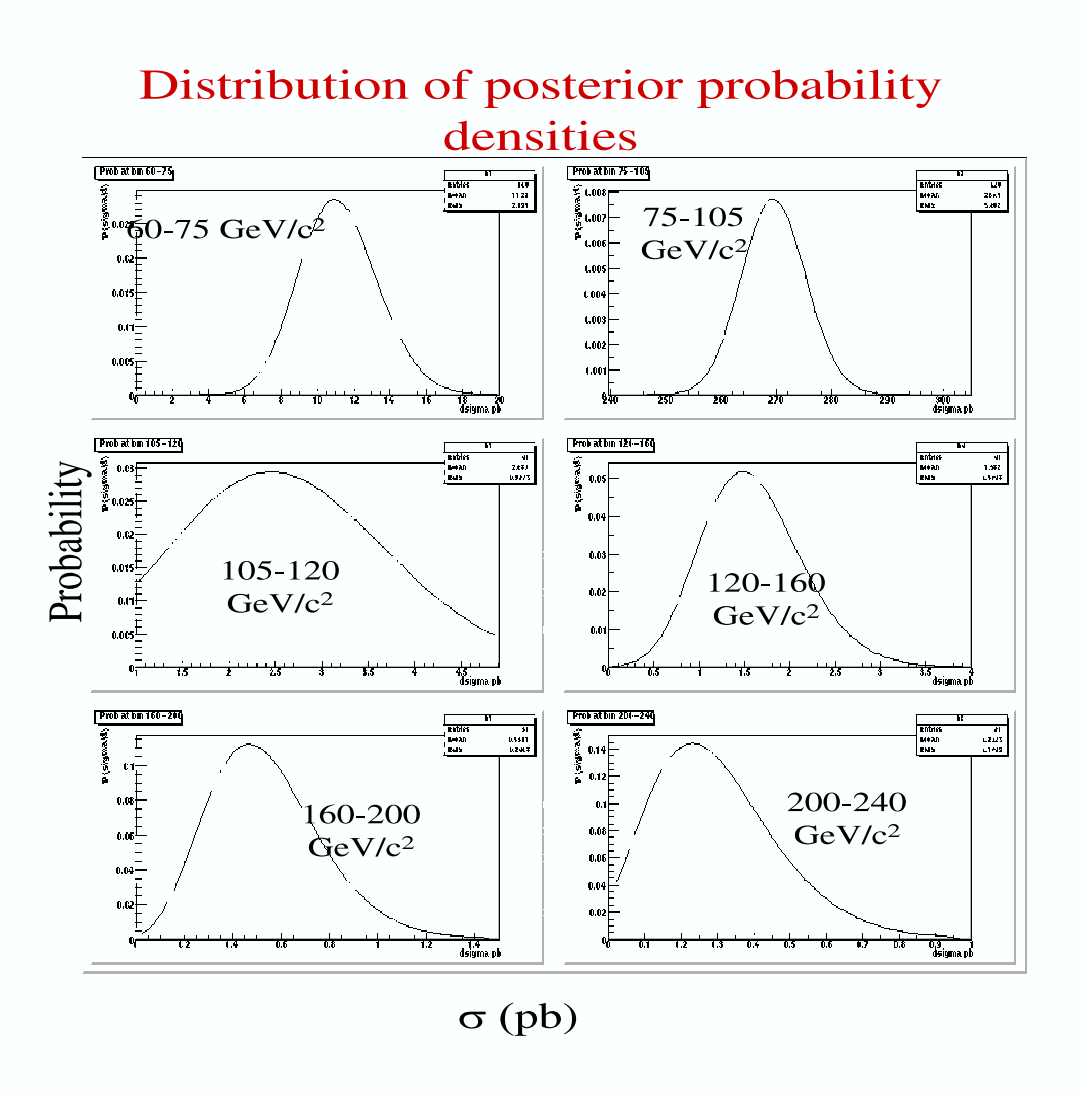

Figure 4.31. Cross section measurement.

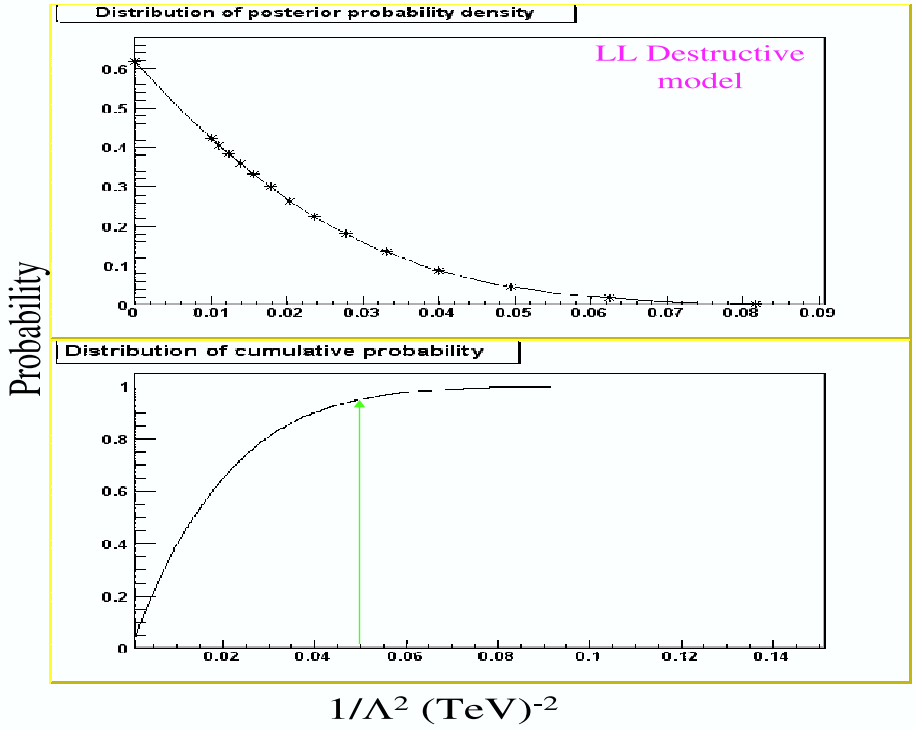

Figure 4.32. Limit calculation of Λ (for LL destructive model).

Since acceptance and all the efficiencies were included in the acceptance map, the calculations of posterior probabilities from equation 4.17 and hence of the 95% limits are significantly simplified using "effective luminosity" instead of the luminosity from the luminosity system. The effective luminosity can be determined from an in situ fit using the NLO Z-peak cross section (equal to the product of the K-factor and LO cross section) [43]. It then is used to normalize the MC to the data.

Systematic uncertainties involved in the measurement of cross sections and the Monte Carlo calculation are about 12%. This is mainly due to the energy depen-

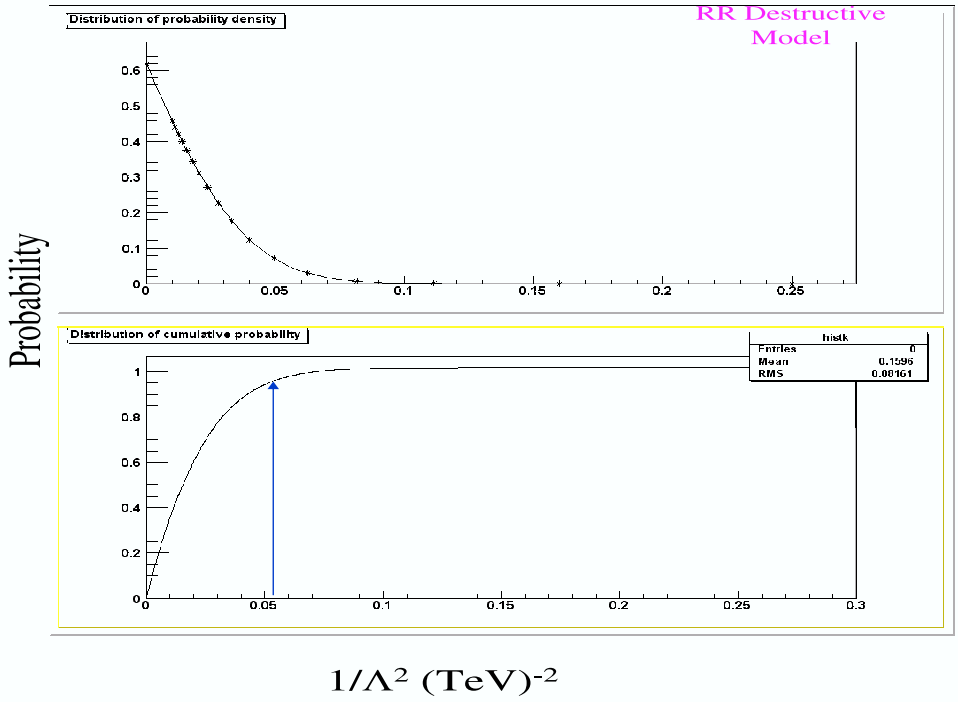

Figure 4.33. Limit calculation of Λ (for RR destructive model).

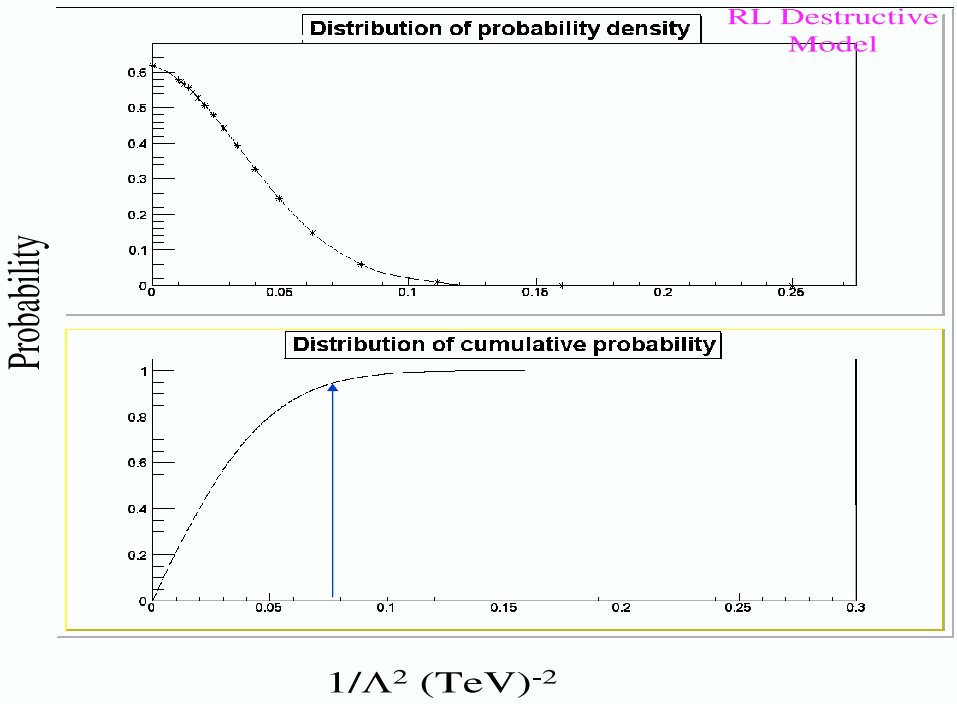

Figure 4.34. Limit calculation of Λ (for RL destructive model).

dence of the K factor (10%), the uncertainties of parton distribution functions (5%, including the dependence of K-factor on parton distribution functions) [43, 3, 19] and the p_T dependence of the efficiencies (5%). The latter 5% comes from full p14 MC and data comparison in the studies done by the Muon ID group [50]. The systematic uncertainties are used as input in the limit setting procedure in this analysis.

For one-dimensional analyses in mass and cosθ^*, the 95% confidence lower limit (CL) on the energy scale of compositeness Λ can be computed from equation 4.18 using the observed numbers of events (data distribution) in mass or cosθ^* and the calculated cross sections for various Λ values (the same method as in [40, 41, 3]). The measured cross section (see section 4.6) provides a consistency check for the one-dimensional analysis in mass.

For a two-dimensional analysis, the cross section is parametrized in each bin of the $M_{\mu\mu}$ and cosθ^* (where $M_{\mu\mu}$ ranges from 0 to 1500 GeV and cosθ^* from 0.0 to 1.0) as a 20×10 grid in terms of β_C (as $1/\Lambda^2$):

$$\sigma = \sigma_{SM} + \sigma_2\beta_C + \sigma_4{\beta_C}^2 \tag{4.19}$$

where σ_{SM} represents the Standard Model DY cross section, σ_2 is the cross section for the interference between the SM and the contact interaction, and σ_4 is the direct contact interaction cross section. The term β_C determines the magnitude of the effect of compositeness on the cross section. The cross section is used to generate the two-dimensional distributions of the SM, the interference and the contact interaction. They are fitted to data to extract the best value of β_C. The variable β_C is considered as a free parameter in this part of the fitting procedure. The fitting program uses the data, and the background and signal MC two-dimensional distributions to calculate the best value for β_C and its errors. If the data is consistent

with SM backgrounds, it also sets the 95% CL upper limit on β_C, denoted β_C^{95} which can be used to set a lower limit on the compositeness scale Λ.

The above procedure is repeated for each chirality channel. The best-fit values for β_C are shown in Table 4.5.

Table 4.5

BEST FIT VALUES FOR β_C FOR DIFFERENT CONSTRUCTIVE (β_C^+) AND DESTRUCTIVE (β_C^-) CONTACT INTERACTION MODELS IN THE DIMUON CHANNEL.

Model	$\beta_C^+(\text{TeV}^{-2})$	errors	$\beta_C^-(\text{TeV}^{-2})$	errors
LL	0.018	+0.021-0.017	0.000	+0.006-0.000
RR	0.020	+0.022-0.019	0.000	+0.007-0.000
LR	0.000	+0.015-0.000	0.007	+0.002-0.000
RL	0.000	+0.014-0.000	0.007	+0.018-0.000
LL+RR	0.013	+0.013-0.000	0.000	+0.003-0.000
LR+RL	0.000	+0.009-0.000	0.006	+0.012-0.000
LL-LR	0.018	+0.015-0.015	0.000	+0.005-0.000
RL-RR	0.000	+0.006-0.000	0.016	+0.014-0.015
VV	0.005	+0.008-0.000	0.000	+0.004-0.000
AA	0.017	+0.010-0.011	0.000	+0.003-0.000

The 95% CL limit setting described earlier in this section is applied for this two-dimensional analysis with slight modification.

The conditional probability to observe an event distribution $\text{d}_o = \{N_o^{ij}\}$ as a function of β_C can be expressed as the likelihood function:

$$P(d_o|d_{\beta_C}) = \prod_{ij} \frac{e^{-N_{\beta_C}^{ij}} N_{\beta_C}^{ij\ N_o^{ij}}}{N_o^{ij}!} \tag{4.20}$$

where $d_{\beta_C} = \{N_{\beta_C}^{ij}\}$, $N_{\beta_C}^{ij} = L\sigma_{ij}$, L is the effective luminosity, and σ_{ij} is the cross section given in Equation 4.19, integrated over bin (i,j) in $\text{M}_{\mu\mu}$ and $\cos\theta^*$. The

posterior probability is reconstructed using Bayes' theorem:

$$P(d_{\beta_C}|d_o) = \frac{P(d_o|d_{\beta_C})P(L,\beta_C)}{Z} \tag{4.21}$$

where Z is normalization constant, $P(L,\beta_C)$ is the joint prior probability for the effective luminosity and β_C that determines the compositeness signal behavior. Those prior probabilities are taken to be independent, thus:

$$P(L,\beta_C) = P(L)P(\beta_C) \tag{4.22}$$

$P(\beta_C)$ is assumed to be flat, i.e.

$$P(\beta_C) = \begin{cases} 1/\beta_C^{max} & \text{if } 0 < \beta_C < \beta_C^{max} \\ 0 & \text{otherwise} \end{cases} \tag{4.23}$$

where β_C^{max} is chosen to be sufficiently large to ensure that the likelihood that the true β_C is greater than β_C^{max} is negligibly small.

The posterior probability for β_C given the observed event distribution is d_o can be expressed as:

$$P(\beta_C|d_o) = \frac{1}{Z}\int dL\ P(d_o|d_{\beta_C})e^{-\frac{1}{2}\left(\frac{L-L_0}{\sigma_L}\right)^2} P(\beta_C) \tag{4.24}$$

where L_0 is the value for L and σ_L is its error.

The 95% CL limit for β_C can be determined from:

$$\int_0^{\beta_C^{95\%}} d\beta_C\ P(\beta_C|d_o) = 0.95 \tag{4.25}$$

The results of setting limits independently for each separate chirality channel of the contact interaction Lagrangian: LL, RR, LR, RL, LL+RR, LR+RL, LL-LR, RL-RR, VV and AA for the two-dimensional analysis in mass and cosθ^* are shown in Table 4.6. For comparison, previous results of a one-dimensional analysis in mass

from the DØ Run I and Run II dielectron channel are shown in Table 4.7 and Table 4.8, respectively.

Table 4.6

DØ RUN II 95% CL LOWER LIMIT (THIS ANALYSIS) ON COMPOSITENESS SCALE Λ FOR DIFFERENT CONSTRUCTIVE AND DESTRUCTIVE CONTACT INTERACTION MODELS IN DIMUON CHANNEL.

Model	Λ^+(TeV)	Λ^-(TeV)
LL	4.19	6.98
RR	4.15	6.74
LR	5.32	5.10
RL	5.31	5.17
LL+RR	5.05	9.05
LR+RL	6.45	6.12
LL-LR	4.87	7.74
RL-RR	5.07	7.41
VV	6.88	9.81
AA	5.48	9.76

By changing the number of bins used for $|\cos\theta^*|$ from 10 to 1, the 95% confidence limit using only the one-dimensional mass distribution can be calculated. The one-dimensional 95% CL limits on β_C are obtained for constructive chirality channels LL and RR:

$$\beta_{LL}^{1D95\%} = 6.06 \times 10^{-2} TeV^{-2}$$
$$\beta_{RR}^{1D95\%} = 6.06 \times 10^{-2} TeV^{-2}$$

These are about 6% and 4% worse than the limits obtained using two-dimensional distributions (5.71×10^{-2} and $5.80\times10^{-2} TeV^{-2}$ respectively).

For parity flipping constructive channels RL and LR and their combinations such as LRRL, RLRR, and VV, the gains of including $|\cos\theta^*|$ in a two-dimensional

Table 4.7

DØ RUN I 95% CL LOWER LIMIT ON COMPOSITENESS SCALE Λ FOR DIFFERENT CONSTRUCTIVE AND DESTRUCTIVE CONTACT INTERACTION MODELS IN DIELECTRON CHANNEL. ADAPTED FROM [3].

Model	Λ^+(TeV)	Λ^-(TeV)
LL	3.3	4.2
RR	3.3	4.0
LR	3.4	3.6
RL	3.3	3.7
LL+RR	4.2	5.1
LR+RL	3.9	4.4
LL-LR	3.9	4.5
RL-RR	4.0	4.3
VV	4.9	6.1
AA	4.7	5.5

Table 4.8

DØ RUN II 95% CL LOWER LIMIT ON COMPOSITENESS SCALE Λ FOR DIFFERENT CONSTRUCTIVE AND DESTRUCTIVE CONTACT INTERACTION MODELS IN DIELECTRON CHANNEL. ADAPTED FROM [20].

Model	Λ^+(TeV)	Λ^-(TeV)
LL	3.6	6.2
RR	4.3	5.0
LR	4.5	4.8
RL	3.8	5.8
LL+RR	4.1	7.9
LR+RL	5.0	6.0
LL-LR	4.8	6.4
RL-RR	4.7	6.8
VV	4.9	9.1
AA	5.7	7.8

analysis range from 10% to 22%:

$\beta_{LR}^{1D95\%} = 4.03 \times 10^{-2}$, 14% worse than its two-dimensional $\beta_{LR}^{2D95\%} = 3.53 \times 10^{-2}$

$\beta_{RL}^{1D95\%} = 4.21 \times 10^{-2}$, 19% worse than its two-dimensional $\beta_{RL}^{2D95\%} = 3.55 \times 10^{-2}$

$\beta_{LRRL}^{1D95\%} = 2.94 \times 10^{-2}$, 22% worse than its two-dimensional $\beta_{LRRL}^{2D95\%} = 2.40 \times 10^{-2}$

$\beta_{RLRR}^{1D95\%} = 2.01 \times 10^{-2}$, 10% worse than its two-dimensional $\beta_{RLRRL}^{2D95\%} = 1.82 \times 10^{-2}$

$\beta_{VV}^{1D95\%} = 2.52 \times 10^{-2}$, 19% worse than its two-dimensional $\beta_{VV}^{2D95\%} = 2.11 \times 10^{-2}$

All these limits are in unit of TeV^{-2}. These are in the range predicted in the study [11], justifying the use of the two-dimensional distribution in mass and $|\cos\theta^*|$.

For a sensitivity study, 200 trial experiments were run, using randomly filled two dimensional histograms in $M_{\mu\mu}$ and $|\cos\theta^*|$ according to the SM background and the effective luminosity. The two-dimensional SM histograms were fluctuated using Poisson statistics and refilled. Then the limit-setting procedure was applied to find 95% CL limit. This was done for each chirality channel (for constructive and destructive contact interactions). The distributions of 95% CL limits on β_C for the 200 trials for chirality channels LL, RR, LR, RL, LL+RR, LR+RL, LL-LR, RL-RR, VV and AA are shown in Figure 4.35, Figure 4.36, Figure 4.37, Figure 4.38, Figure 4.39, Figure 4.40, Figure 4.41, Figure 4.42, Figure 4.43, and Figure 4.44. It shows that results (Table 4.6) are within the expected sensitivity.

The best fit values of β_C for those channels are 5.71×10^{-2}, 2.05×10^{-2}, 5.80×10^{-2}, 2.22×10^{-2}, 3.53×10^{-2}, 3.84×10^{-2}, 3.55×10^{-2}, 3.74×10^{-2}, 3.92×10^{-2}, 1.22×10^{-2}, 2.40×10^{-2}, 2.67×10^{-2}, 4.22×10^{-2}, 1.67×10^{-2}, 1.82×10^{-2}, 3.89×10^{-2}, 2.11×10^{-2}, 1.04×10^{-2}, 3.33×10^{-2}, and 1.05×10^{-2} respectively.

The present limits are now the most stringent set thus far in the dimuon channel by any experiment.

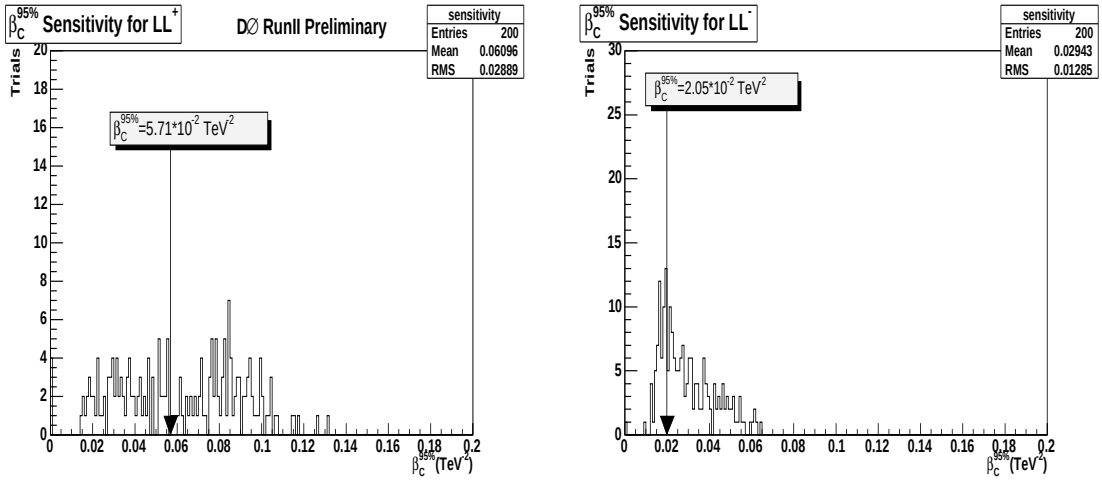

Figure 4.35. The distribution of best fit values on β_C for 200 MC trials for LL (constructive and destructive)

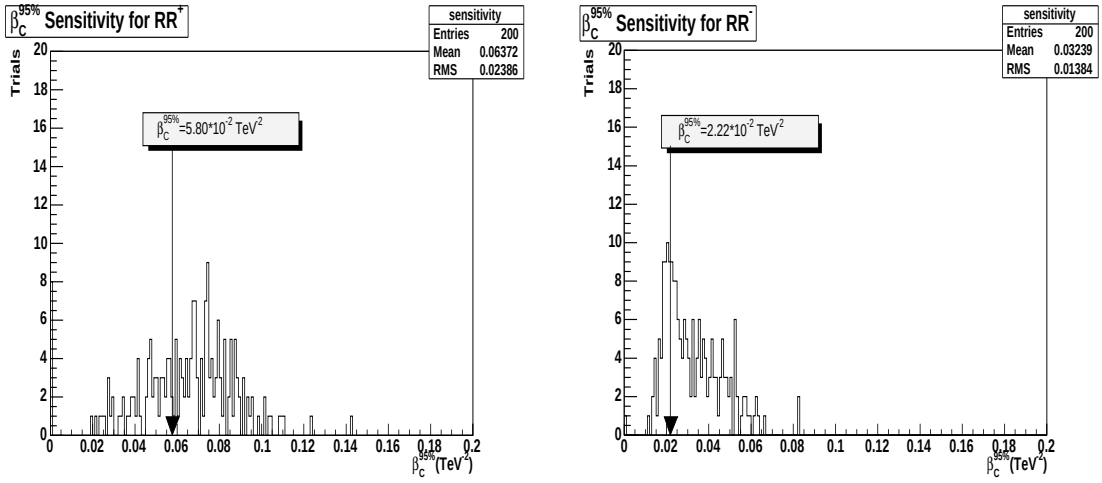

Figure 4.36. The distribution of best fit values on β_C for 200 MC trials for RR (constructive and destructive)

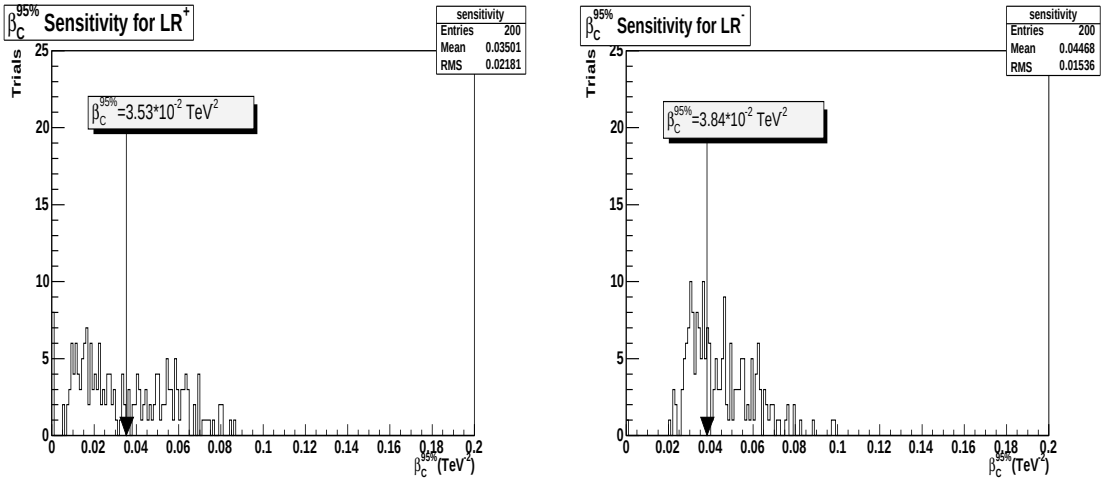

Figure 4.37. The distribution of best fit values on β_C for 200 MC trials for LR (constructive and destructive)

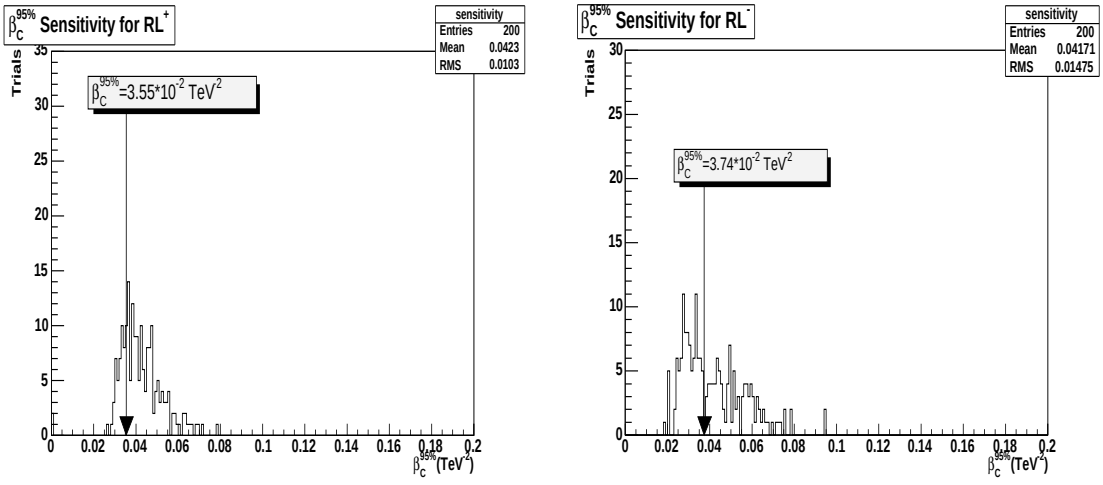

Figure 4.38. The distribution of best fit values on β_C for 200 MC trials for RL (constructive and destructive)

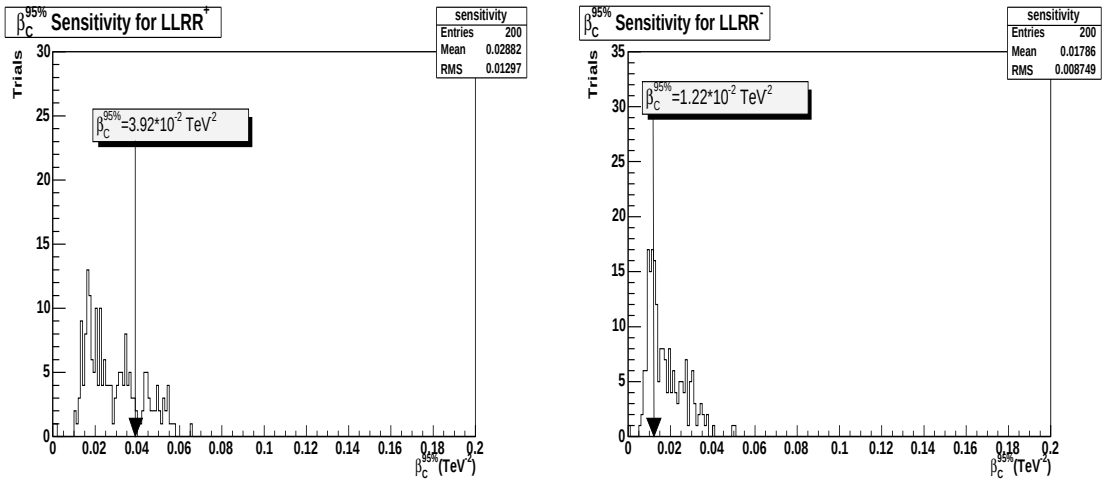

Figure 4.39. The distribution of best fit values on β_C for 200 MC trials for LLRR (constructive and destructive)

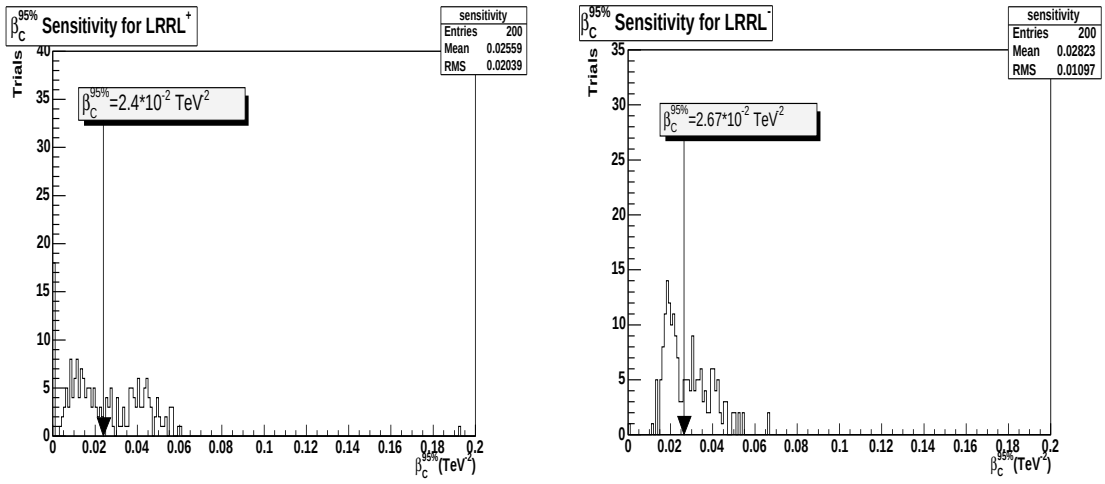

Figure 4.40. The distribution of best fit values on β_C for 200 MC trials for LRRL (constructive and destructive)

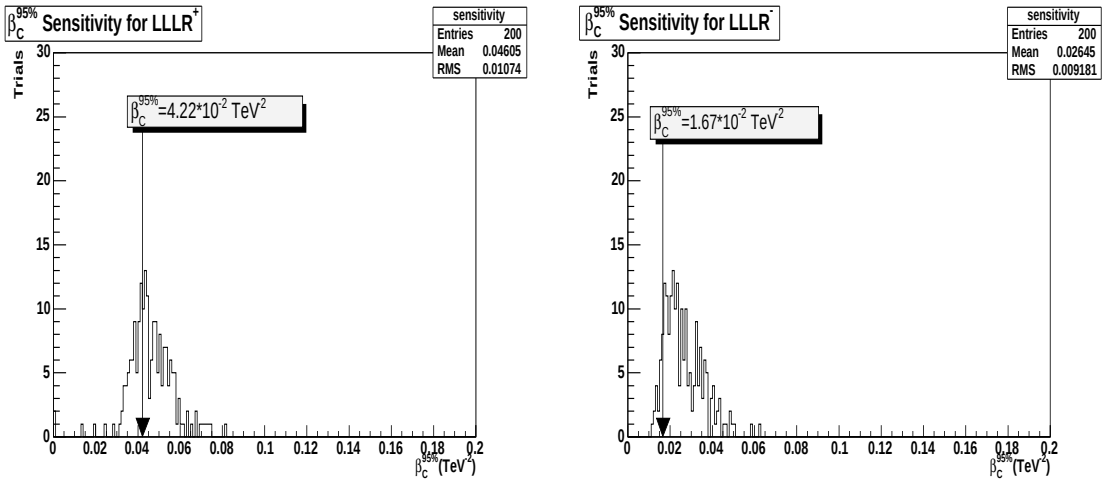

Figure 4.41. The distribution of best fit values on β_C for 200 MC trials for LLLR (constructive and destructive)

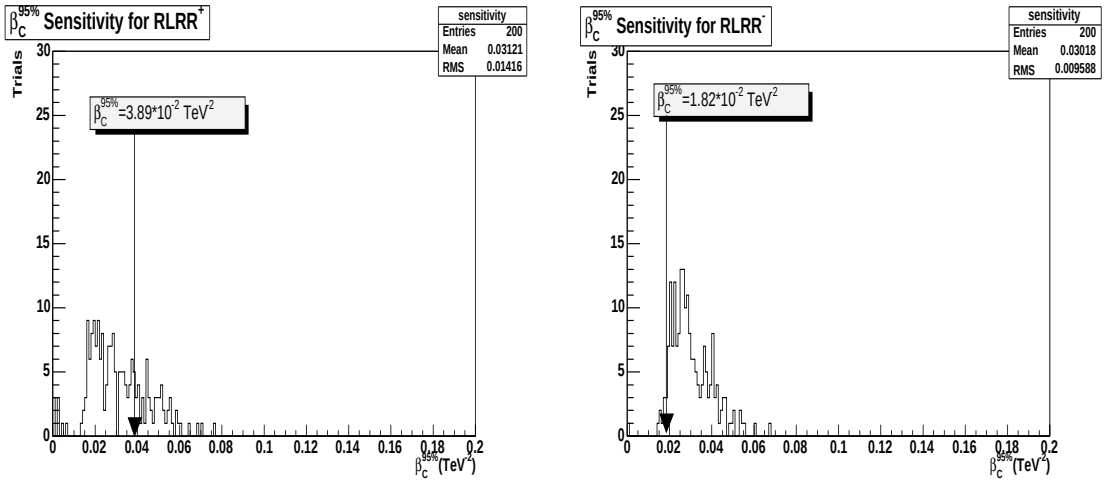

Figure 4.42. The distribution of best fit values on β_C for 200 MC trials for RLRR (constructive and destructive)

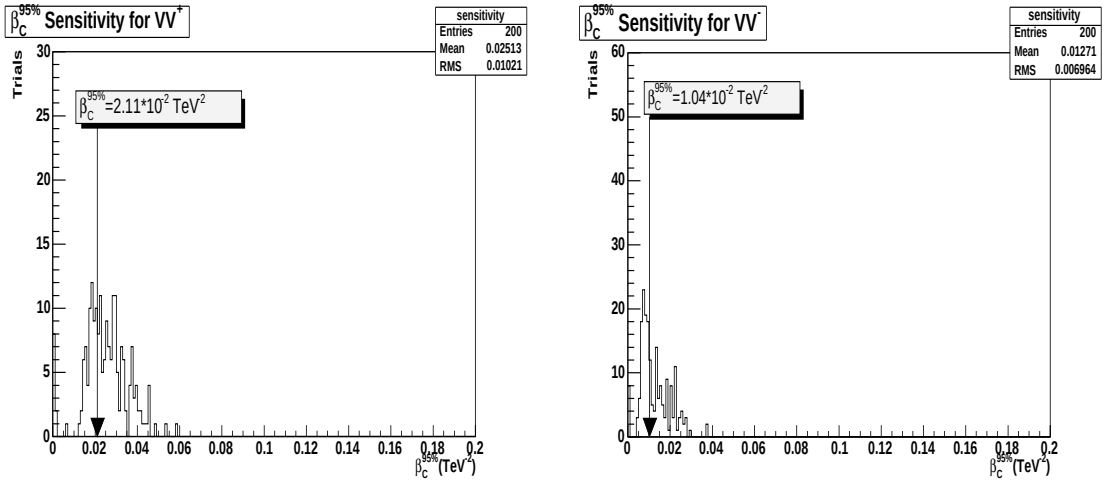

Figure 4.43. The distribution of best fit values on β_C for 200 MC trials for VV (constructive and destructive)

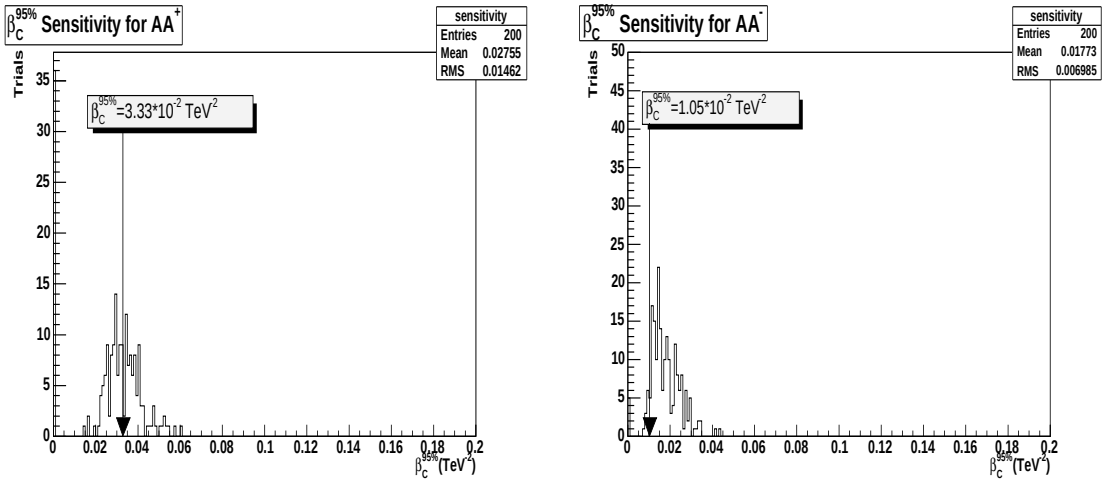

Figure 4.44. The distribution of best fit values on β_C for 200 MC trials for AA (constructive and destructive)

CHAPTER 5

CONCLUSIONS

The search for quark and lepton compositeness using 400 pb^{-1} of data collected with the DØ detector at the Fermilab Tevatron was presented. No evidence for quark-lepton compositeness was found. The model-dependent lower limits at the 95% confidence level on the compositeness scale of 4.2 to 9.8 TeV for constructive and destructive interference between the Drell-Yan (DY) amplitude and the contact interaction for various quark and lepton chiralities were obtained (see Table 5.1). They are superior to reported limits on quark-lepton compositeness of 3.3 TeV to 6.1 TeV in the dielectron channel at DØ in Run I and better than the preliminary limit of 3.6 TeV to 9.1 TeV reported for the same channel in Run II.

Table 5.1

DØ RUN II 95% CL LOWER LIMIT ON COMPOSITENESS SCALE Λ FOR DIFFERENT CONSTRUCTIVE AND DESTRUCTIVE CONTACT INTERACTION MODELS IN DIMUON CHANNEL.

Model	Λ^+(TeV)	Λ^-(TeV)
LL	4.19	6.98
RR	4.15	6.74
LR	5.32	5.10
RL	5.31	5.17
LL+RR	5.05	9.05
LR+RL	6.45	6.12
LL-LR	4.87	7.74
RL-RR	5.07	7.41
VV	6.88	9.81
AA	5.48	9.76

APPENDIX A

CANDIDATE EVENTS

In the final sample there are seven events with mass above 300 GeV. The events with the highest mass and with the next to the highest mass are chosen as two candidate events to examine.

Parameters for the two candidate events are shown in Tables A.1-A.2. Table A.1 lists the information for the event with the highest invariant mass, and Table A.2 shows the same information for the candidate event with the next to the highest mass. D0ve XYview and RZview event displays for these events are shown in Figures A.1-A.2.

Table A.1

PARAMETERS OF THE HIGHEST MASS CANDIDATE EVENT.

Run	Event	M (GeV)	$\cos(\theta^*)$
174996	9150818	522	0.15

	μ_1	μ_2
p_T (GeV)	1000.0	255.0
ϕ (radians)	-0.40	2.63
η	-0.05	0.37
A-Layer Scintillator Time (ns)	-3.51	-0.63
BC-Layer Scintillator Time (ns)	4.06	3.40
Calorimeter Halo (GeV)	0.16	1.50
Track Halo (GeV)	0.70	1.82

Table A.2

PARAMETERS OF THE NEXT TO THE HIGHEST MASS CANDIDATE EVENT.

Run	Event	M (GeV)	$\cos(\theta^*)$
188975	66717850	409.1	0.38

	μ_1	μ_2
p_T (GeV)	564.7	184.2
ϕ (radians)	1.25	-2.17
η	0.75	-0.12
A-Layer Scintillator Time (ns)	-3.55	-2.04
BC-Layer Scintillator Time (ns)	-5.96	-3.23
Calorimeter Halo (GeV)	0.28	0.34
Track Halo (GeV)	0.0	1.11

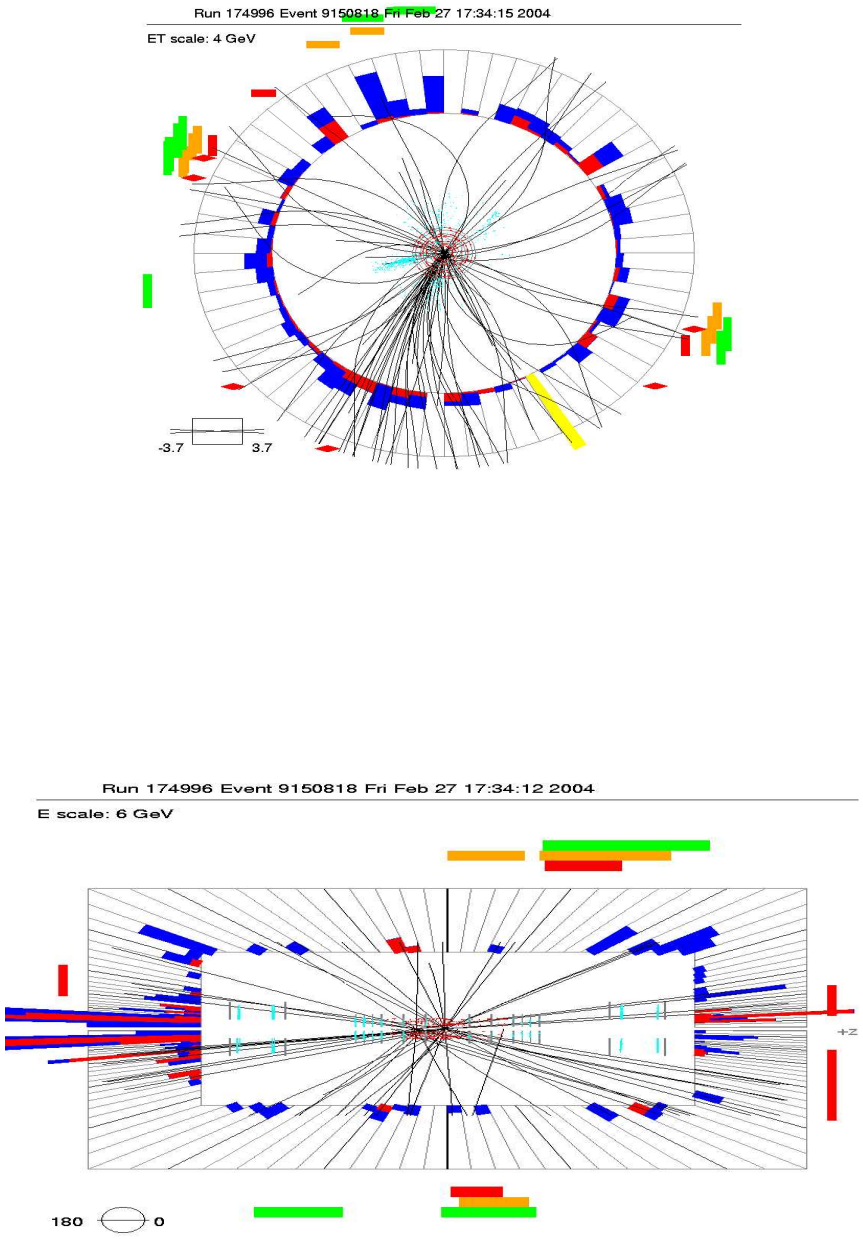

Figure A.1. The top figure shows XY view for the highest mass event. The bottom figure shows the $r - z$ view for the event. Reconstructed tracks are shown as well as muon system hits displayed as polygons or rectangles. Adapted from [51]

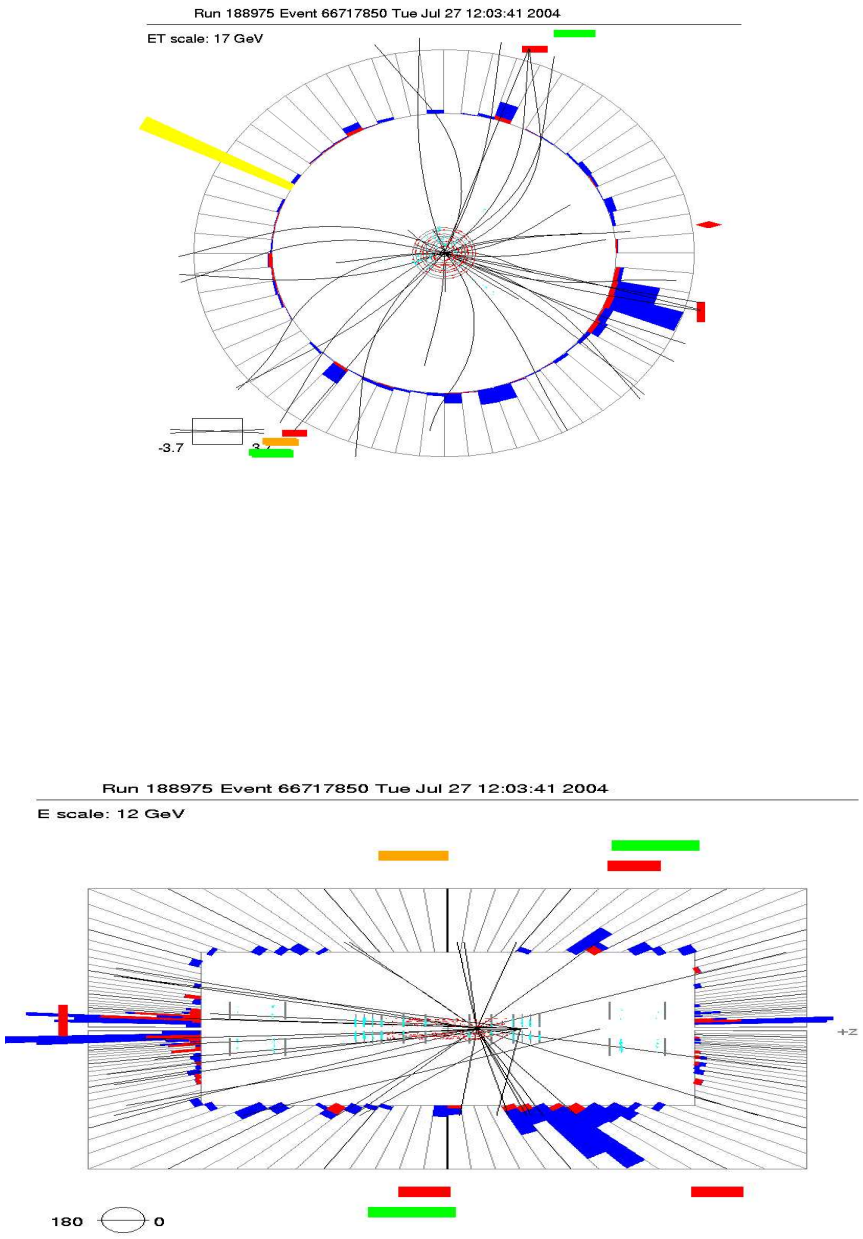

Figure A.2. The top figure shows the XY view for the next to the highest mass event. The bottom figure shows the $r - z$ view for the event. Reconstructed tracks are shown as well as muon system hits displayed as polygons or rectangles. Adapted from [51]

BIBLIOGRAPHY

[1] P. Ramond "Journey Beyond the Standard Model", Westview Press, Colorado (2004).

[2] D. Lincoln "Understanding the Universe from Quarks to the Cosmos", World Scientific, New York (2004).

[3] A. Gupta, Ph.D. Thesis, Tata Institute of Fundamental Research, India, 1999 (unpublished).

[4] V. D. Barger and R. J. N. Phillips, "Collider Physics", Addison-Wesley Publishing Company, New York, (1996).

[5] F. Halzen and A. D. Martin, "Quark and Lepton: An Introductory Course in Modern Particle Physics", John Wiley and Sons (1984).

[6] R. Harnberg, W.L. Van Neerven, and T. Matsura, Nucl. Phys. **B359**, 343 (1991); S. Mrenna, private communication.

[7] E. Eichten, K. Lane and M. Peskin, Phys. Rev. Lett. **50**, 811 (1983);
E. Eichten, I. Hinchliffe, K. Lane and C. Quigg, "Review of Modern Physics", **56**, October 1984.

[8] K. S. Babu, C. Kolda, J. March-Russell and Frank Wilzeck, hep-ph/9703299.

[9] V. Barger *et al.*, hep-ph/9703311.

[10] A. Nelson, Phys. Rev. Lett. **78**, 4195 (1997).

[11] N. Bartolomeo and M. Fabbrichesi, Phys. Lett. **B406**, 237 (1997).

[12] W. Buchmuller and D. Wyler, hep-ph/9704317.

[13] CDF Collaboration, F. Abe *et al.*, Phys. Rev. Lett **77**, 5336 (1996).

[14] DØ Collaboration, B. Abott *et al.*, Phys. Rev. Lett **80**, 666 (1998).

[15] OPAL Collaboration, K. Ackerstaff *et al.*, Phys. Lett **391**, 221 (1997).

[16] H1 Collaboration, C. Adloff *et al.*, Z. Phys. **C74**, 191 (1997); ZEUS Collaboration, J. Breitweg *et al.*, Z. Phys. **C74**, 207 (1997).

[17] P. Lanngacker, Phys. Lett **256**, 277 (1991); M. Leurer, Phys. Lett **D49**, 333 (1994).

[18] K. S. McFarland *et al.* (CCFR), FNAL-Pub-97/001-E.

[19] T. Nunnemann, DØ Internal Note #4476.

[20] S. Chakrabarti, "Search for Quark-Electron Compositeness in e^+e^- Production", DØ Internal Note #4552.

[21] R. Hooper, Ph.D. Thesis, University of Notre Dame, 2004 (unpublished).

[22] Fermi National Accelerator Laboratory, Batavia, Illinois (USA), Tevatron Run II Handbook, Internal FNAL Note.
`http://www-bd.fnal.gov/runII/index.html`

[23] Elvin Harms and Jim Morgan, "The Antiproton Source Rookie Book".
`http://www-bdnew.fnal.gov/pbar/documents/PBAR_Rookie_Book.PDF`

[24] DØ Collaboration, B. Abachi *et al.*, Phys. Rev. Lett. **74** 2632 (1995).

[25] CDF Collaboration, F. Abe *et al.*, Phys. Rev. **74** 2626 (1995).

[26] DØ Collaboration, Nucl. Instr. Meth. **A338**, 185 (1994)

[27] A. Melnitchouk, *Search for non-SM Light Higgs Boson in the $h \to \gamma\gamma$ Channel*, Ph.D. Thesis, Brown University, 2003 (unpublished).

[28] A. Patwa, Ph.D. Thesis, Stony Brook University, 2002 (unpublished).

[29] A.R.Baden "Jets and Kinematics in Hadronic Collisions", January 1997.

[30] `http://www-d0.fnal.gov/Run2Physics/displays/presentations/#gallery`

[31] DØ Collaboration, "DØ Silicon Tracker Technical Design Report", DØ Internal Note #2169, 1997 (unpublished).
`http://d0server1.fnal.gov/projects/silicon/www/tdr_final.ps`

[32] DØ Collaboration, "The DØ Upgrade Central Fiber Tracker: Technical Design Report", DØ Internal Note #4164, 1997 (unpublished).
`http://d0server1.fnal.gov/users/stefan/www/CFT_TDR/CFT_TDR.ps.`
Plus discussions and notes from Gaston Gutierrez.

[33] G. Gutierrez, "Central Fiber Tracker Mechanics: Ribbon Data", Internal DØ Document, 2001.
`http://d0server1.fnal.gov/projects/sciFi/mechanical/documentation.html`

[34] A. Bross *et al.*, "SCIFI 97: Conference on Scintillating Fiber Detectors", AIP Conference Proceedings 450, 1998.

[35] M. Gao, *A Search for Extra Neutral Gauge Boson in the Dielectron Channel with the DØ Detector in $p\overline{p}$Collisions at $\sqrt{s}$=1.96 TeV*, Ph.D. Thesis, Columbia University, 2003 (unpublished). And private communications.

[36] M. Adams *et al.*, "Design Report of the Central Preshower Detector for the DØ Upgrade", DØ Internal Note #3014.

[37] A. Gordeev *et al.*, "Technical Design Report of the Forward Preshower Detector for the DØ Upgrade", DØ Internal Note #3445, 1998 (unpublished).

[38] P. Demine, *Study of the tri-lepton events in the Run II data of the DØ experiment at the Tevatron. Interpretation in the R-parity violating supersymmetry framework (λ coupling)*, Ph.D. Thesis, ISN Grenoble, 2002 (unpublished).

[39] K. Cheung and G. Landsberg, Phys. Rev. D **62**, 076003 (2000).

[40] S. Jain, DØ Internal Note #3752.

[41] S. Jain, CMS Note 1999/075

[42] G. Landsberg, DØ Internal Note #4336

[43] R. Hooper, G. Landsberg, DØ Internal Note #4576

[44] P. Telford, DØ Internal Note #4297

[45] G. Landsberg, DØ Internal Note #3729, v4.0.
`http://www-d0.fnal.gov/~gll/d0_private/ed1.htm`

[46] DØ New Phenomena Group. NP group skimming web page.
http://www-clued0.fnal.gov/gusbroo/d0_ private/skims-to-trees.html, 2004.

[47] DØ Common Samples Group CS group website
http://www-d0.fnal.gov/Run2Physics/cs/index.html, 2004.

[48] ROOT: An Object-Oriented Data Analysis Framework.
`http://root.cern.ch.`

[49] E. Nurse, P. Telford, "Measurement of $\sigma \times Br$ for $Z \to \mu^+\mu^-$ in $p\overline{p}$ collisions at $\sqrt{s} = 1.96$ TeV.", DØ Internal Note #4284

[50] C. Clement *et al.*, MuonID Certification for p14, DØ Internal Note #4350.

[51] R. Hooper, G. Landsberg, "Search Randall-Sundrum Gravitons in the Dimuon Channel with 250 pb^{-1} of Run II Data", DØ Internal Note #xxxx.

[52] P. Telford, DØ Internal Note #4160

[53] R. Hooper, J. Zhu, DØ Internal Note #4067

[54] The CDF Collaboration, Phys. Rev. Lett. **79** 2191 (1997).

[55] `http:/www-d0.fnal.gov/Run2Physics/WWW/documents/temp/lum_calc1.pdf`

[56] R. Hooper, Talk given to the Muon ID Group, July 1st 2003
`http://www-d0.hef.kun.nl///displayLevel.php?fid=26..`

[57] D. Whiteson and M. Kado, DØ Internal Note #4070.

[58] I. Bertram, G. Landsberg, J. Linneman, R. Partridge, M. Paterno, H.B. Prosper, DØ Internal Note #3476.

[59] J. Hobbs, G. Landsberg, `http://d0server1.fnal.gov/users/hooper/CL95g++.C`

[60] CTEQ Collaboration (Coordinated Theoretical/Experimental Project on QCD Phenomenology and Tests of the Standard Model), H.L. Lai et al., and S. Kuhlmann(ANL), S. Mishra(Harvard), R. Brock, J. Pumplin, C.P. Yuan (MSU), D. Soper(Oregon),J. Collins, J. Whitmore(PSU), F. Olness (SMU), and J. Smith, G. Sterman(Stony Brook).

[61] H.L. Lai et al.(CTEQ Collaboration), Phys. Rev.**D51**, 4763 (1995).

[62] H.L. Lai et al.(CTEQ Collaboration), Phys. Rev.**D55**, 1280 (1997).